National Aeronautics and
Space Administration

CFT-RPT-0015
Revision: Basic
Effective Date: 10/27/2022

John H. Glenn Research Center
Cage Code No.: 1QFP5
21000 Brookpark Road
Cleveland, OH 44135

CRYO-FLUID MANAGEMENT PROJECT

Cryogenic Thermal Coatings Final Report

Authorized By CM For Use	
Date	**Signature**
10/27/2022	Tracy A. Leonard

Signature Page

Prepared by: /electronic signature/ _____

Tracy L. Gibson, Ph.D. *Date*
Subject Matter Expert
Kennedy Space Center, LASSO

Concurred by: /electronic signature/ _____

Mark A. Nurge, Ph.D. *Date*
Research Ast, Sensors & Transducers
Kennedy Space Center, UB-G2

Approved by: /electronic signature/ _____

Michael P. Doherty *Date*
CFT Project Manager
Glenn Research Center

Released by: /electronic signature/ _____

Tracy A. Leonard *Date*
Configuration Data Management Lead
Glenn Research Center

Change History

Revision	Effective Date	Description
Basic	*10/27/2022*	*Initial Release*

Table of Contents

Table of Figures

List of Tables

1.0 EXECUTIVE SUMMARY

The goals of this project were to produce yttrium oxide- (Y_2O_3) based tiles and a spray-on coating with minimal solar absorption, to perform exposure testing on these coatings (both rigid and spray-on), and to work towards a manufacturing process whereby these coatings could be made available to the space community. The Key Performance Parameters (threshold values) were to achieve 1% solar absorption for the tiles as measured in a deep space simulator, and 6% solar absorption for the spray-on coating as measured using a reflectance spectrometer. The values achieved were 1.2% (GRC Deep space simulator) and 4% (KSC spectrometer using Spectralon as a reference) for the tiles and spray-on coating, respectively. Exposure testing consisted of measuring tile and spray-on coating degradation due to atomic oxygen, ultraviolet radiation, and electrostatic fields. Atomic oxygen caused some degradation, while ultraviolet exposure caused a significant increase in absorption. However, in-space samples exposed to solar ultraviolet did not show this significant increase. This discrepancy is addressed in this report.

As a result of this work, Y_2O_3 tiles have been manufactured in the Kennedy Space Center (KSC) Applied Chemistry Laboratory (ACL), and the process has been transferred to the Thermal Protection System Facility (TPSF) at KSC. The TPSF manufactures coatings for the space community and is an ideal route by which future users could access Y_2O_3-based coatings. The spray-on coating has been developed such that it can be applied to a wide range of substrates, substantially lowering absorbed solar power as compared to currently available coatings.

2.0 INTRODUCTION/SUMMARY

In the spring of 2015, a Phase 1 NASA Innovative Advanced Concepts (NIAC) project was awarded to KSC entitled “Cryogenic Selective Surfaces.” Under this effort, a novel, high reflectivity coating was proposed that consisted of sintered particles with a reflective metallic backing. Analysis showed that this coating could potentially achieve cryogenic temperatures in deep space, essentially reflecting enough of the Sun’s irradiant power, while emitting thermal power, to achieve steady state temperatures below 90 K. This work was published [1] and documented in a NIAC final report [2]. In addition, a patent application was filed, and the patent was awarded in 2019 [3]. During this time, the name “Solar White” was coined as an alternative to “Cryogenic Selective Surface” or, as it was later called, “Cryogenic Thermal Coating.” In this report, all three names refer to the new coating under development, though the name “Cryogenic Thermal Coating,” or CTC, will be preferred.

A phase 2 NIAC proposal was submitted and awarded, starting in the summer of 2016, to advance the concepts to develop an actual coating. In addition, supplemental funding was provided by the Launch Services Program (LSP) at KSC and from internal KSC research and development sources. The next two years saw the creation of rigid tiles composed of barium fluoride (BaF_2) and, eventually, Y_2O_3, along with the development of an early deep space simulator. This work was published [4], documented in detail in a NIAC final report [5], and patented [6]. In addition, near the end of the project a small amount of funding was supplied by Nuclear Thermal Propulsion (NTP), which was seeking improved reflectance of solar radiation to maintain liquid hydrogen in space. With that funding, a spray-on version of the Y_2O_3 coating was invented, which was eventually submitted for a patent [7] (this patent was granted in August 2022 but has not been published as of the writing of this report).

In 2017, a NIAC Phase 1 project was awarded called "Solar Surfing." Under this project, the potential use of a Y_2O_3-based rigid tile coating as an improvement over the carbon composite shield used on the Parker Solar Probe was explored. The hope was that a future probe could reach within 1 solar radius of the Sun, as opposed to the 8 solar radii limit of the Parker Solar Probe. This work had some impact on the development of the Y_2O_3 tiles, but, more importantly for the current application, documents our analysis of multiple other materials that might be used instead of Y_2O_3 [8].

After the Phase 2 NIAC ended in September 2018, Game Changing funding was sought to continue the work, but the technology readiness level (TRL) was determined to be too low due to our recent switch to Y_2O_3. However, seedling funding was provided to advance the work, and additional funding was also provided by LSP to bridge the gap until a full Game Changing Project could be initiated, which occurred in the fall of 2019. Cryogenic thermal coatings were determined to be outside of KSC's "swim lanes" and consequently, the Game Changing Project was submitted by the Glenn Research Center (GRC), who would administer the project and perform much of the testing. Some of the GRC members were also part of the Phase 2 NIAC project, so this two-center joint project was a natural extension of the prior work.

In the fall of 2019, a kick-off meeting was held at GRC, during which the goals of the project were presented, and a schedule was developed for this two-year effort. It was decided that the focus of the first year would be the tiles, including purchasing a higher temperature oven to improve the tile performance, and then testing the tiles under atomic oxygen and ultraviolet exposure. This would allow the second year to be spent on extending the spray-on coating, additional testing, and working on any issues resulting from the testing. However, the advent of COVID disrupted the work. In March 2020, both KSC and GRC were closed, and the project was effectively suspended.

Prior to this, in the spring of 2018, LSP at KSC decided that the cryogenic thermal coating needed to be tested in low Earth orbit (note that several samples have been exposure tested on the International Space Station (ISS) under the Materials International Space Station Experiment (MISSE)). To complete this testing, LSP initiated a CubeSat development project called Passive Thermal Coating Observatory Operating in Low-Earth Orbit (PATCOOL) at the University of Florida (UF). The UF team went through several rounds of development and design reviews [9], and LSP was told that a launch date in the summer of 2021 had been chosen. This is significant because under KSC COVID guidelines, work required to meet a launch date was rated as mission critical and would allow workers to return to the space center. Consequently, on June 11, 2020, the KSC cryogenic thermal coating team was given permission to return to KSC and continue the development of the coating, directed towards the needs of the CubeSat.

The COVID impact to the project was primarily two-fold: 1) KSC personnel were restricted to tele-work for 3 months, and GRC personnel were out for 20 months (until October 2021), significantly affecting the interaction between the two centers, and 2) the CubeSat needed the spray-on coating developed, so that effort was moved into the first year, pushing the tile work into the second year of the project. The project schedule was rearranged to reflect these two impacts. By the end of the summer of 2020, the spray-on coating development had met its KSC milestones, and a detailed report was prepared and made public [10]. KSC personnel worked through FY21 developing the Y_2O_3 rigid tiles, generating a detailed report in the summer of 2021 [11]. In

addition, two publications describing the cryogenic thermal coatings and their testing appeared in the 2021 Cryogenic Engineering Conference & International Cryogenic Materials Conference [12,13].

Table 3-1. Key performance parameters.

Performance Parameter	State of the Art	Threshold Value	Project Goal
KPP 1: Solar Absorption of Rigid Tiles (%)	6	1	0.3
KPP 2: Solar Absorption of Spray-on Coating (%)	15	6	3

By the end of FY21, KSC personnel had met all their project milestones, but the GRC team was still waiting to return to work, which occurred in October 2021). Multiple samples of the Y_2O_3 tiles and spray-on coatings were sent to GRC in September 2021 in preparation for the return to work. Over FY22, the GRC team delivered reports on atomic oxygen exposure (May 2022, Appendix D), ultraviolet exposure (May 2022, Appendix E), electrostatic degradation (August 2022, Appendix F), and the GRC Deep Space Simulator (August 2022, Appendix C). During this time, the KSC team worked on fabricating high-purity, consistent Y_2O_3 powder to replace the inconsistent material found when ordering from vendors (Appendix B describes this work).

3.0 THE PROJECT

3.1 SUMMARY

A detailed description of the Cryogenic Thermal Control project is provided below, with the caveat that, in the interest of succinctness, previously published material is only referenced and is not repeated. In addition, many details have been placed into the appendices to allow the body of the report to be more concise and easily read.

The project description is divided into sections. The first two sections describe advances made to the spray-on coating and the tile generation that have not been described in the extensive reports that are already published and available at the NASA Technical Reports Server. The third section describes the generation and results of fabricating high purity Y_2O_3. After that is an extensive section on testing, including descriptions of the GRC deep space simulator (the KSC deep space simulator is described in the published literature [12]) and its test results, test results on the spray-on coating from the KSC deep space simulator, reflectivity test results, results from the Materials International Space Station Experiment (MISSE), and the attempt to test the spray-on coating with a CubeSat. Following this is a section on the exposure testing performed at the Glenn Research Center, consisting of atomic oxygen exposure, ultraviolet exposure, and electrostatic degradation. The ultraviolet exposure issue is serious enough that a special section devoted to its understanding is included. Finally, there is a conclusion section that summarizes the results and discusses the remaining open issues.

3.2 SPRAY-ON COATING UPDATE

The spray-on paint formulation was used to coat carbon composite samples to evaluate its usefulness as a coating on composite overwrap pressure vessels (COPVs) commonly used to store cryogenics. The calculated solar absorptance was 6.12% (relative to Spectralon) which is not as

good as our best coating (2.07% relative to Spectralon on high grade aluminum). Long wave infrared can get through the coating and be absorbed by the dark colored COPV/carbon composite material, limiting the performance of the spray-on coating. Even so, this is an impressive result. A photo of the spray-on coating on carbon composite is shown in Figure 3-1.

Figure 3-1. Carbon composite sample coated with 15 layers of paint.

Multi-Layered Insulation (MLI) was also coated with solar white (Figure 3-2). The Thermal Protection Systems Facility (TPSF) coated additional MLI samples and made recommendations for scaling up the process and improving application efficiency. This will be further discussed below.

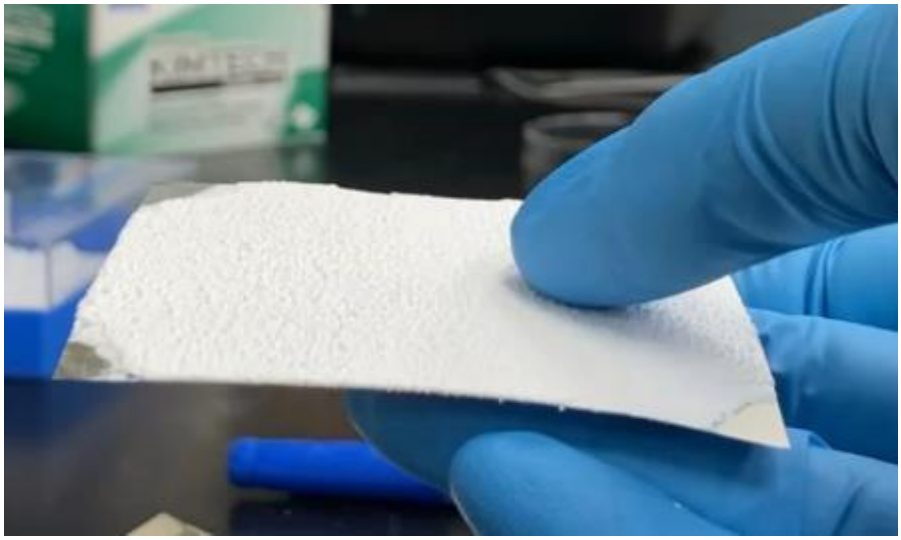

Figure 3-2. A single sheet of MLI coated with 15 layers of Solar White paint.

Some vendor supplied Y_2O_3 powders immediately settled out of solution when used in paint formulations. The team found that heating these powders to 1200^{o}C for 30 minutes, allowed these powders to stay suspended. Furthermore, it was found that powders that were previously able to

be made into paints without heating, performed better after heating. This is important because vendor supplied is much less expensive than the lab produced powder and some users have expressed interest in using the spray on material over large acreage.

Figure 3-3 shows Scanning Electron Microscope (SEM) images of one of the vendor-supplied powders before and after heating. Crystal face development and increased average particle size are observed after heating. Existing publications describe a "pre-sintering phenomenon" occurring in Y_2O_3 powders at 1200^{o}C [14]. Why this heating allows particles that readily settled out of solution to form a stable suspension is under investigation at the time of writing this report. It is possible that surface modification takes place upon heating in air that results in additional hydrogen bonding or hydration sites on the particle surfaces. Improvements in paint performance can likely be attributed to the changes in particle size. X-Ray Diffraction (XRD) analysis was performed by the materials scientist at GRC who concluded that the powders were in the same crystal phase prior to and after heating (cubic). XRD results are shown in Figure 3-4.

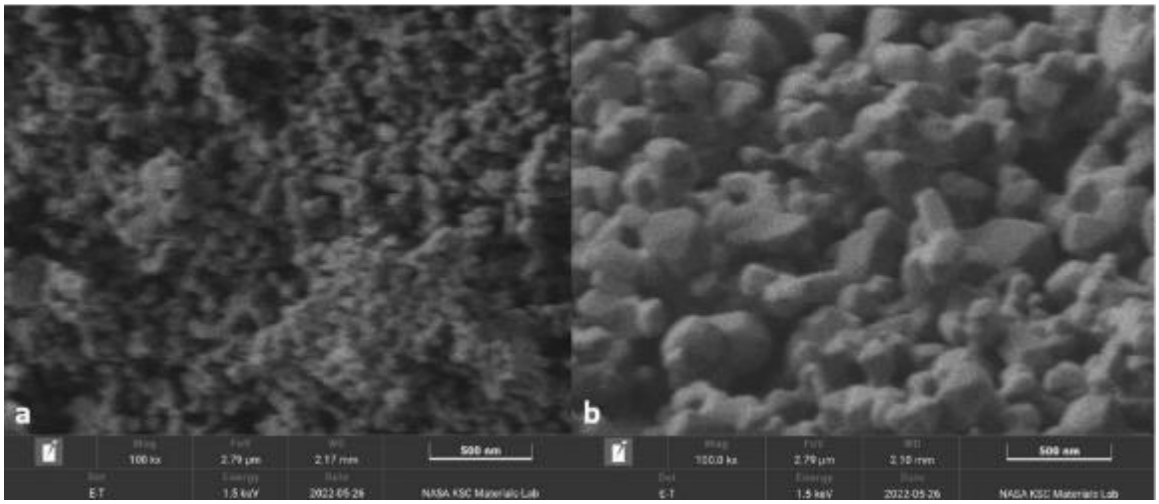

Figure 3-3. a) SEM image of as-received vendor supplied powder; b) SEM image of heat treated (1200 ^{o}C for 30 min) vendor supplied powder.

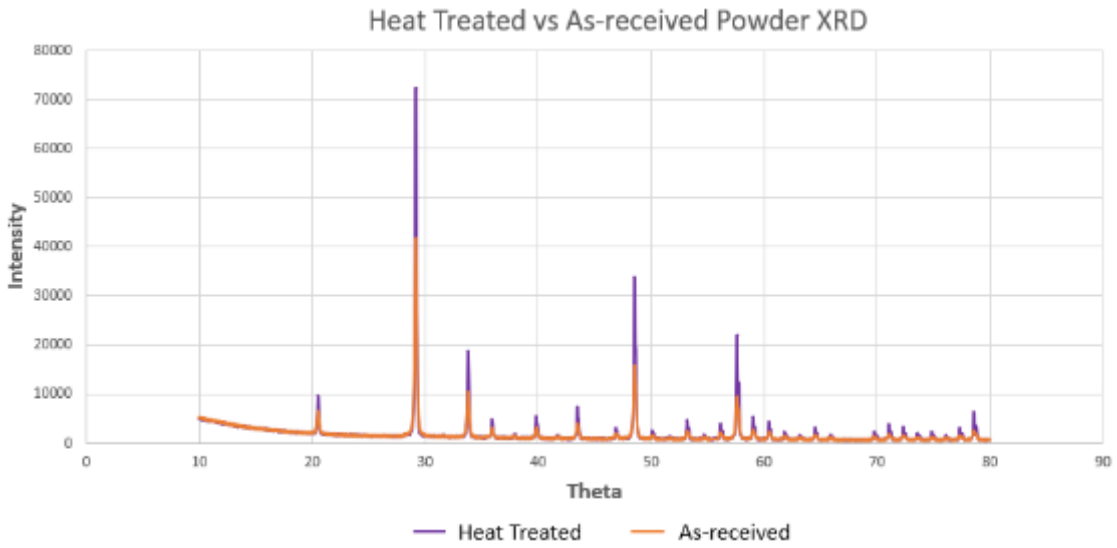

Figure 3-4. XRD of powders before and after heating, showing both are in the cubic phase.

Upon removing paint from the surfaces of aluminum coupons, the team noticed that the underlying aluminum was discolored. A galvanic reaction may be taking place between the less noble metals present in 7075 aluminum, such as zinc or magnesium, and the yttrium. This results in corrosion and discoloration of the metal surface. This is problematic because a reflective metal backing is required to prevent the absorption of infrared radiation. The team also noticed that 7075 from various sources behaved differently; this is likely due to the various forming options and finishes utilized in the manufacture of 7075. Figure 3-5 shows the difference in corrosion on a 7075 coupon and disk both of which were coated with the same type and amount of paint. Discoloration on the disk is much less noticeable than that of the square coupon. The team hypothesized reduced surface interaction due to the rough surface of the disk resulting from its manufacture could be a factor.

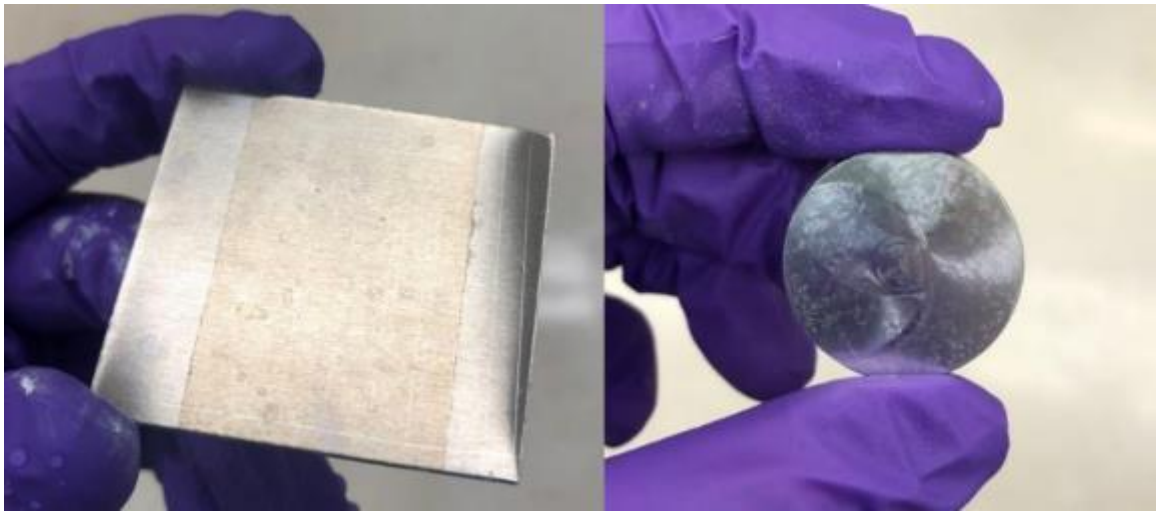

Figure 3-5. A 7075 coupon and disk after removal of heat-treated paint.

The team also attempted to reduce the corrosion by sputter coating a 7075 disk with pure aluminum which is very corrosion resistant. Figure 3-6 shows the corrosion observed after paint removal

from the sputter coated surface. Some pitting was observed but the discoloration was significantly reduced. It is possible that the pitting is due to an uneven sputter coat.

Figure 3-6. Corrosion after paint removal from an aluminum sputter coated 7075 disk.

Cladding is a technique often employed in aerospace and aviation to prevent corrosion by adding a thin layer of pure aluminum to part exteriors [15] and the team is considering investigating this as a potential solution to the corrosion issues. It is worth noting that corrosion was not observed on any of the MLI samples coated with paint.

3.3 TILE MANUFACTURING UPDATE

After noticing issues with potential color center formation (see the UV degradation section below), the team decided to try sintering rigid samples at lower temperatures to evaluate whether this would resolve the issue. Samples were heated to 1150^{o}C for 6 hours. This method yielded acceptable results and performed well in the UV region compared to rigids sintered at higher temperatures. The team also sintered the sample multiple times and a decrease in solar absorptance was observed with each sinter. Figure 3-7 shows spectra and solar absorptance results (relative to Spectralon) for this heating profile. However, because the particles are not truly sintering (or minimally sintering) at temperatures below 1200^{o}C, these rigids had reduced breaking strength when compared to previously fabricated barium fluoride rigids.

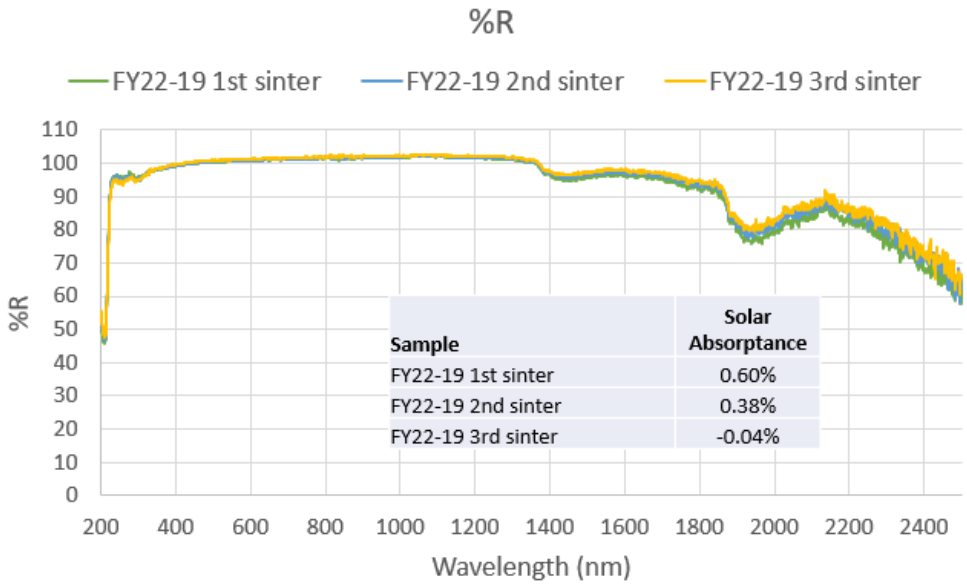

Figure 3-7. Spectroscopy and calculated solar absorptance relative to Spectralon for a rigid sample heated to 1150 ºC for 6 hours. The heating profile was repeated three times.

Ceramic molds and Y_2O_3 powder were provided to the TPSF to fabricate rigid samples and allow them to make recommendations for scale-up of the process. However, the rigid samples produced by the TPSF had a yellow discoloration after sintering in ovens at the TPSF, Figure 3-8. It is suspected that residual contamination is responsible for this discoloration as the ovens are used for a variety of manufacturing processes. Samples pressed at the TPSF and sintered in the ACL did not display this yellowing/contamination. It is likely that dedicated ovens will be required for tile manufacture to avoid contamination issues. In addition to contamination, the TPSF had difficulty using the ceramic molds because they would often crack and break during tile pressing. TPSF personnel also had difficulty removing tiles from these molds and would often crack or break the tiles during the removal process.

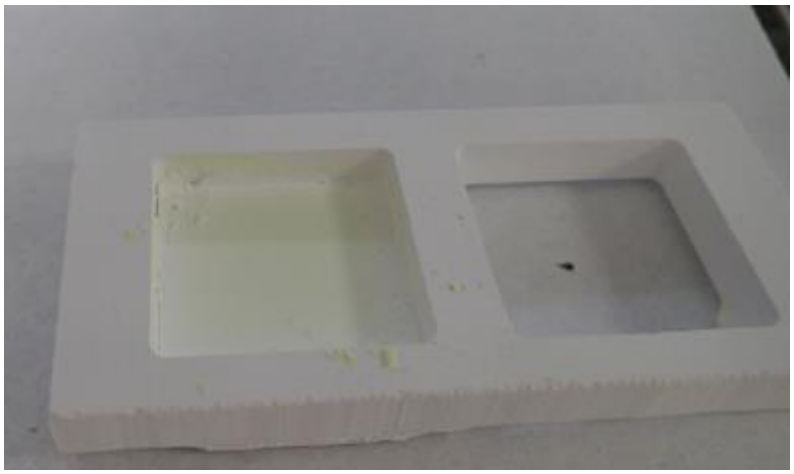

Figure 3-8. A discolored rigid sample fabricated by the TPSF inside the mold after sintering.

A new mold was fabricated to make 2" by 1.5" rectangular rigid samples. The mold is lined with sapphire to provide additional strength and to minimize contamination during pressing. A thin barrier film is placed over the base plate and ram during pressing to prevent the yttria powder from contacting the metal. This mold is also able to be taken apart using an Allen wrench which significantly reduces the likelihood of damaging the tiles upon removal from the mold. The TPSF was able to successfully press and remove tiles without breaking the mold or tiles. This mold was used for fabricating tiles that are 3mm-6mm thick. The 6mm thick tiles were cut into strips that are 8mm wide and 2" long. These strips were used for strength testing via ASTM C133. As previously stated, the rigid tiles fabricated from yttrium oxide showed significantly less flexural strength when compared to previously fabricated barium fluoride rigid tiles. Figure 3-9 shows photographs of the mold.

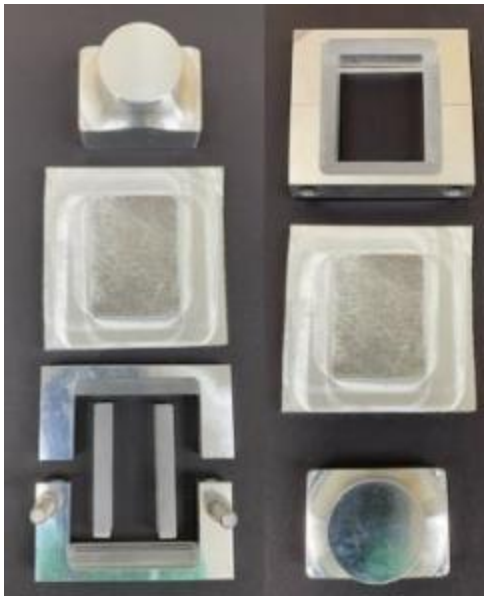

Figure 3-9. Sapphire-lined rectangular mold for tile fabrication.

3.4 HIGH PURITY Y_2O_3

Early in the project a 1-kilogram lot of 99.999% Rare Earth Oxide (REO) yttrium oxide nanopowder (100-200 nm Average Particle Size (APS)) was purchased from a commercial source and evaluated for use in the preparation of rigid thermal coating tiles and spray-on coatings (paints). The initial nanopowder performed in an acceptable manner for both rigid and spray-on coating applications. When the original 1-kilogram lot was depleted, another 5-kilogram lot of the same material (different lot) was purchased from the original vendor. Attempts were made to prepare both rigid tiles and spray-on coatings from this material, but all attempts were unsuccessful. After discussions with the vendor, another 5-kilogram lot of nanopowder was purchased in the hope that the issues identified with the previous lot were corrected. Again, attempts were made to prepare both rigid tiles and spray-on coatings from this material. This time, the team was able to successfully prepare rigid tiles but were unsuccessful in preparing spray-on coatings. Since the acquisition of yttrium oxide nanoparticles with consistent properties from the original vendor was difficult, yttrium oxide nanopowder was sourced from three other vendors. Attempts to fabricate rigid tiles and spray-on coatings using the yttrium oxide nanopowder from the second vendor were partially successful since the team was able to fabricate rigid tiles using

this yttrium oxide nanopowder; but the team was not able to fabricate spray-on coatings using this yttrium oxide. Attempts to fabricate rigid tiles and spray-on coatings using yttrium oxide nanopowder from the third vendor were unsuccessful. Attempts to fabricate rigid tiles and spray-on coatings using the yttrium oxide nanopowder from the fourth vendor were more successful in that the team was able to produce spray-on coatings using the nanopowder but were not able to fabricate rigid tiles.

Due to these consistency issues with procured yttrium oxide nanopowders, as well as some potential issues with contaminants in these nanopowders, a decision was made to synthesize the yttrium oxide nanopowders for use in fabricating rigid tiles and spray-on coatings. This was successful, allowing high purity yttrium oxide powders to be fabricated for both tiles and spray-on coatings. The resulting tiles and coatings performed well. Details are provided in Appendix B.

3.5 TESTING

There are three ways to measure the solar absorptivity of a coating or tile:

1. Following the ASTM standard; measure the reflectivity spectrum over a given wavelength, compare to a National Institute of Standard (NIST) standard, and then calculate the absorptivity using a standard solar spectrum. This is the easiest and most common approach; however, it suffers from several shortcomings. Very small misalignments or offset from the spectrometer integrating sphere can cause substantial error (for a given sample, with the KSC Jasco spectrometer, for every 0.01 inches of distance between the sample and the integrating sphere opening, the solar absorptivity drops by 2.7%), the NIST standard (Spectralon) isn't stable in the shortwave UV region and the spectral window being used does not account for all of the solar spectrum (about 3 % of the solar spectrum is beyond 2500 nm, a typical cutoff wavelength for the ASTM approach). There are more details on the shortcomings of this approach in reference 10.
2. Place the sample into a cold, evacuated chamber. After the sample comes to thermal equilibrium, expose it to a simulated solar spectrum and measure the temperature increase. This approach has the advantage of directly measuring the desired effect, the temperature increase due to absorbed solar irradiance. However, it still has shortcomings. The simulated solar spectrum is not accurate, especially in the short ultraviolet range and in the range beyond 2500 nm, and it can be difficult to accurately model the thermal increase, taking into account other heat sources and drains.
3. Place the sample in space and measure the temperature change relative to a control. This approach has the advantage of using the Sun itself, but, of course, requires substantial development. The Launch Control Program pursued this option (see the PATCOOL section) and it might be tried under a NASA tipping point project. In addition, samples of CTC were placed on the materials international space station experiment (MISSE), not to measure performance, but to gain insight into possible degradation due to atomic oxygen and ultraviolet exposure (see the MISSE section below).

3.5.1 Measuring Solar Absorptivity from Reflectivity Spectra

As mentioned in the introduction and in reference 10, determining the actual amount of solar radiation absorbed by a material by measuring its reflectance over a limited spectral window is error prone. Not only does this approach neglect regions of the spectrum and only offers a relative

measurement, it's also very sensitive to the positioning of the sample. Often samples that were measured at one facility yielded different results from another facility and we suspect that positioning partially resolves this discrepancy. To quantify this, a sample was placed in front of the integration sphere on a reflectance spectrometer and shims were used to space the sample back from the entrance. The results are shown in Figure 3-10, where we see that for every 4 thousandths of an inch set back the measured reflectance drops by 1%. This likely explains the results seen in the MISSE-11 samples discussed below.

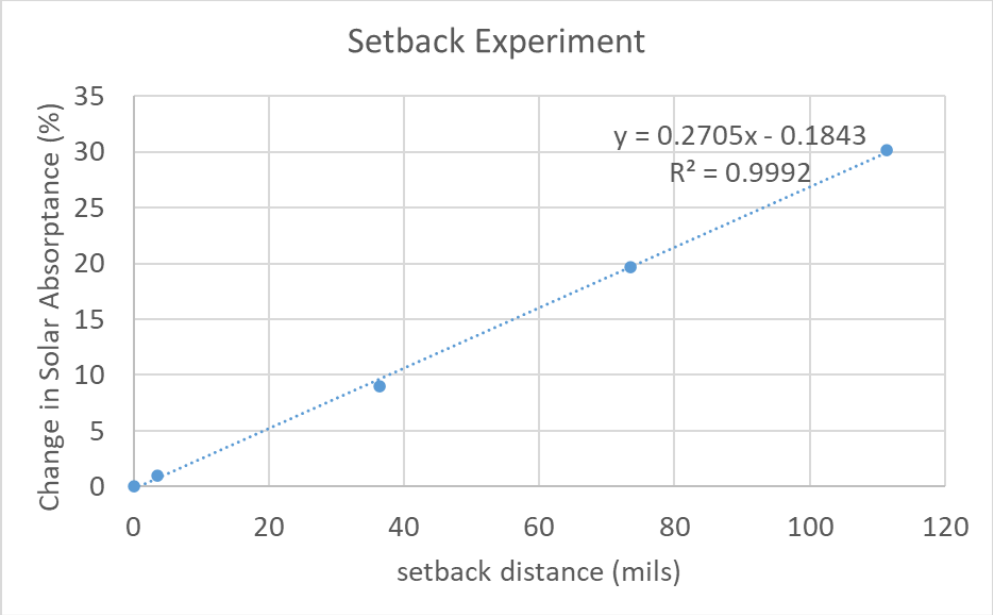

Figure 3-10. The change in measured reflectance vs. distance from the entrance to the integrating sphere.

Over the past several years, hundreds of reflectance spectra have been taken on solar white samples. Some examples of these reflectance spectra and resulting solar absorption are shown in Figures 3-11 through 3-13, which show the data for three samples prepared for a low Earth orbit test. Figure 3-11 shows the Y_2O_3 spray on sample reflectance spectrum with a photo. This sample has 15 lightly applied layers. Its original measured solar absorbance was 2.8%, relative to Spectralon, the NIST standard used in the reflectometer. It should be stressed here that many of our solar absorbances are listed as relative to Spectralon, which itself might have a solar absorbance of over 1 %. So, the solar absorbance of this sample would be about 4% taking that into account. The sample shown in Figure 3-11 was smoothed to make the surface more even by removing surface roughness (even so the photo shows some remaining bumps). After smoothing the solar absorption improved to 2.07%, most likely because the sample could now be brought a few thousandths of an inch closer to the integrating sphere, as discussed in the previous paragraph. The spectral reflectance spectrum shows some UV absorption (this will be discussed further in the UV degradation section) and then a somewhat linear drop from about 1000 nm to 1800 nm, due to the thin nature of this sample allowing longer wavelength light to get through it. The dip at about 2000 nm is likely an OH bond absorption.

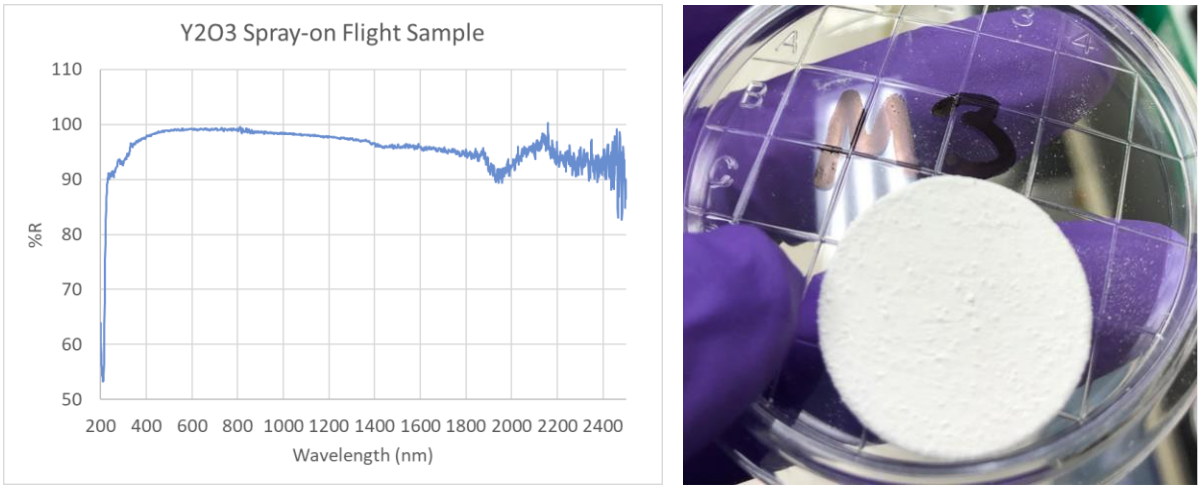

Figure 3-11. Reflectance spectrum (left) and photo (right) of the spray on sample chosen for a low Earth orbit flight exposure test.

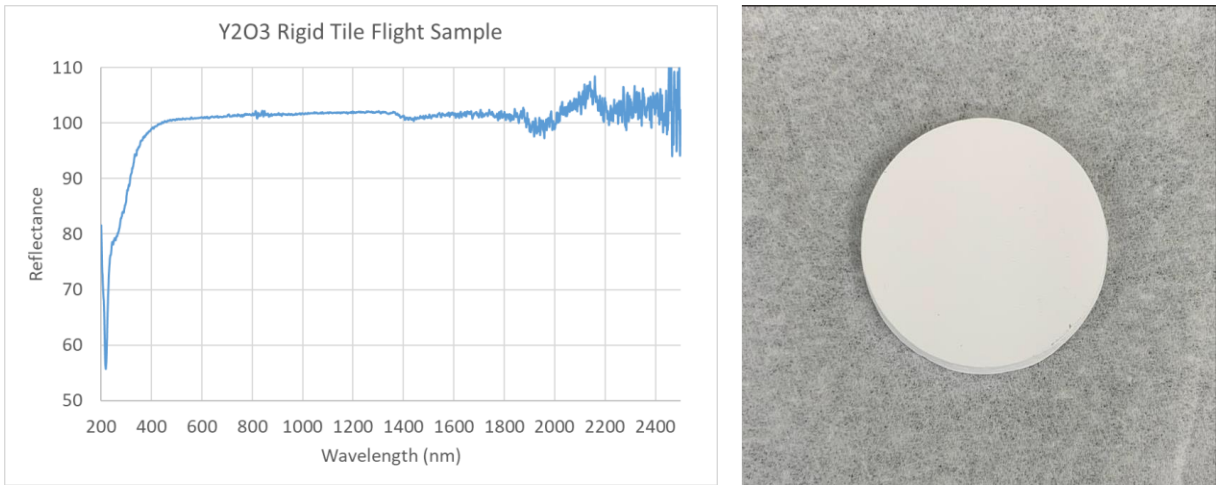

Figure 3-12. Reflectance spectrum (left) and photo (right) of the Y_2O_3 rigid tile chosen for a low Earth orbit flight exposure test.

Figure 3-12 shows the reflectance spectrum and a photo of the Y_2O_3 rigid tile selected for the low Earth orbit flight. This sample has a solar absorbance of -0.54 %, relative to the NIST standard Spectralon, in other words, even with the UV absorption shown in the spectrum, this tile reflects more solar radiation than Spectralon. Other measurements of similar tiles have shown solar absorbances of around 1%, which is consistent with the 1-1.5% absorption seen in Spectralon. Note the very good reflectivity even into the near infrared.

Figure 3-13 shows the reflectance spectrum and a photo of a tile composed of BaF_2. This tile has a similar net solar absorption to the Y_2O_3 tile, namely -0.60%. Note that this material has better UV reflectance, but worse reflectance in the near-IR. Some prior work has shown that BaF_2 has a water affinity, and the near-IR absorption structure is similar to that of water.

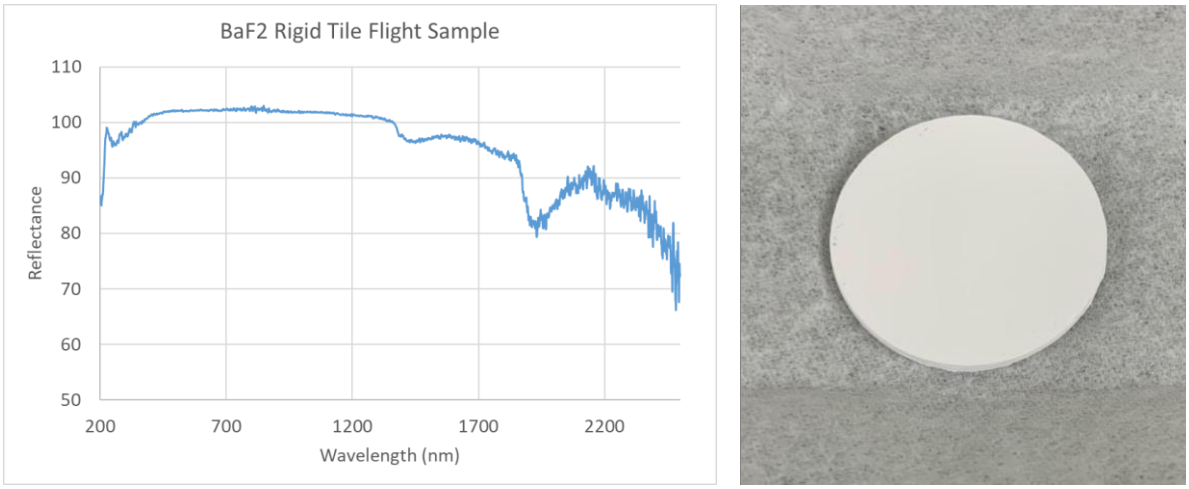

Figure 3-13. Reflectance spectrum (left) and photo (right) of the BaF_2 rigid tile chosen for a low Earth orbit flight exposure test.

Another issue with using reflection spectroscopy to determine solar absorptivity is changes in the NIST standard. Our work has used Spectralon, but Spectralon degrades with use; the UV absorption increases in the 200 nm regime over time. Figure 3-14 shows two reference scans taken of a NIST traceable Spectralon reflection standard, one on 1/03/2022 and one on 4/27/2022, with roughly 35 uses over the time period. The two traces are nearly identical except in the short UV region near 200 nm where the signal has dropped from over 120 to 60. Since Spectralon is the standard against which samples are compared, this change in the reference affects the measurements. We have tried to minimize this problem by limiting the use of the Spectralon, refinishing the surface occasionally to bring it back to its original reflectance, and using a secondary, more stable reference, namely one of our Solar White tiles.

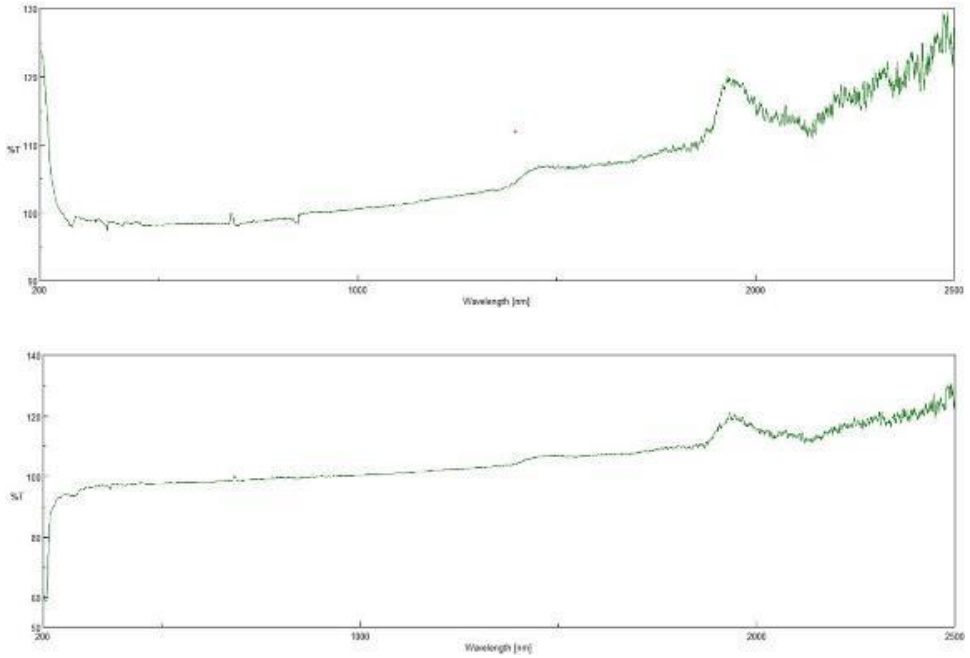

Figure 3-14. Two reference traces taken of a NIST Spectralon reflection standard after about 25 uses.

The Solar White coating partially reflects due to the suspended Y_2O_3 particles (it's paint-like component) and partially due to the reflectivity of the underlying material. Figure 3-15 shows the reflection spectra for the spray-on coating applied to a sapphire window, which has minimal reflectivity (about 7-8 % per surface). This was done to separate the two reflection components and allow just the paint portion of the reflectivity to be seen. The size of the Y_2O_3 has been chosen to maximize the reflectivity in the 400-500 nm range, which is seen in the data. But the reflectivity drops with increasing wavelength due to the reduced interaction of long wave radiation with the smaller particles (standard Rayleigh scattering as described in [1]).

A relatively simple paint theory [16] states that the variation in reflectivity should fit the function

$$\frac{a\,n}{a\,n+1}+b$$

where $a\,n$ is the number of scattering layers, assumed to be proportional to the number of spray layers, n, and b is an offset to compensate for the reflection of the sapphire itself under the coating. The dots shown in Figure 3-15 are fits of this function to the curves generated at each 50 nm interval. Considering the layers are applied manually and may not be exactly the same thickness, the fit is relatively close to the calculated functions. What this data shows is that in the 250-600 nm range, each spray layer corresponds to one scattering length (estimated to be about 0.5 mils or 12 microns) and that this scattering length increases to about 6 layers by 2000 nm and 10 layers by 2500 nm. It was expected that the scattering length would be about 1 micron in the short wavelength region, so further improvement in the spray on coating may be possible, probably by improving the distribution of the Y_2O_3 particles in the KBr binder or increasing the loading.

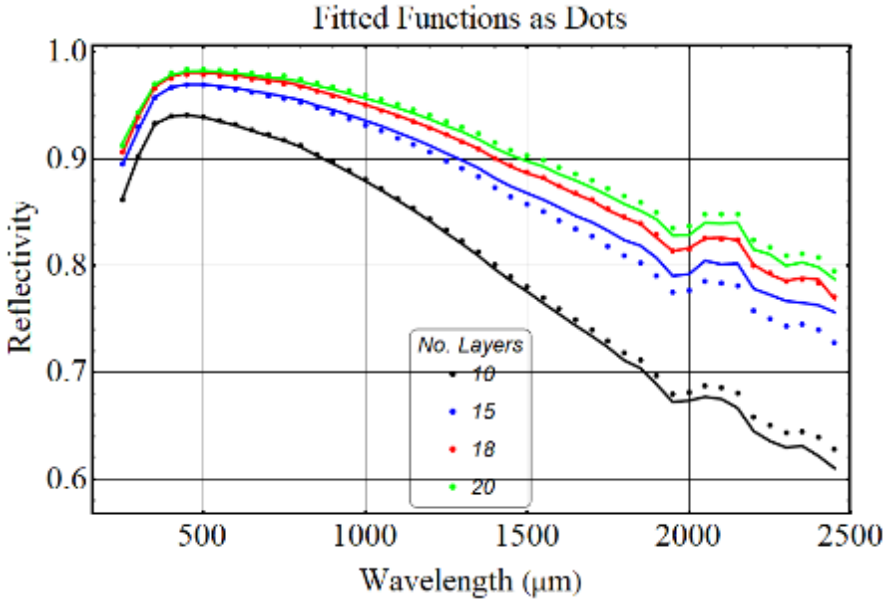

Figure 3-15. Reflection spectra for the spray-on coating on sapphire for various numbers of layers with a functional fit every 50 nm (dots).

3.5.2 The GRC Deep Space Simulator with Testing Results

The GRC deep space simulator and its testing results are provided in the appendix at the end of the report. Four Y_2O_3 tiles were tested yielding solar absorptivity values between 1.2 % and 2.7%. One spray on sample yielded a solar absorptivity value of 3.5%.

3.5.3 Test Results from KSC Deep Space Simulator, Spray-On Sample

Using a deep space simulator constructed at KSC, we have compared the performance of a spray-on Solar White sample and a similar sample sprayed with AZ-93. Both samples were placed in the chamber, which was evacuated and then cooled, allowing the samples to chill through radiation. Using this data, the emissivities of the two coatings were estimated to both be 0.9 or higher. Then, the output from a Xenon lamp was routed into the chamber using a quartz fiber bundle, simulating sunlight over a range of wavelengths. The rise in temperature of the samples was then used to determine solar absorptivity values, which were compared to their reflectance spectra measurement.

3.5.3.1 Summary of the KSC Deep Space Simulator

This system was described in detail in a recent conference publication [12], so only a short description is provided here. The system consists of a Xenon light source to simulate the solar spectrum. This light is focused onto a multimode fiber bundle and routed into a chamber where the sample is mounted (see Figure 3-16). The sample is located in an enclosure that is chilled to cryogenic temperatures simulating the black radiative background of the sky. The copper-based enclosure is located in a vacuum chamber that is pumped down to vacuum levels before chilling starts. The fiber bundle is chilled before contacting the sample chamber in order to remove any heat related radiation.

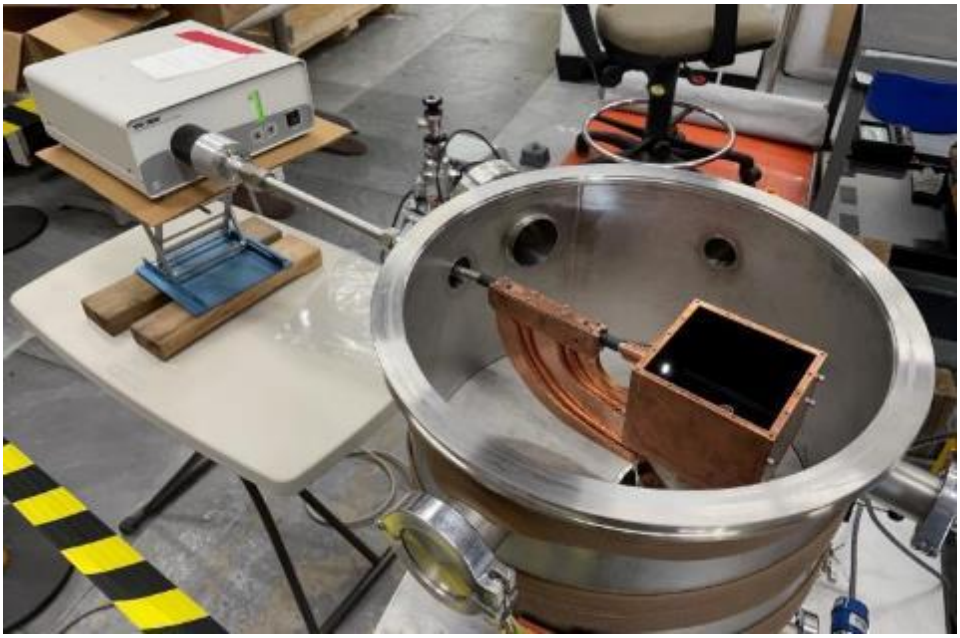

Figure 3-16. The KSC deep space simulator with vacuum chamber lid and enclosure lid removed.

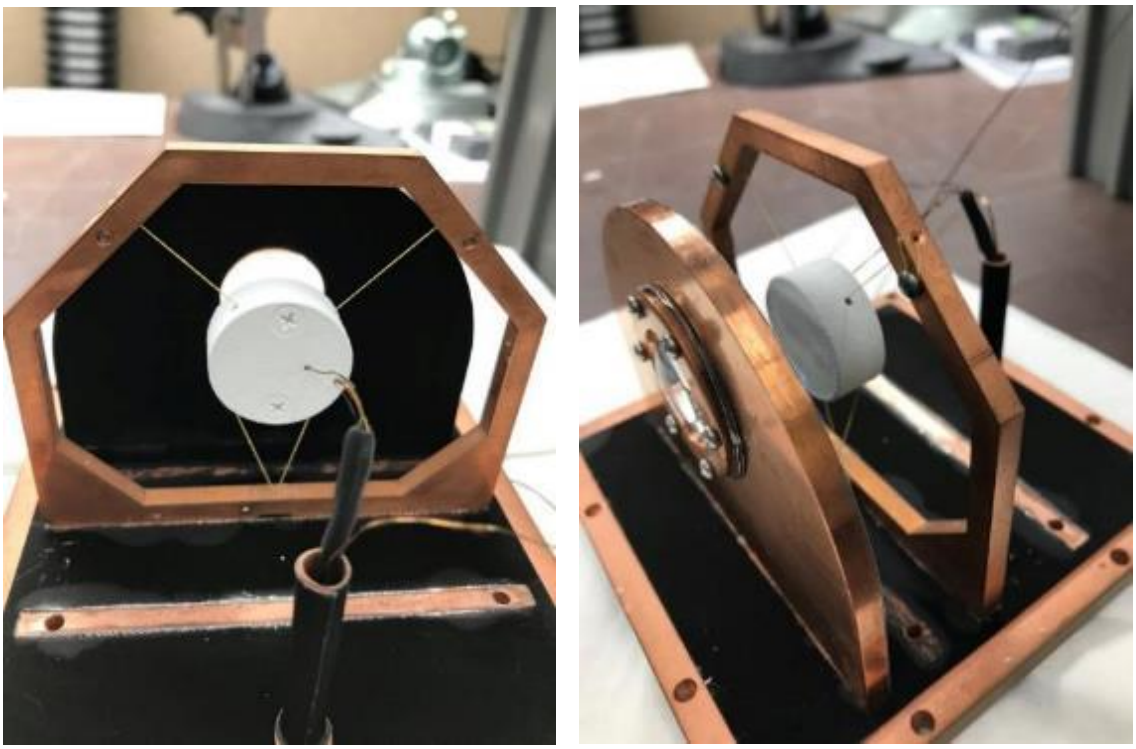

Figure 3-17. Images of the solar white sprayed sample mounted in a frame using Kevlar string, ready to be lowered into the test enclosure.

Figure 3-18. Images of the AZ-93 sample mounted in a frame using Kevlar string, ready to be lowered into the test enclosure.

The samples to be tested are mounted with Kevlar strings, as shown in Figures 3-17 and 3-18, to a copper frame. A one-inch focal length lens is used to capture the light emerging from the fiber, preventing it from diverging so it can illuminate the sample. At room temperature there is 850 mW of radiation hitting the sample. Prior testing has shown that this figure drops by 16% when the fiber is chilled, so we assume that 714 mW hits the sample when the system is cryogenically chilled.

During a test the vacuum chamber is pumped down and then the cryocooler turned on. There are four temperature sensors in the system.

Sensor 1 is mounted in the sample,
Sensor 2 is mounted on the lens holder,
Sensor 3 is mounted on the side of the enclosure, and
Sensor 4 is mounted on the cold head.

Sensors 2, 3, and 4 are mounted onto copper entities that are connected back to the cold head and minimal difference is seen in the temperatures provided by these sensors during testing. However, they provide a measurement of the temperature of the surrounding environment of the sample. Most of the inside of the enclosure is covered with an Edmund Optics black coating in order to absorb any light not absorbed by the sample (i.e., to minimize multiple impacts of the light onto the sample.). This black coating also means that the surrounding field of view of the sample can be assumed to have an emissivity near 1, allowing an estimate of the radiative heat load on the sample.

The samples are coated aluminum cylinders that screw together and contain a temperature sensor. Figure 3-19 shows an exploded view of one of the samples before the coating is applied. The disks are 7075 aluminum, machined smoothly, one-inch in diameter. The thicker disk (1/4 inch) contains a slot for the temperature sensor and two arced slots for the Kevlar string. It also has two tapped 4-40 holes allowing the 1/8th inch thick top plate to be attached. The top plate has a small hole to allow the temperature sensor wires to emerge (not shown in Figure 3-19). The temperature sensor (silicon diode from Scientific Instruments) is potted into the lower disk using Stycast.

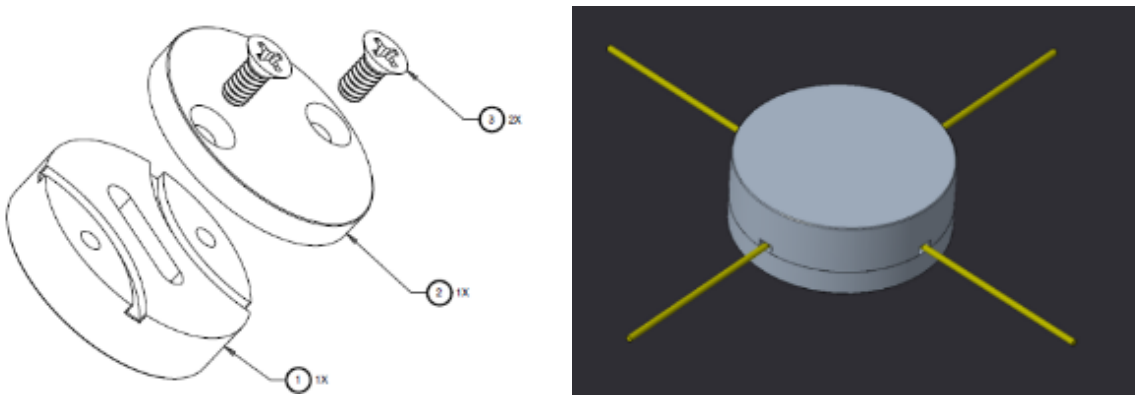

Figure 3-19. Sketches showing the composition of the samples before spraying.

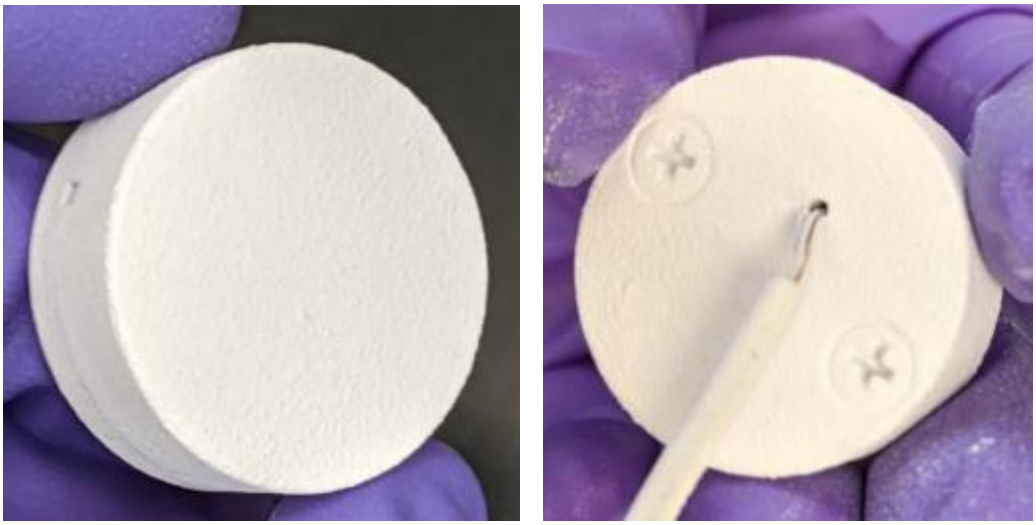

Figure 3-20. Front (left) and back (right) views of the spray-on samples.

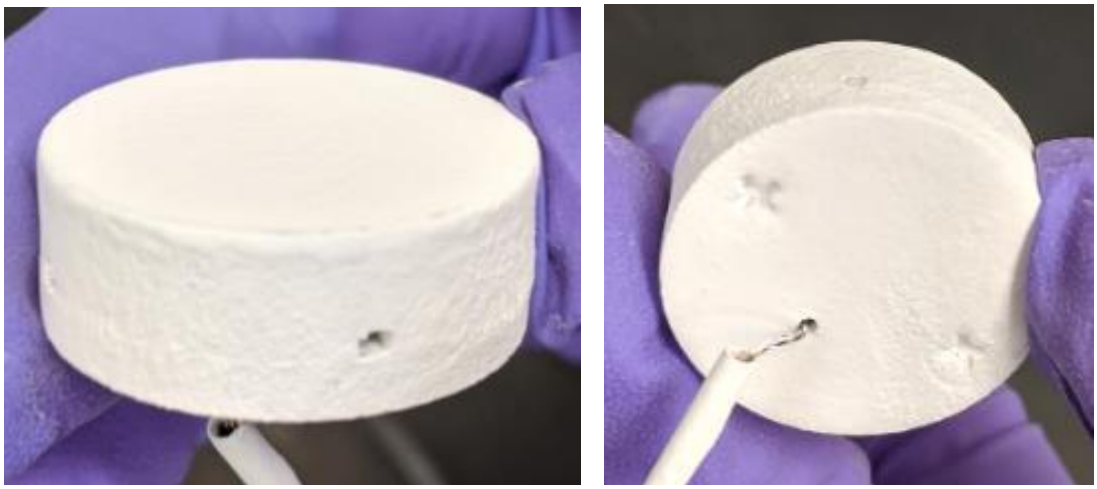

Figure 3-21. Front (left) and back (right) of the AZ-93 coated samples.

Figure 3-20 shows a sprayed sample and Figure 3-21 shows a sample painted with AZ-93. These are representative pictures and not the actual samples used in the testing described below. Note that all surfaces of the samples are coated, including the screw heads.

One way to estimate the solar absorptance of a coating is to measure the reflectance spectrum, as compared to Spectralon, and then integrate this spectrum against the solar spectrum. The measured solar absorbance for the spray-on sample tested in this document is 2.85% and for the AZ-93 coated sample it is 9.7% (both relative to Spectralon). (AZ Technology states that the solar absorbance of AZ-93 is 15 %, but we've obtained lower values when applying it onto smooth aluminum surfaces.)

A carefully constructed model of the chilldown of these two samples was created in order to obtain an estimate of the emissivity of the coatings. This model included the temperature variation of the heat capacity of 7075 aluminum (obtained by fitting data to NIST data for 6061 aluminum), a determination of surface area and mass of each sample, the thermal conductivity of the temperature

sensor wires carrying heat away from the samples, the thermal conductivity of the Kevlar strings (which turns out to be negligible), and 10 microwatts generated by the temperature sensor.

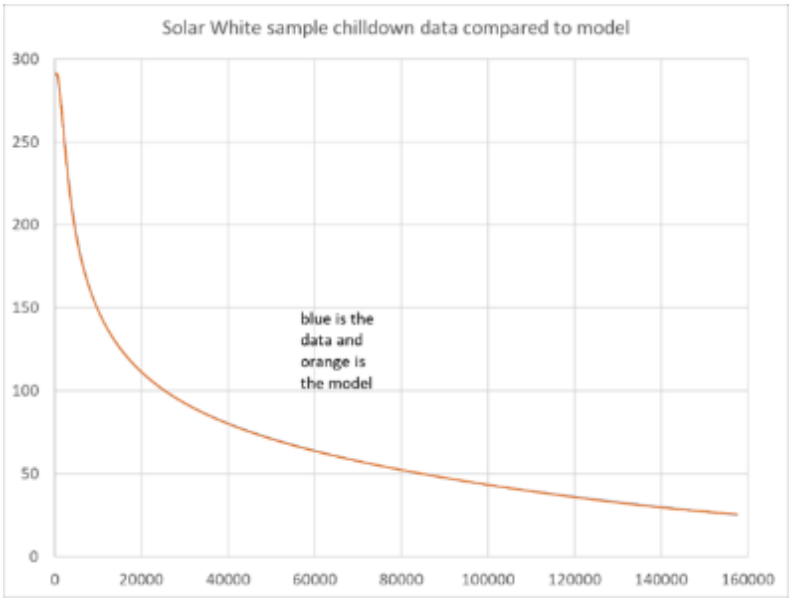

Figure 3-22. Chill down data and theory for the spray on sample.

Figure 3-22 shows the chill-down data (blue) for the solar white sample (degrees Kelvin versus time in seconds) and the theoretical fit (orange). The two are nearly identical, causing the theory curve to cover the data curve, however, an additional 70 microwatts of heat load on the sample had to be added to achieve this fit. It is not known where that heat is coming from. Also, an emissivity of 1 needed to be used, which was surprising since theory predicted an emissivity of around 0.8-0.9. However, this high emissivity was substantiated by GRC testing and is likely due to entrapped water in the spray on coating. This chilldown test was repeated with nearly identical results (65 microwatts of additional heating).

Figure 3-23 shows the chill-down data (blue) for the AZ-93 sample (degrees Kelvin versus time in seconds) and the theoretical fit (orange). The two are nearly identical causing the theory curve to cover the data curve, however, an additional 140 microwatts of heat load on the sample had to be added to achieve this fit. It is not known where that heat is coming from. The vendor stated that the emissivity for this coating was 0.91 and this value was used in the analysis to yield the curve shown in Figure 3-23. The extremely good agreement between theory and experiment substantiates the theory and supports the result that the spray on coating has an emissivity of about 1.

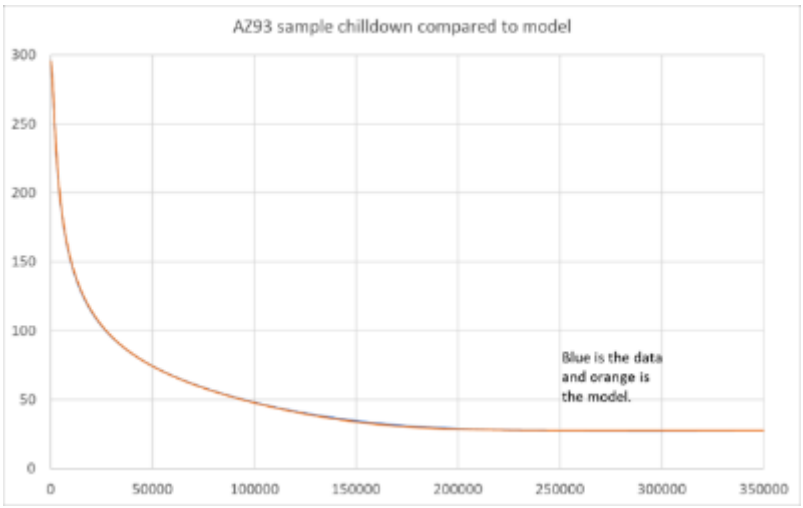

Figure 3-23. Chill down data and theory for the AZ-93 sample.

After a sample has chilled down, the lamp is turned on, illuminating the sample with simulated solar radiation with an estimated 714 mW of power. The front face of the sample has an area of 512 mm^2, so this is an average irradiance of 1.4 mW/mm. The deep space solar irradiance is about 1366 W/m^2 = 1.366 mW/mm^2, so the average irradiance inside of the chamber on these samples is roughly equal to one solar irradiance.

The first lamp on test is shown in the plot below and corresponds to the first chilldown data provided above. The model is the same as used for the chilldown except that the solar irradiance is now added as a heat source. So, the only free parameter is the solar absorptivity. The measured solar absorptivity for this sample was 2.85%, assuming that the reference, Spectralon, was perfect. Spectralon, however, is not perfect, having an estimated 1% absorption, though this might also be relative to another standard. The data below shows a very nice fit between the model and the data when an absorptivity of 4.13% is used, a reasonable result.

The lamp on test was repeated and the absorption increased to 5.13%. It was not known why the performance degraded, but subsequent testing showed that contamination was forming on the samples, likely due to outgasing from the Edmund Optics black coating. Even so, the fit between the model and the data is impressive.

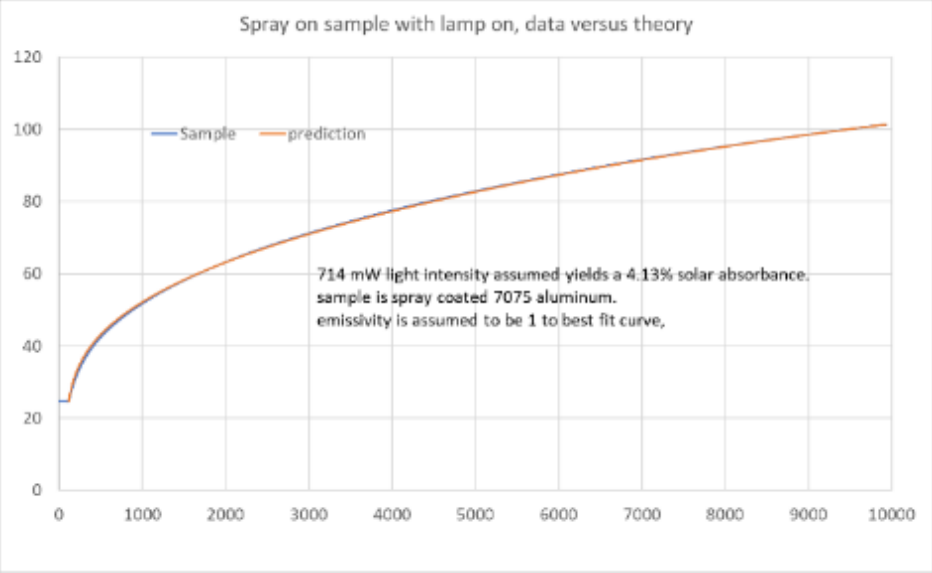

Figure 3-24. Lamp on data and theory for the spray on sample.

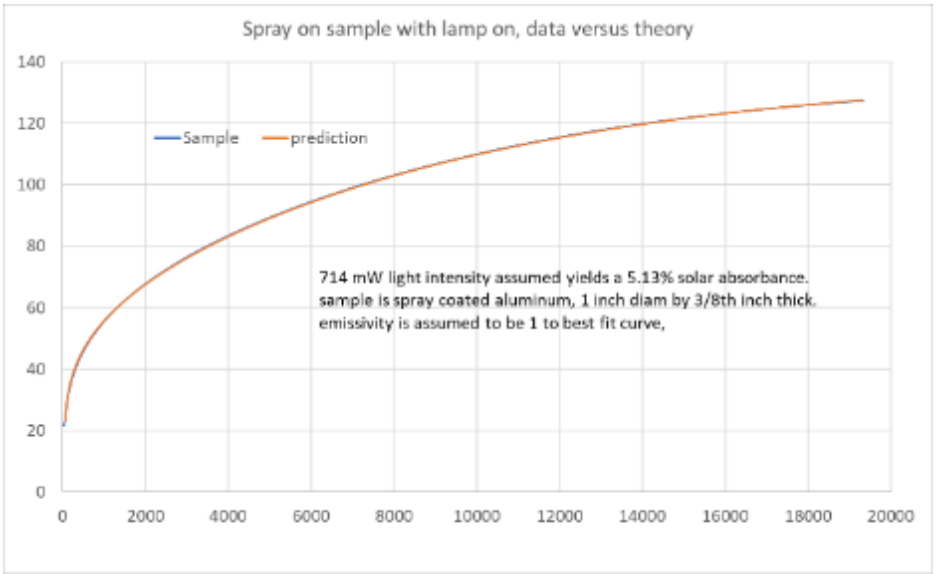

Figure 3-25. Lamp on data and theory for the spray on sample, run 2.

Figure 3-26 shows the lamp on data for the AZ-93 sample. In this case the model and the data did not agree as well as for the spray on sample data, so two different plots of solar absorptivity are shown. A solar absorptivity of 11.6% matched the data well for the first hour, but then the sample temperature increased a bit where after 18000 seconds it agreed more closely with an absorptivity of 11.76%. This might suggest that the solar absorptivity is temperature dependent, but that is not expected physically. More likely, the emissivity of AZ-93 drops a little with decreasing temperature (this would somewhat explain the increased low temperature plateau seen in the chill-down data, i.e., instead of adding extra heat to explain this it may be that the sample cannot emit energy as efficiently at low temperatures than at high temperatures.) The measured absorptivity of the AZ-93 coated sample using the spectral reflectance was 9.7%. So, adding about 2% to this

to account for the Spectralon offset to obtain the lamp-on solar absorptivity values is not unreasonable.

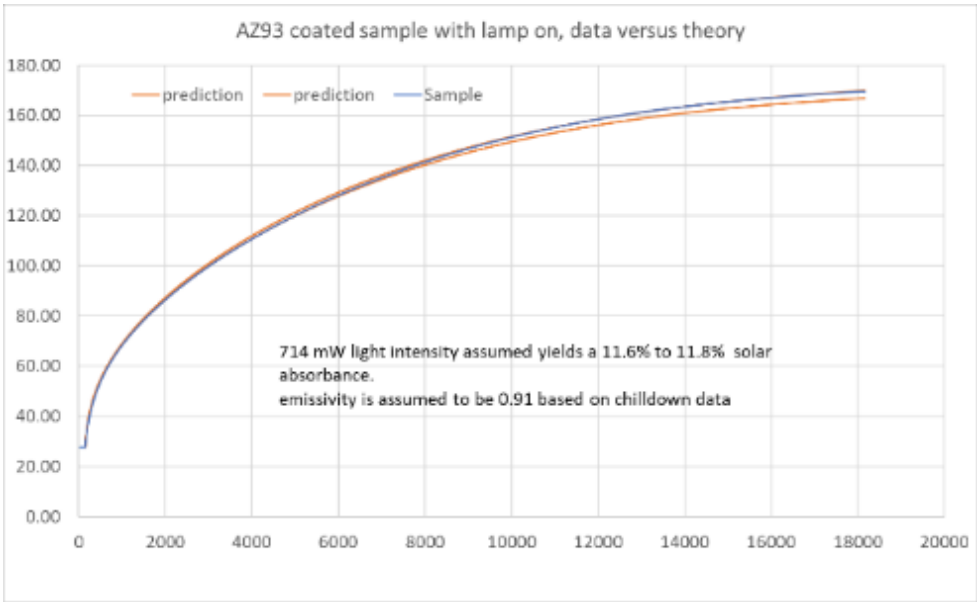

Figure 3-26. Lamp on data and theory for the AZ-93 sample.

3.5.4 Low Earth Orbit Testing

The deep space simulators provide a direct measurement of the amount of energy absorbed by a thermal control coating, but have shortcomings, primarily in not being accurate models of the solar irradiance. They do not generate correct amounts of ultraviolet nor mid-far infrared irradiance. In many cases, the error in solar absorptivity measurement caused by missing these spectral regions is not too significant, but when trying to reach a solar absorptivity less than 2-4 % it can be important.

This section of the report briefly presents a CubeSat experiment that was intended to compare the performance of the spray-on Solar White material to AZ-93 in low Earth orbit but begins with some in space testing that occurred on the International Space Station (ISS). On the outside of the ISS is a structure with the purpose of testing material response to the low-Earth orbit (LEO) environment, which includes atomic oxygen exposure and ultraviolet exposure. The Materials International Space Station Experiment (MISSE) uses this structure and has tested thousands of materials. Two different tiles, one composed of BaF_2 and one of Y_2O_3, have been mounted to this structure and exposed to the low earth orbit environment to gain information on their potential degradation resulting from atomic oxygen and ultraviolet radiation exposure.

3.5.4.1 MISSE-10 BaF_2

A small tile of BaF_2 was included in the MISSE-10 mission. This was launched to the ISS on Nov. 17, 2018 (during the NIAC Phase 2 project that occurred before the current Game Changing/Tech demo project being described in this report), installed in January 2019, and deployed on April 26, 2019. The MISSE-10 carrier was returned to Earth on January 13, 2021. The BaF_2 tile was located in the RAM position, facing into the direction of motion, which is a high exposure position. The net environmental impact is difficult to determine, but researchers with other samples in this tray has estimated that the net is 1.17 years of direct space exposure [17]. Figure 3-27 shows two photos

taken of this tile while mounted on the MISSE early in its deployment and a few months later, showing no signs of degradation in the visible.

Even though this sample returned to Earth in early 2021, data on its change in reflectivity were not measured until July of 2022 due to COVID shutdown restrictions at the Goddard Space Flight Center. The spectra for the sample before and after the mission are shown in Figure 3-28, where a small drop in reflectivity in the UV/blue region of the spectrum is seen. This corresponds to an increase in solar absorption from 4.4% to 6.7%. Note that the sample is recessed in its holder, causing it to be located a small distance from the entrance to the spectrometer integrating sphere and leading to a shift in the solar absorbance as discussed previously. So, the absolute number here is not important, but the change is. The sample degraded by 2.3%, which is very impressive given its location and exposure, however, it is not known if this degradation is caused by atomic oxygen or ultraviolet exposure.

Figure 3-27. Images of the BaF_2 tile on the MISSE carrier at two different dates.

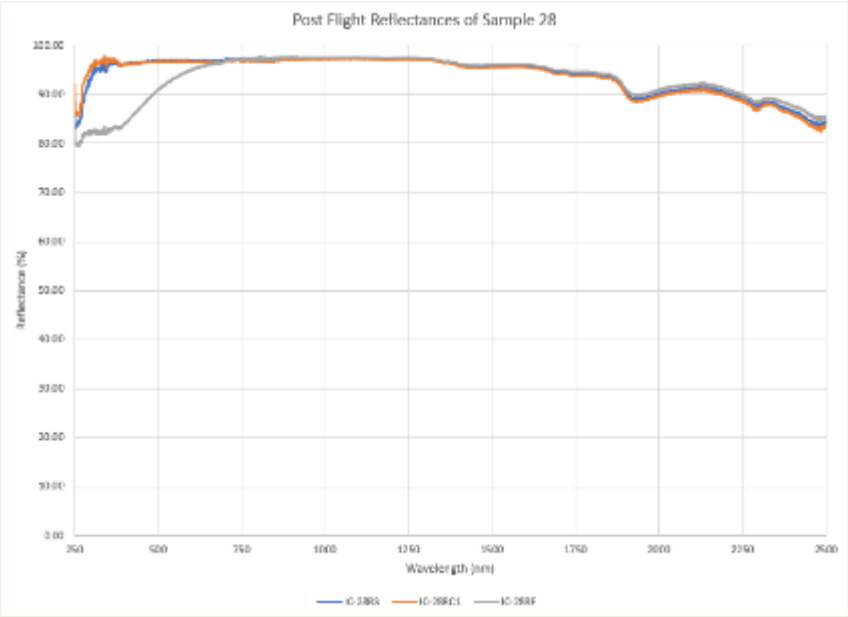

Figure 3-28. Comparison of pre (28RS and 28RC1) and post (28RF) flight spectral reflectivities of the MISSE-10 tile.

3.5.4.2 MISSE-11 Y_2O_3

A small tile of Y_2O_3 was included in the MISSE-11 mission. They were launched to the ISS on April 17, 2019 (before the current project started), installed in April 2019, and deployed in April 2019. The MISSE-11 carrier was returned to Earth on January 13, 2021. The Y_2O_3 tile was located in the Wake position, which is relatively protected. The actual net solar exposure has not been provided to us, but it has been indicated that our estimate of 1/10 outside time, is not unreasonable. This sample was outside of the ISS for 17 months, so its net solar exposure is roughly 1000 hours, with net atomic oxygen exposure even less. Figure 3-29 shows the MISSE-11 tray containing the Y_2O_3 tile, the white one, third row down, second from the right. Figure 3-30 shows the Y_2O_3 tile after the mission, still appearing to be bright white. Figure 3-31 shows the spectral reflectance of the MISSE-11 Y_2O_3 tile after the mission compared to a control tile. The measured solar absorbance changed from 7.1% to 7.7%, a small amount of degradation. Note again that the sample is recessed into its holder which will cause the reflectance measurement to be shifted downward. It is more important to note the change rather than the magnitude. This small degradation is impressive, though in contradiction to ground based exposure testing described in the sections below.

Figure 3-29. MISSE-11 tray containing the Y_2O_3 tile (white tile).

Figure 3-30. MISSE-11 Y_2O_3 tile after the mission.

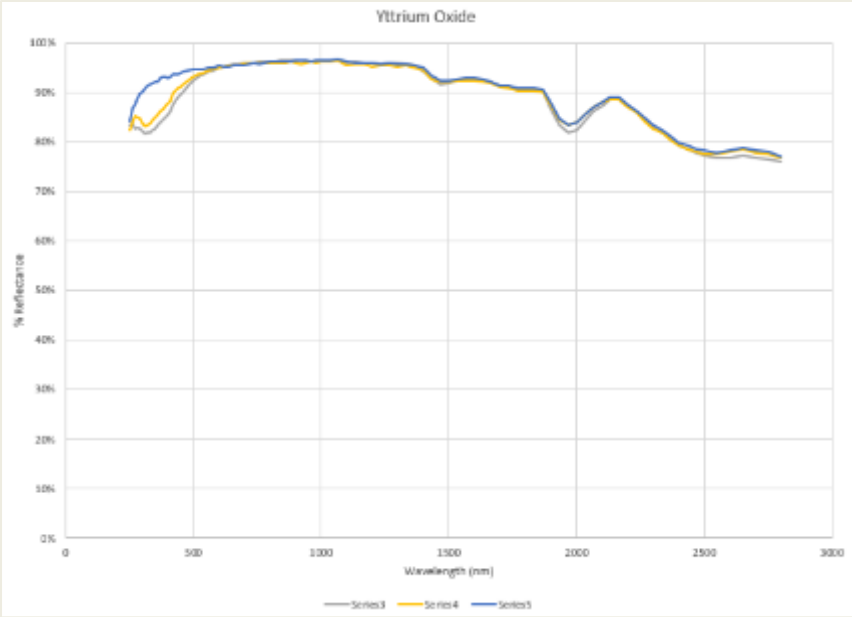

Figure 3-31. Spectral reflectance of the MISSE-11 Y_2O_3 tile after the mission (Series 3 and 4) compared to a control tile (Series 5).

3.5.4.3 MISSE-16 and Others-Ongoing

With the growing interest in the spray on coating it was decided that a sample of it should be placed in orbit for exposure testing. Figure 3-32 shows this sample, sprayed onto 7075 aluminum. It was launched on February 19, 2022 to the ISS and we presume it has been installed into the MISSE rack. The plan was to have it installed into the zenith position.

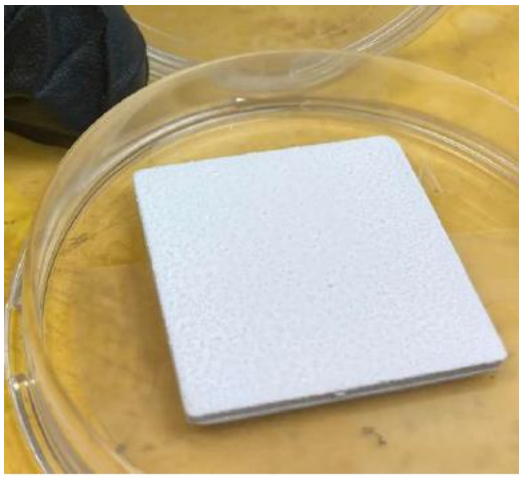

Figure 3-32. A spray-on sample prepared for MISSE-16.

Samples of BaF_2 tiles, Y_2O_3 tiles, and spray on coatings were delivered in July 2022, for an unspecified low Earth orbit test. Pictures and spectra for the flight samples are shown in section 3.5.4.1 above.

3.5.4.4 PATCOOL

The best test of the new material is to launch it into space and monitor its performance under actual sunlight unfiltered by the atmosphere. The Launch Service Program decided to do this and funded a program to design, construct, and launch a CubeSat for this purpose. The contract was given to the ADvanced Autonomous MUltiple Spacecraft (ADAMUS) Laboratory at the University of Florida (UF). They gave the project the title PAssive Thermal Coating Observatory Operating in Low-earth orbit (PATCOOL). This work has been published [9], so most of the details will not be presented here. Figure 3-33 shows a design model of the CubeSat containing solar panels, communications hardware, electronics, an orientation device, and the payload at top. The orientation device was required to aim the payload away from the infrared radiation of the earth, monitoring the performance of the samples only when seeing deep space or the Sun. Figure 3-33 also shows an exploded model of the payload. The blue discs are the samples being tested, two are spray on coatings and two are AZ-93 coated coupons.

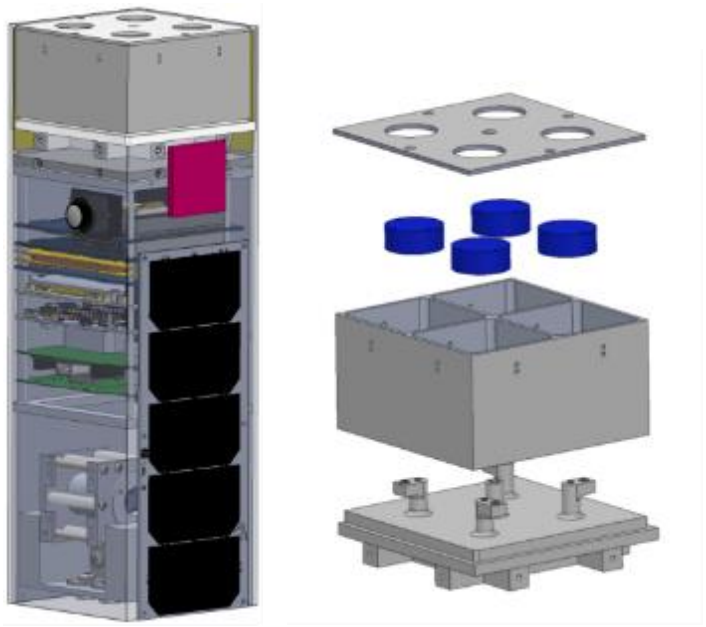

Figure 3-33. CubeSat (left) and an exploded view of the payload, with the samples in blue (right).

Figure 3-34 shows the final payload hardware with the four samples suspended by Kevlar strings. The samples consist of aluminum disks that hold temperature sensors and have paths cut into them to route the strings. The other photo shown is the final payload with the cover and a protective film in place. This was delivered from KSC to the UF team.

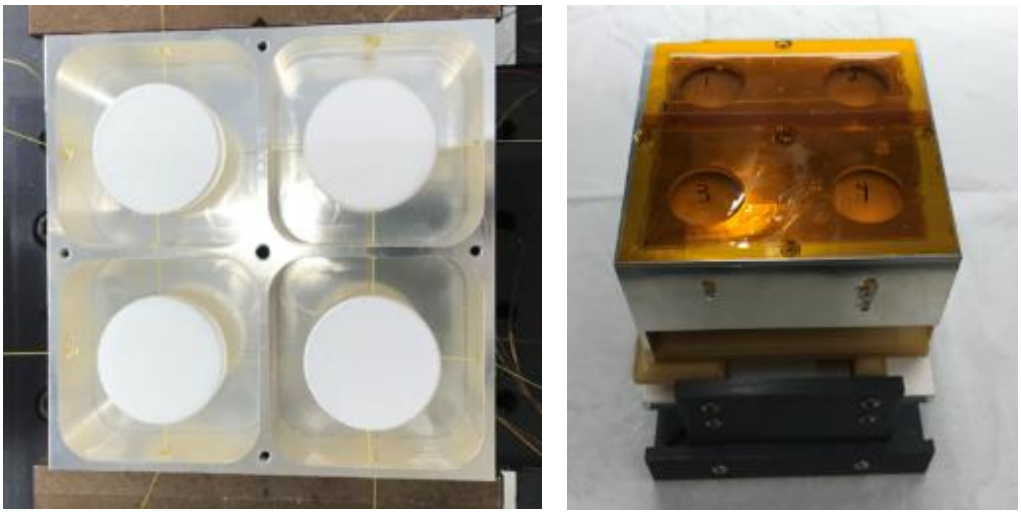

Figure 3-34. Exposed payload showing the samples suspended by Kevlar strings (left) and the delivered payload with cover and protective film (right).

Figure 3-35. CubeSat being launched from the ISS.

3.5.5 GRC Exposure Testing

A significant portion of the technology demonstration funded work was to perform laboratory measurements of the degradation of both the Y_2O_3 tiles and the spray on coating when exposed to atomic oxygen, ultraviolet radiation, and electrostatic build-up. This testing was performed at the Glenn Research Center and is described below.

3.5.5.1 Atomic Oxygen

Atomic oxygen degradation on the tiles and spray on coatings, versus exposure, is shown in Figure 3-36. The tiles begin in the 1-2 % range and degrade to above 4%, while the spray on coatings start at about 8% and degrade to about 12-13%. The degradation is shown in terms of total fluence (atoms/cm^2). As an example, during STS-8 an Atomic Oxygen Interaction Experiment was conducted [18]. The atomic oxygen flux seen in the ram position was 1.9×10^{15} oxygen atoms per second per cm^2. Using this value, the chart shown in Figure 3-36 corresponds to 9 days.

The tiles are not expected to be used in low-Earth orbit, so this degradation is not significant; however, the spray on coating may be used in this environment. So, it should be noted that the spray on coating may experience a degradation of 2-3% in its solar absorptivity during 2-3 days in the ram position on a spacecraft. It should also be pointed out that the MISSE-11 tile described above saw very little atomic oxygen due to its location on the MISSE rack.

Further details on the effect of atomic oxygen on the Y_2O_3 based materials is in the associated appendix.

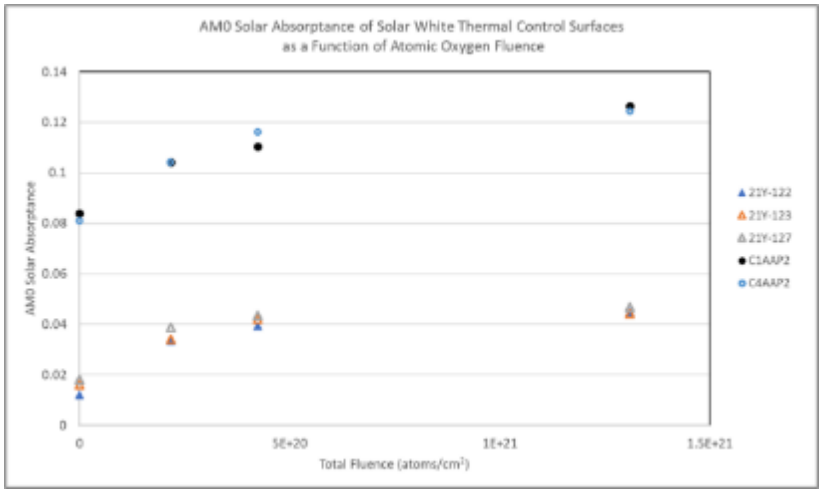

Figure 3-36. Solar absorbance of tiles and spray-on coatings vs. atomic oxygen fluence.

3.5.5.2 Ultraviolet

Ultraviolet exposure tests of the tiles and spray on materials were conducted by GRC and documented in the report provided in the associated appendix. A summary of the results is shown in Figure 3-37. The tiles began with a solar absorbance of about 1.2% and degraded steadily to a solar absorbance of about 28% after about 850 equivalent hours of full solar exposure. This result was unexpected, especially considering the relatively small degradation seen by the tile from MISSE-11 which saw roughly the same solar exposure. Consequently, efforts were expended to understand this discrepancy and a summary of the results of that effort are provided in section 3.5.5.4. Note that the spray on coating showed similar degradation and the expectation is that this is primarily due to the Y_2O_3 and not the KBr in the coating. So, the discussion in section 3.5.5.4 should apply to both the tiles and the spray on coating. However, as an assurance, as mentioned above, a spray on sample is currently on the ISS as part of MISSE-16.

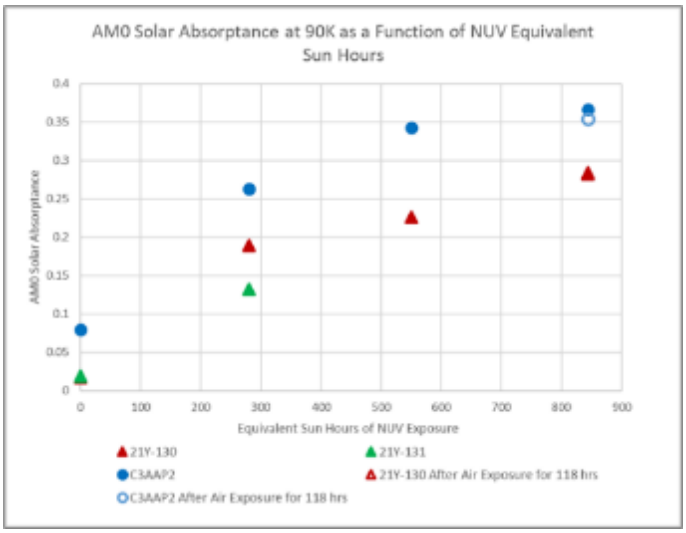

Figure 3-37. Solar absorbance of tiles and spray on coatings versus NUV equivalent Sun hours.

3.5.5.3 Electrostatic

Electrostatic build-up and discharge experiments have been performed on both the tiles and the spray on coating. The details are provided in the associated appendix but show that the tile is sufficient thick that it will not arc in either low earth orbit or geosynchronous orbit due to charge build up. However, the spray on coating, being only a few mils thick did arc in a simulated geosynchronous orbit, but not in low earth orbit where sufficient dissipation exists. It should be noted that the testing was limited and whether the arcing identified is an issue or not is mission dependent. Further investigation will be needed to fully understand the arcing and if potential mitigations are required.

3.5.5.4 Y_2O_3 Ultraviolet Degradation

The laboratory induced ultraviolet degradation of Y_2O_3 was surprising, given that it predicted a 25% increase in solar absorption after 800 hours of full sun exposure, but the sample returned from MISSE-11 had less than a 1% after a similar amount of actual solar exposure. An effort was started to try and understand this discrepancy since this large difference in degradation strongly affects the applicability of the material as a solar reflector/thermal control coating. In addition to trying to understand the degradation itself, three avenues were explored to try and resolve the difference between the lab and the MISSE-11 results: contamination, thermal recovery, and solar simulation issues.

3.5.5.4.1 Contamination

It was possible that the laboratory handling of the samples contaminated them, leading the enhanced ultraviolet sensitivity. With that in mind X-ray Diffraction (XRD) analysis and X-ray photo-electron spectroscopy (XPS) as well as scanning electron microscope (SEM) imaging were performed on the exposed samples to measure what elements were present.

SEM analysis showed slight presence of Al and perhaps Si, as well as lower concentration of oxygen in the UV exposed sample. XPS analysis of the reference sample (i.e., an unexposed sample) Y2O3 (21-Y-123) showed a surface layer of carbon (normal on most samples), with no evidence of any other trace contaminants. But XPS analysis of the exposed sample showed a thin

layer (150 to 200 Å thick) of SiO_x in addition to the carbon layer. There was also a trace amount of fluorine present on the surface. Table 3-2 shows the concentrations measured on the surface of the two samples.

Table 3-2. Contamination differences between the unexposed and exposed samples.

XPS Analysis of Y_2O_3 Before and After UV Exposure Atomic Concentrations (at.%)							
Sample	**C**	**O**	**Y**				
Unexposed 21Y-123	32.4	43.5	24.1				
Sputtered 1 min (100 Å)	29.8	43.1	27.1				
	C	**O**	**Y**	**Si**	**F**		
UV1 21-Y-130	31.4	47.7	5.2	16.0	0.4		
Sputtered 1 min (100 Å)	25	51.2	7.5	15.4	0.3		

The source of the fluorine is believed to be the vacuum grease used to seal the UV exposure chamber. The source of the silicon oxide is not known. However, even though the exposed samples had contamination not present on the unexposed samples, the discoloration of the surface is not due to this surface contamination. The discoloration is deeper than the contamination indicating that it is not the source.

3.5.5.4.2 Oxygen Deficiency

Shortly after the laboratory exposure work was complete, it was stated that the discoloration was caused by loss of oxygen; that the ultraviolet photons had somehow caused oxygen to be lost from the Y_2O_3. The alternative belief was that the ultraviolet photons had caused the oxygen atoms in the crystal structure to shift from their lowest energy position to a new position that perturbed the material structure such that it becomes a UV/blue absorber. This second hypothesis is referred to as color center formation. Performing a literature search located a reference [19], substantiating the ultraviolet induced color change being caused by oxygen deficiencies. One of applicable results described in this publication was that the degree of color change is related to the energy, or wavelength, of the ultraviolet radiation. The study exposed zirconia samples to 243 nm radiation and a similar intensity of 365 nm radiation. After 24 hours the color change of the samples exposed to the shorter wavelength was six times that of the longer wavelength exposed samples. However, this didn't resolve the oxygen issue.

3.5.5.4.3 Thermal Recovery

A sample of discolored material was heated in air for two hours at 1375 °C and it recovered. Reflectivity measurements indicated a complete recovery. Figure 3-38 shows the before and after heating photos. However, even though thermal recovery is a promising result, it does not indicate if oxygen is being returned to the sample from the air (the argument for this is referred to as bleaching) or if the oxygen atoms were being thermally agitated back to their ground state locations in the crystal matrix.

Figure 3-38. Discolored Y_2O_3 tile before (left) and after (right) heating in air.

To finally resolve this, a discolored sample was heated to 1375 °C in argon for two hours, with no oxygen present. The sample recovery photos are shown in Figure 3-39, affirming that the oxygen atoms were still present in the material. It should be mentioned that 100-300 nm wavelength light is required to eject electrons from some materials and that an oxygen atom weighs roughly 32,000 times an electron, so it was highly unlikely that the ultraviolet light being used could detach and then eject an oxygen atom from the crystal.

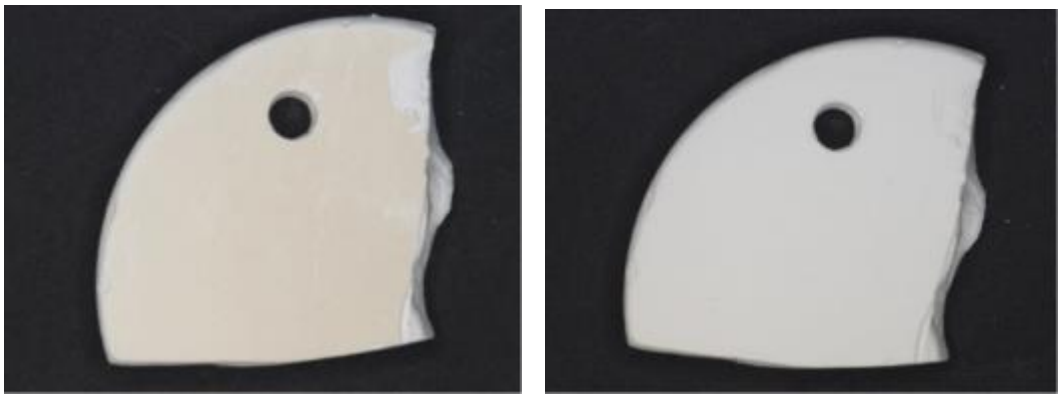

Figure 3-39. Discolored Y_2O_3 tile before (left) and after (right) heating in argon.

This result, that the discolored Y_2O_3 can heal thermally from ultraviolet degradation, partially explains the difference between the samples exposed to ultraviolet radiation in the chamber versus the one from MISSE-11. The MISSE-11 sample had more than a year on the MISSE rack during which time it could heal. Even though it wasn't at 1375°C, it would still have healed but at a slower rate. Gathering more data on the degradation rate versus healing rate as a function of temperature would allow a determination of the steady state degradation, where damage and healing balance, at a chosen temperature.

3.5.5.4.4 Solar Simulation Issues

Another possible reason that the laboratory exposure degradation rate does not appear to agree with the flight sample is, as reported in reference 19, that the discoloration is preferentially caused by wavelengths in the 200-250 nm range rather than the 300-400 nm range. This makes sense in

that Y_2O_3 crystals have minimal absorption beyond 250 nm, so those longer wavelength photons initially just pass through the material. However, the laboratory analysis arbitrarily chose to compare the integrated solar spectrum from 200-400 nm to that of the Hg-Xe lamp being used, claiming that this spectral range was important, but without any justification. Figure 3-40 shows plots of the two spectra (one the same scale) where the Hg-Xe lamp integrated intensity is claimed to be twice that of the integrated solar spectrum. This factor of two was then used to scale the sample degradation rate to find a solar irradiance degradation rate.

There are two issues with how that factor of two was found. The first is that the Hg-Xe lamp spectra is measured too coarsely. The dots shown in Figure 3-40 are the measurements and most of the peaks shown have only one measurement point. It is not reasonable that the measurements happened to be at the peaks, so the actual peaks may be higher, or some peaks even missed (depending on the bandwidth of the measurements). So, this spectrum is not adequate upon which to make a comparison with the Sun. The second issue, as alluded to previously, is that the 200-400 nm band is arbitrary. If instead a band from 200-250 nm had been used, the conversion factor would have been different. 21% of the displayed Hg-Xe irradiance in the 200-400 nm band is in the 200-250 nm band. But only 2% of the Sun's irradiance in the 200-400 nm band is in the 200-250 nm band. So instead of a factor of 2 there is a factor of 20 times more irradiance in the laboratory lamp than is generated by the Sun, assuming only the 200-250 nm band is important.

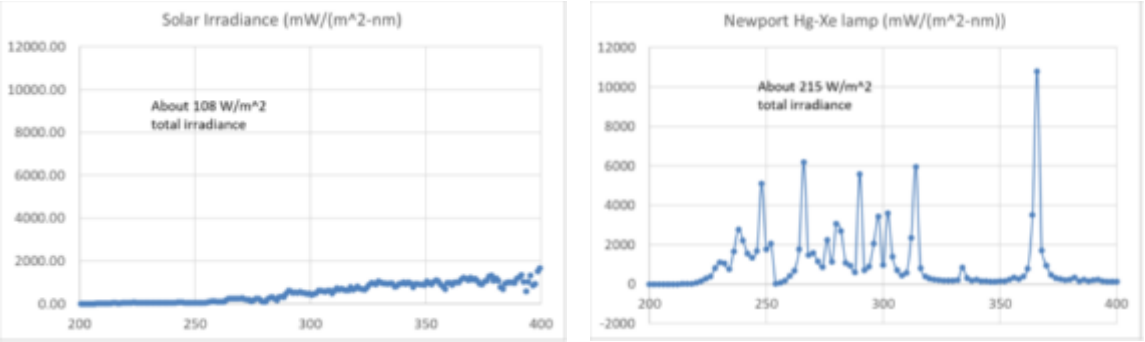

Figure 3-40. Solar irradiance (left) and solar simulator (right) spectra from 200-400 nm.

The arbitrariness of choosing a 200-400 nm band for comparison with the Sun, coupled with the thermally induced healing, may explain why the MISSE-11 sample showed so little degradation compared to that of the sample exposed to the laboratory lamp.

4.0 CONCLUSION

The development and testing of Y_2O_3 based solar reflective materials have been advanced considerably by this effort. However, the Y_2O_3 based tiles may not be appropriate for use on a deep space cryogenic depot, which was the original goal. The tiles need to reflect about 99% of the Sun's energy, which has been achieved, however, tiles composed of Y_2O_3 will degrade under solar irradiance. The degradation may be much slower than what was seen in the lab, but in this application the tiles will be cold, most likely significantly decreasing the recovery of the material. A full analysis has not been done, comparing the rate of degradation to the rate of recovery versus temperature, but based on current data it is unlikely that Y_2O_3 based tiles will maintain sufficient reflectance for this long-term application.

The spray on coating is being considered for short term applications, e.g., minimizing the solar heat load on a cryogenic tank being used to deliver cryogens. Consequently, this coating may still be used for missions of sufficiently short duration that the degradation of the spray on coating due to atomic oxygen and ultraviolet irradiance are not significant. Many missions currently use AZ-93 which has a solar absorbance in the 15% range, while the Y_2O_3 based coating has a lab measured solar absorbance of only about 4%. On potential user stated that even if the lab measurement degraded by a factor of 2 (to 8%) that it would still be a worthwhile coating.

A small follow-on project will occur in FY23 to attempt to answer two important questions raised by the work done to date.

a. What is the ultraviolet degradation rate of BaF_2 based tile?

One of the interesting results from the work described above is that the BaF_2 tile on MISSE-10 suffered only minor degradation after more than a year in the RAM position on the MISSE rack. It is likely that this degradation was primarily caused by the interaction with atomic oxygen, resulting in the formation of barium oxides. If so, then BaF_2 may have very minimal degradation due to ultraviolet irradiance and may be a candidate for coating a future deep space cryogenic storage tank. In FY23 the degradation of BaF_2 under solar UV will be explored.

b. What is the ultraviolet degradation rate of the spray on coating in low earth orbit?

The rate of degradation of the spray on coating under solar ultraviolet irradiance is not known but is needed. As with the tiles, the laboratory measurements show rapid degradation, but this has been discounted for the tiles, as described above, and will likely also be discounted for the spray on coating. Measurements of the spray on coating UV degradation will be made and, hopefully, the sample from MISSE-16 will return to provide on-orbit data.

5.0 REFERENCES

1. Youngquist, Robert C., and Mark A. Nurge. "Achieving cryogenic temperatures in deep space using a coating." *Optics Letters* 41, no. 6 (2016): 1086-1089.
2. Cryogenic Selective Surfaces - NASA Technical Reports Server (NTRS)-final report on Phase 1 NIAC
3. Patent 10273024, “Radiation reflector and emitter”, April 30, 2019.
4. Youngquist, Robert C., Mark A. Nurge, Wesley L. Johnson, Tracy L. Gibson, and Jan M. Surma. "Cryogenic deep space thermal control coating." *Journal of Spacecraft and Rockets* 55, no. 3 (2018): 622-631.
5. Cryogenic Selective Surfaces - NASA Technical Reports Server (NTRS)-final report on Phase 2 NIAC
6. Patent 10815129, “Method of fabricating rigid radiation reflectors”, October 27, 2020
7. Patent Pending, Patent Application Serial Number 16/575720, “Reflective Paint for Cryogenic Applications”.
8. Solar Surfing: Final Report on a Phase I NASA Innovative Advanced Concepts Study - NASA Technical Reports Server (NTRS)
9. Passive Thermal Coating Observatory Operating in Low-Earth Orbit (PATCOOL) – Cubesat Design to Test Passive Thermal Coatings in Space - NASA Technical Reports Server (NTRS)
10. Y2O3 Based Spray-On Cryogenic Thermal Control Coating Study - NASA Technical Reports Server (NTRS)
11. Manufacturing of Rigid Y2O3 Tiles for Cryogenic Thermal Coatings - NASA Technical Reports Server (NTRS)
12. Swanger, A. M., A. Krenn, R. Youngquist, and T. L. Gibson. "Development of a space irradiance simulator for advanced studies and materials research." In *IOP Conference Series: Materials Science and Engineering*, vol. 1240, no. 1, p. 012006. IOP Publishing, 2022. Development of a Space Irradiance Simulator for Advanced Studies and Materials Research - NASA Technical Reports Server (NTRS)
13. Cryogenic Thermal Control Coatings: An Overview - NASA Technical Reports Server (NTRS)-A presentation by Angela Krenn.
14. Alavi, S., Joffin, N., Verelst, M., and Caussat, B. “Crystallization of microscopic Y_2O_3 powders by different techniques of fluidization at high temperature.” *Chemical Engineering Journal* Vol 125, Issue 1 (2006): 25-33.
15. Aluminum Aircraft Parts: Clad Aluminum Vs Bare Aluminum | AAA Air Support
16. Kubelka, Paul, and Franz Munk. "An article on optics of paint layers." *Z. Tech. Phys* 12, no. 593-601 (1931): 259-274.
17. Kim K. de Groh and Bruce A. Banks, “MISSE-Flight Facility Polymers and Composites Experiment 1-4 (PCE 1-4)”, NASA Technical Memorandum NASA/TM-20205008863, Feb. 2021.
18. James Visentine, “Atomic Oxygen Effects, Measurements for Shuttle Missions, STS-8 and 41-G”, NASA technical memorandum 100459, September 1983.
19. Han, A., et. al. “Prolonger UV-C Irradiation is a Doubled-Edged Sword on the Zirconia Surface”, ACS Omega 2020, 5, pp. 5126-5133.

APPENDIX A: ACRONYMS

Acronym	Definition
ACL	Applied Chemistry Laboratory
ADAMUS	ADvanced Autonomous MUltiple Spacecraft
APS	Average Particle Size
COPVs	Composite Overwrap Pressure Vessel
CTC	Cryogenic Thermal Coating
FY	Fiscal Year
GRC	Glenn Research Center
ISS	International Space Station
KSC	Kennedy Space Center
LEO	Low-Earth Orbit
LSP	Launch Services Program
MISSE	Materials International Space Station Experiment
MLI	Multi-layer Insulation
NIAC	NASA Innovative Advanced Concepts
NIST	National Institute of Standards
NTP	Nuclear Thermal Propulsion
PATCOOL	Passive Thermal Coating Observatory Operating in Low-Earth Orbit
REO	Rare Earth Oxide
SEM	Scanning Electron Microscope
TPSF	Thermal Protection Systems Facility
TRL	Technology Readiness Level
UF	University of Florida
UV	Ultraviolet
XPS	X-ray Photo-electron Spectroscopy
XRD	X-ray Diffraction

APPENDIX B: SYNTHESIS AND PROPERTIES SYNTHESIZED Y_2O_3 PARTICLES

Synthesis

The following method was used to synthesize high purity yttrium oxide nanopowders. Yttrium nitrate [$Y(NO_3)_3$] is dissolved in nanopure water in a fleaker to yield an aqueous solution of yttrium nitrate. Ammonium sulfate [$(NH_4)_2SO_4$] is added to the fleaker and dissolved. Ammonium bicarbonate [NH_4HCO_3] is dissolved in nanopure water in a separate beaker. Alternatively, aqueous ammonium hydroxide [NH_4OH] is used as a precipitating agent. The yttrium nitrate solution is stirred while either the ammonium bicarbonate or ammonium hydroxide is added dropwise. After addition is complete, the precipitant is allowed to age for a specified duration, stirring continuously during this time. Upon completion of aging, the resulting white slurry of $Y_2(CO_3)_3$ or $Y(OH)_3$ is transferred to tubes which are then centrifuged. The supernatant is discarded and nanopure water added. The product is then resuspended using a vortex mixer followed by sonication. These steps are repeated for a total of four washes in nanopure water, and two washes in absolute ethanol. Upon completion of the washes the resulting white powder (yttrium carbonate or yttrium hydroxide depending on the precipitating agent used) is transferred to a crucible and dried at 70 °C in a vacuum oven overnight. The dried yttrium carbonate/yttrium hydroxide powder is then calcined inside an oven to yield yttrium oxide. Variables assessed in this synthesis procedure include the addition rate, calcination temperature, reaction temperature, aging time, yttrium nitrate concentration, and ammonium sulfate concentration.

Reagent Purity:
Yttrium nitrate hexahydrate: 99.8% purity (trace metal basis)
Ammonium bicarbonate: >99.5% purity
Ammonium sulfate: >99.0% purity
Ammonium bicarbonate: >99.5% purity
Ammonium hydroxide: 28-30% in H2O

Material Analysis-Powders

Synthesized powders were analyzed to determine purity and morphology. Inductively Coupled Plasma (ICP) was used for purity analysis and Scanning Electron Microscopy (SEM) was used to determine morphology. A Thermo Scientific iCAP 7000, Inductively Coupled Plasma Optical Emission Spectroscopy Instrument, was used to assess the purity of two batches of synthesized yttria. Yttria powders were digested in nitric acid; the resulting solution was then diluted with nanopure water and filtered. Samples were then analyzed for 28 different elements via ICP-OES. Whenever possible, elements were analyzed at more than one wavelength so that interferences could be identified. In order to obtain a worst-case estimate of purity, the highest concentration indicated by the analyzed peaks was included in the final purity calculation. In some instances, an element could only be measured at a single wavelength; this was due to the high concentration of yttrium in the sample causing interferences (peak overlap) that made it difficult to quantify trace amounts of particular elements. In instances where unusually high levels of an element were indicated by ICP-OES, Energy-Dispersive Spectroscopy (EDS) was employed to confirm gross contamination (>1.0%) was not present. Both batches analyzed were determined to have less than 1% contamination for the elements analyzed, indicating they were >99% pure. ICP results of synthesis 20210928-1 are shown below in Table B-1.

Table B-1. ICP results for synthesized powder 20210928-1.

Element/Wavelength/Position	Measured Concentration (ppm)	Wt% of Dry Sample
Ag 338.289 {100} (Radial)	13.8931947	0.13893
Al 167.079 {502} (Radial)	0.332593423	<0.01
As 189.042 {478} (Axial)	-0.071	<0.01
Ba 455.403 {74} (Radial)	0.375649972	<0.01
Be 313.107 {108} (Radial)	0.008	<0.01
Ca 393.366 {86} (Radial)	0.79306296	<0.01
Cd 226.502 {449} (Axial)	0.302254655	<0.01
Co 228.616 {447} (Axial)	0.237083119	<0.01
Cr 283.563 {119} (Radial)	5.894702404	0.05895
Cu 324.754 {104} (Radial)	0.038778059	<0.01
Fe 259.940 {130} (Radial)	0.396851727	<0.01
K 766.490 {44} (Axial)	6.07679917	0.06077
Li 323.263 {104} (Radial)	1.691283347	0.01691
Mg 280.270 {120} (Radial)	2.196190917	0.02196
Mn 257.610 {131} (Axial)	0.05736368	<0.01
Mo 202.030 {467} (Axial)	0.034113796	<0.01
Na 589.592 {57} (Radial)	2.281	0.02281
Ni 216.556 {456} (Radial)	0.17007352	<0.01
Pb 220.353 {453} (Axial)	1.355060981	0.01355
S 180.731 {487} (Axial)	18.685	0.18685
Sb 206.833 {463} (Axial)	0.071	<0.01
Se 196.090 {472} (Axial)	-0.150396547	<0.01
Si 251.611 {134} (Axial)	35.3501815	0.353
Sr 407.771 {83} (Radial)	0.354835109	<0.01
Ti 334.941 {101} (Axial)	1.112863848	0.01113
Tl 190.856 {477} (Axial)	1.227	0.01227
V 292.402 {115} (Axial)	0.174803088	<0.01
Zn 213.856 {458} (Radial)	0.213822829	<0.01

A TESCAN AMBER 58252G FIB-SEM (S/N 119-0216), scanning electron microscope, was used to determine the morphology and size of synthesized yttria particles. Figure B-1 shows SEM images from two synthesis attempts with particles sizes in the desired 50-200 nm size range.

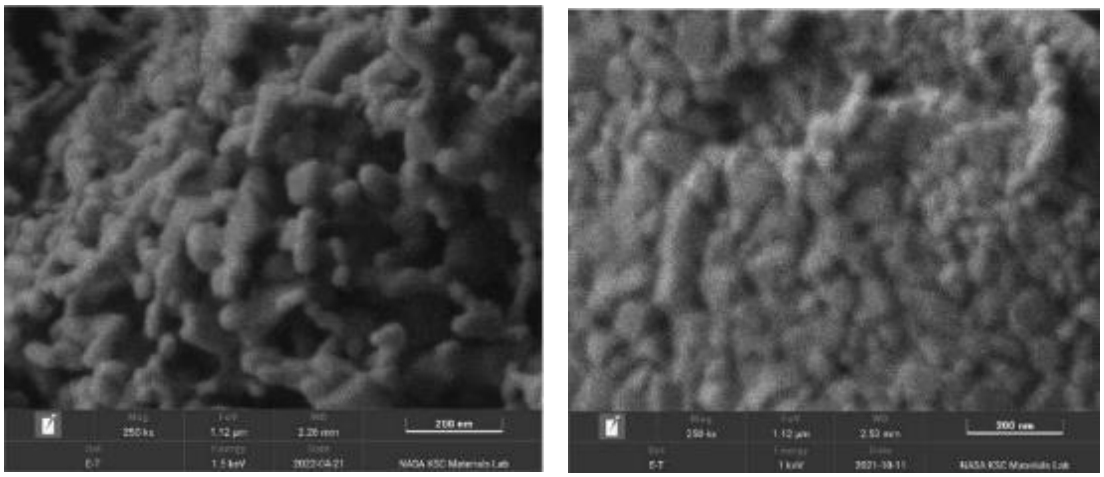

Figure B-1. Synthesis 20220419 (left) and Synthesis 20211004-3 (right).

Material Analysis-Rigid Tiles

Rigid tiles were fabricated from synthesized yttria powders and analyzed to determine their morphology and optical performance. Scanning Electron Microscopy (SEM) was used to determine morphology and semi-hemispherical reflectance was used to determine optical performance. Based on the spectral data collected, the percent solar absorption for the powders was calculated using ASTM E-490 data for the Sun integrated from 200 nm to 2400 nm (ASTM E903 Standard Test Method for Solar Absorptance, Reflectance, and Transmittance of Materials Using Integrating Spheres).

A TESCAN AMBER 58252G FIB-SEM (S/N 119-0216) was used to determine the morphology and size of synthesized yttria particles in fabricated rigid samples. Figure B-2 shows images from two fabricated rigid tile samples made from synthesized yttria powders. These images give an approximation of void volume as well as particle size distribution.

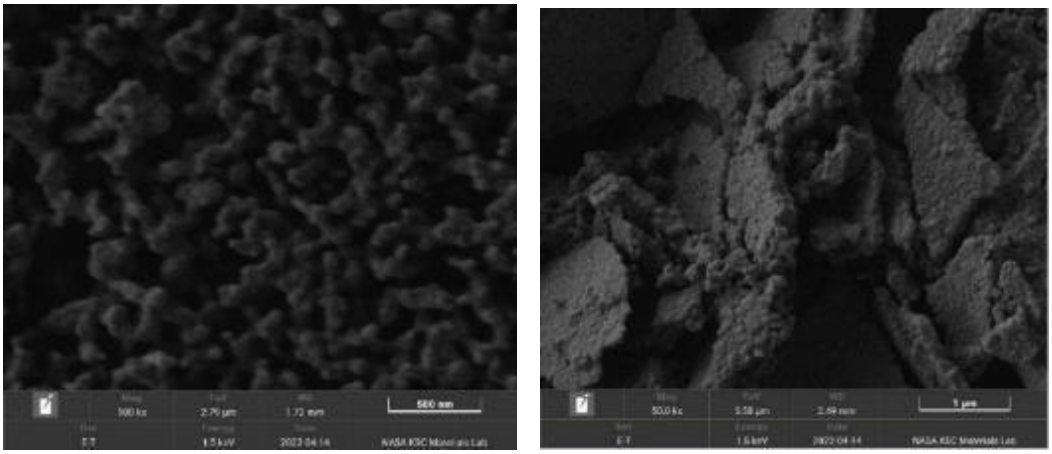

Figure B-2. Rigid samples FY22-13 (left) and FY22-14 (right).

A Jasco V-770 with the ISN-923 integrating sphere accessory was used to measure the percent reflectance (%R) of rigid samples made from synthesized yttria powders. Solar absorptivity values

as low as -1% (one percent better than the NIST reference) were obtained. This is as good as with the better vendor supplied material and demonstrates that the synthesized yttria can be used in the fabrication of high-quality tiles.

Material Analysis-Spray-On Coatings

Spray-on coatings were fabricated from synthesized yttria powders and analyzed to determine their morphology and optical performance. SEM was used to determine morphology and semi-hemispherical reflectance was used to determine optical performance. A TESCAN AMBER 58252G FIB-SEM (S/N 119-0216) was used to image the surface of 7075 coupons coated with paints made from synthesized yttria powders.

Figure B-3 shows an yttria based paint made from synthesize yttria powder on a 7075 aluminum coupon. The left image in Figure B-3 shows regions of potassium bromide (white) and yttria (grey) on the painted surface of the 7075 coupon. The center image in Figure B-3 shows an yttria region on a 7075 coupon; several particle sizes and morphologies can be observed. Figure B-3, right image, shows a region of potassium bromide crystal on the painted surface.

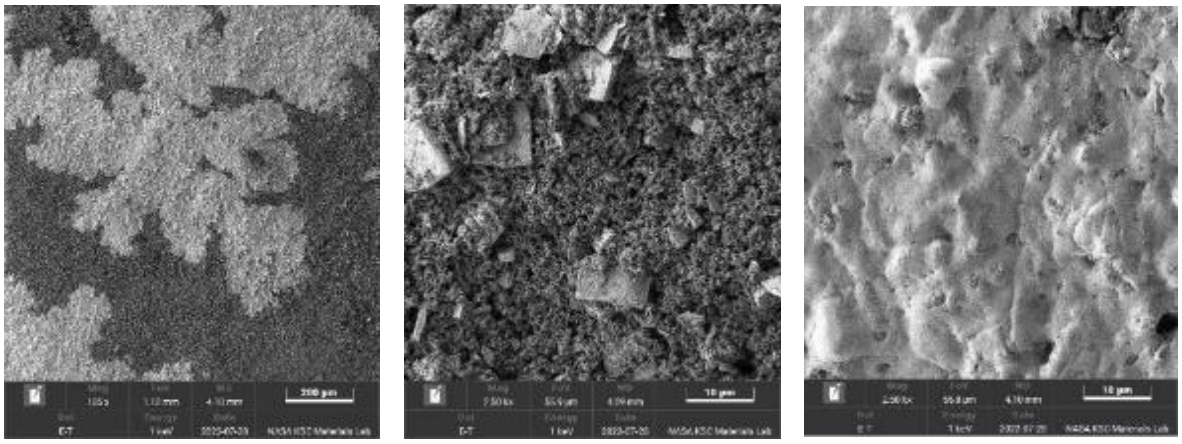

Figure B-3. Yttria paint on a 7075 coupon.

A Jasco V-770 with the ISN-923 integrating sphere accessory was used to collect spectra of 7075 aluminum coupons coated with paints made with synthesized powders. Solar absorptivity values as low as 2.3% (compared to the NIST reference) were obtained. This is as good as with the better vendor supplied material and demonstrates that the synthesized yttria can be used in the fabrication of a spray on coating.

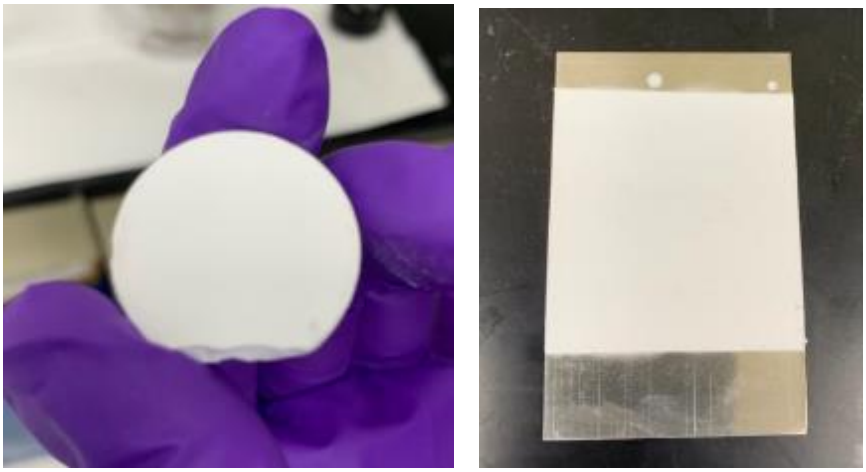

Figure B-4. Tile (left) and sprayed aluminum panel (right) composed of synthesized yttria.

APPENDIX C: THE GLENN RESEARCH CENTER DEEP SPACE SIMULATOR, DESIGN AND TESTING RESULTS

Summary

Solar White thermal control coating samples, produced by the Kennedy Space Center (KSC), were tested at to Glenn Research Center (GRC) to characterize the thermal performance of the material in a simulated deep space environment and expose the material to relevant low earth orbit environment exposure simulations, including atomic oxygen (AO), ultraviolet (UV) light, and electrostatic charging (EC). A description of the Deep Space Solar Simulator (DS^3) testing methodology, test results, and analysis is provided below. Results of the AO, UV, and EC will be discussed in separate reports.

Test Plan – Needs, Goals, and Objectives

Needs

- Characterize Solar White tile and spray-on coating absolute thermal performance, solar absorption versus thermal emittance.
- Characterize Solar White tile and spray-on coating optical performance degradation due to typical LEO-environmental exposure.

Goals

- Assess solar absorptance and thermal emittance of Solar White tile and spray-on coating using deep-space environmental chamber (absolute measurement).
- Expose Solar White tile and spray-on coating to simulated relevant environment exposures including atomic oxygen exposure, UV exposure, and electrostatic charging.
- Measure solar absorptance and thermal emittance of Solar White tile and spray-on coating, before and after simulated exposure testing.

Secondary Goal

- Demonstrate the ability to model the solar white material performance in thermal software and evaluate solar white material capabilities under various application scenarios.

Primary Objectives

- Construct and verify operation of Deep-Space Solar Simulator (DS^3) for quantifying absolute thermal performance of Solar White material under deep-space-like cold background and 1 sun solar irradiance conditions.
- Construct thermal model to characterize thermal energy balance of DS^3 and sample material.
- Perform DS^3 testing to measure the temperature of Solar White tiles and Solar White spray-on samples while under simulated deep space environment. The DS^3 will be tested under both infrared (IR) only conditions (light OFF) and solar simulated conditions (light ON).
- Expose Solar White tiles and Solar White spray-on samples to atomic oxygen representative of LEO exposure with intermittent checks, using spectrophotometry, to assess degradation over time.

- Expose Solar White tiles and Solar White spray-on samples to UV representative of LEO exposure with intermittent checks, using spectrophotometry, to assess degradation over time.
- Expose Solar White tiles and Solar White spray-on samples to electrostatic charge testing representative of LEO and GEO exposure.

Secondary Objectives

- Perform DS^3 testing to measure the temperature of Solar White tiles and Solar White spray-on samples while under simulated deep space environment after AO exposure.
- Perform DS^3 testing to measure the temperature of Solar White tiles and Solar White spray-on samples while under simulated deep space environment after UV exposure.

Test Configuration Discussion

Test Samples

Table C-1 below lists the samples provided by KSC for the purpose of completing the stated test objectives. The table provides sample description and lists which test were performed on each sample.

Table C-1. Test protocol summary.

Test ID	Sample Marking	Description	DS^3 Test	AO Test	UV Test	EC Test
1	C2AAP2	DS^3 unexposed - Spray-on sample	X			
2	21Y-135	DS^3 unexposed - Tile #1	X			X
3	21Y-134	DS^3 unexposed - Tile #2	X			X
4	Wired 1	AO Exposed - Spray-on sample #1		X		
5	C1 AAP2	AO Exposed - Spray-on sample #2		X		
6	C4 AAP2	AO Exposed - Spray-on sample #3		X		
7	Z1Y-122	AO Exposed - Tile #1	X	X		X
8	Z1Y-123	AO Exposed - Tile #2		X		X
9	Z1Y-127	AO Exposed - Tile #3		X		X
10	Wired 2	UV Exposed - Spray-on sample #1			X	
11	C3 AAP2	UV Exposed - Spray-on sample #2			X	
12	Z1Y-130	UV Exposed - Tile #1			X	X
13	Z1Y-131	UV Exposed - Tile #2			X	X

Deep Space Simulator

Overview

The Glenn Research Center Deep Space Solar Simulator (DS^3) is a thermal vacuum chamber designed to simulate a deep space thermal environment, including high-vacuum, a cryogenic-cold thermal background temperature, and an approximate 1-sun solar emission source. Using the DS^3 test chamber, the Solar White samples were tested to assess the material's solar absorptivity and emissivity, using a calorimetric technique. Solar White samples were brought to thermal steady state conditions, under both IR-only conditions (no solar emission) and solar conditions. The

sample and thermal background temperatures and the solar light intensity were measured to assess the sample's performance for cryogenic space applications.

Hardware Description

The DS^3 is shown in Figures C-1 and C-2. The DS^3 consists of a 16" dia. x 14" long cylindrical vacuum chamber. A cryocooler coldhead is installed through the top port of the vacuum chamber and is used to cool the chamber cold shroud assembly. The cold shroud (cube) assembly is mechanically attached to the coldhead, and the entire assembly, except for the view port, is insulated with MLI. The solar simulator is mounted underneath the vacuum chamber and directs its illumination through the vacuum chamber's bottom view port, which is aligned with cold cube assembly viewport. Chamber high vacuum (<10^-6 torr) is achieved via a combination roughing pump and turbo pump vacuum train.

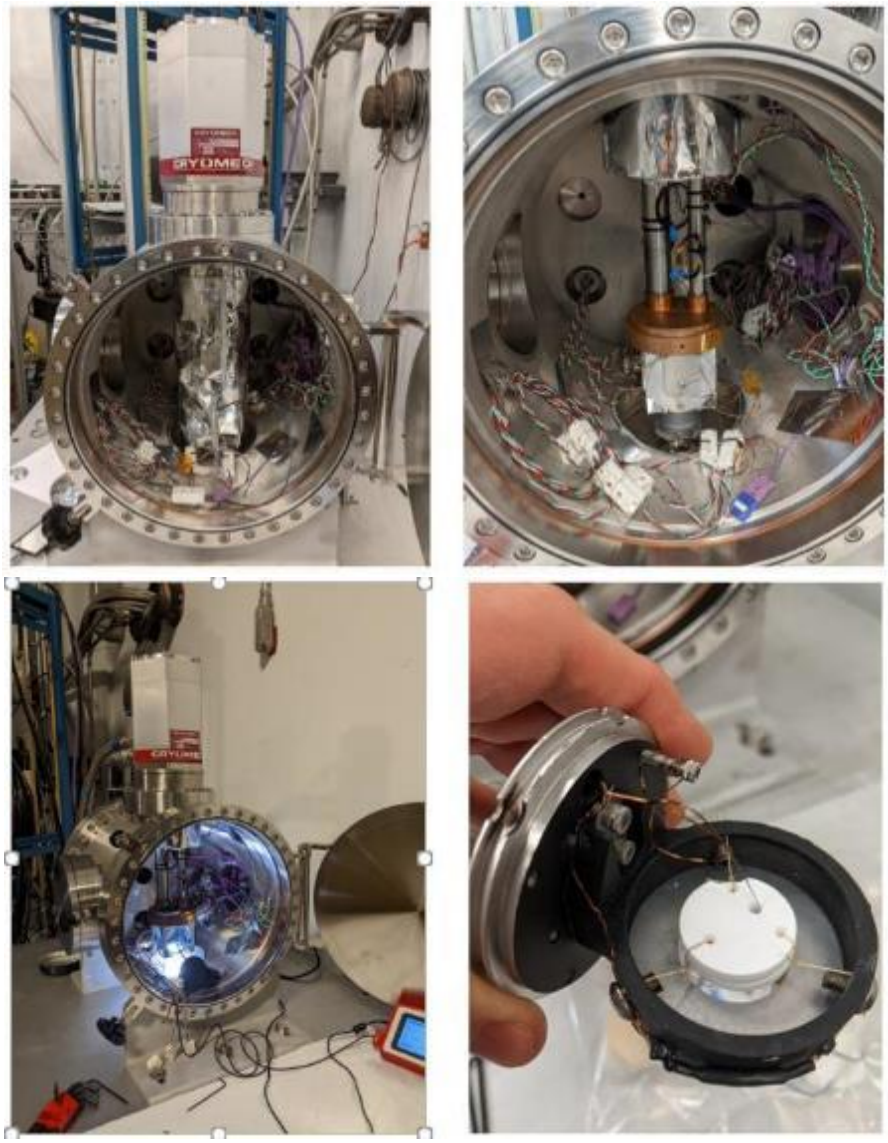

Figure C-1. Deep space solar simulator (DS^3)

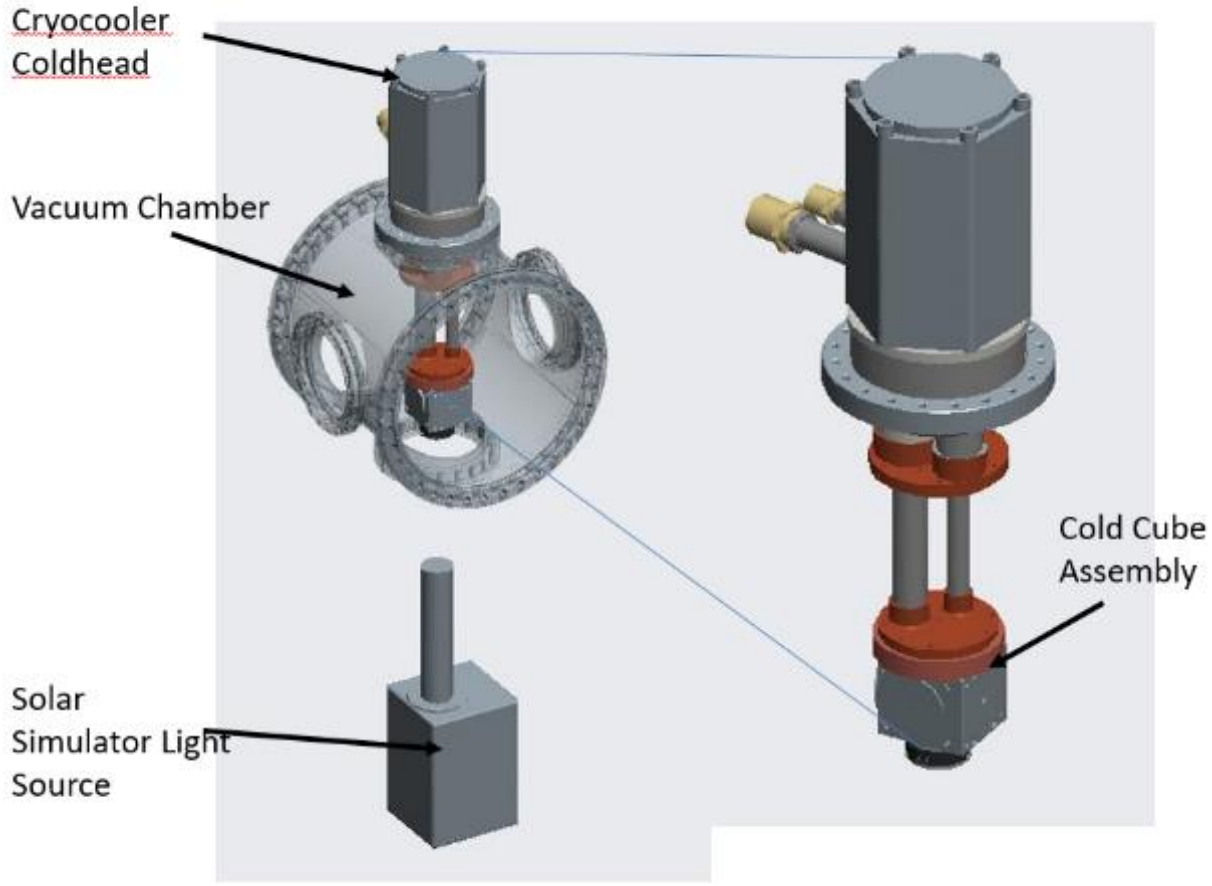

Figure C-2. DS^3 CAD model – base components

Cold Shroud (Cube) Assembly

The cold cube assembly provides the cold, deep space background temperature for samples under test. Attached to the cryocooler coldhead, the cube assembly achieves temperatures as low as 10K without solar illumination and 15-20K while under solar conditions. While the standard reference for deep space cold temperature is 2.7K [1], for the expected steady state sample test temperatures (90 - 150K), 10 - 20K was deemed suitable for the intended application. Additionally, the analysis compensates for the actual boundary conditions under test.

The cold cube assembly (Figure C-3) is constructed from commercial-off-the-shelf (COTS) optical cage-cube components from Thorlabs. The cube itself is part # LC6W and is 60mm in outer dimensions. The sample holder assembly consists of part #'s LB3C and LB5CT2, and the ring diameter is 2 inches. All parts are made of aluminum and were provided free of anodizing. To improve radiative thermal heat transfer, internal cube assembly surfaces were painted with Aeroglaze black paint. The viewport or aperture of the cold cube assembly is 1" in diameter and includes a fused silica glass filter. The glass filter is conductively cooled to the cube assembly, to filter external IR emissions.

The sample is mounted in the sample ring holder via fine Kevlar strings (see Figure C-2). The Kevlar strings minimize conduction between the sample holder and the sample. While mounting

the sample, care is taken to visually center the sample within the sample ring. The sample holder itself is specifically designed to mount and align into the cold cube assembly. The sample holder, when inserted into the cube assembly, accurately aligns the sample relative to the cube view port. Dimensionally, the cold cube assembly can accommodate samples up to 1" in diameter. For instrumentation, the sample holder has two temperature sensors, and the sample itself has an embedded temperature sensor.

The cold cube assembly's viewport and fused silica glass filter is designed to filter in-coming IR radiation from the light source and ambient environment. The fused silica glass absorbs the majority (99.9%) of all external long wave IR radiation (Figure C-4), and the absorbed IR radiation is effectively conducted and absorbed by the cold cube assembly.

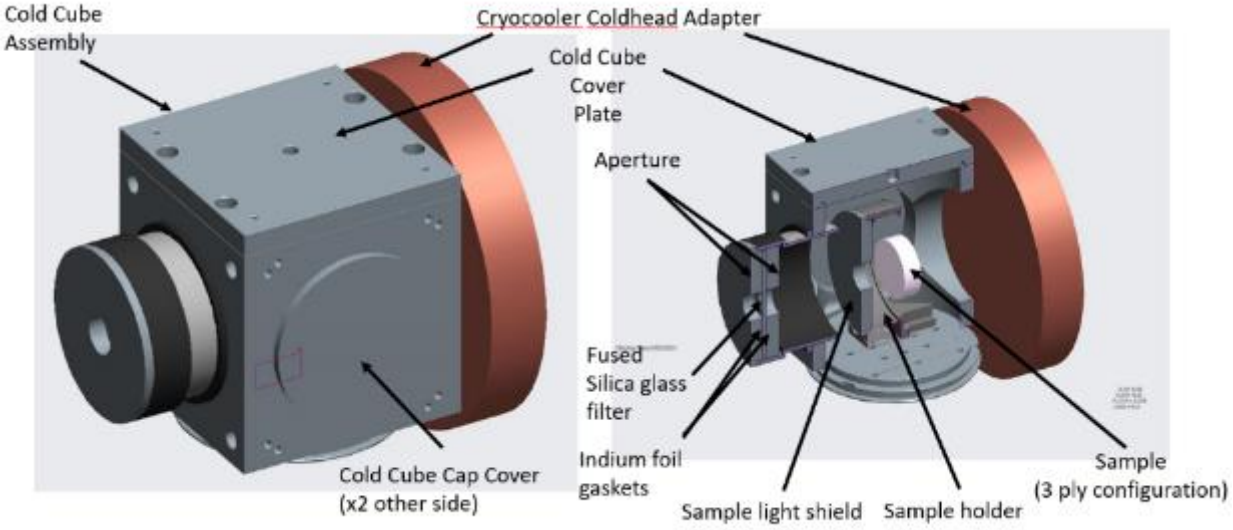

Figure C-3. Cold cube assembly.

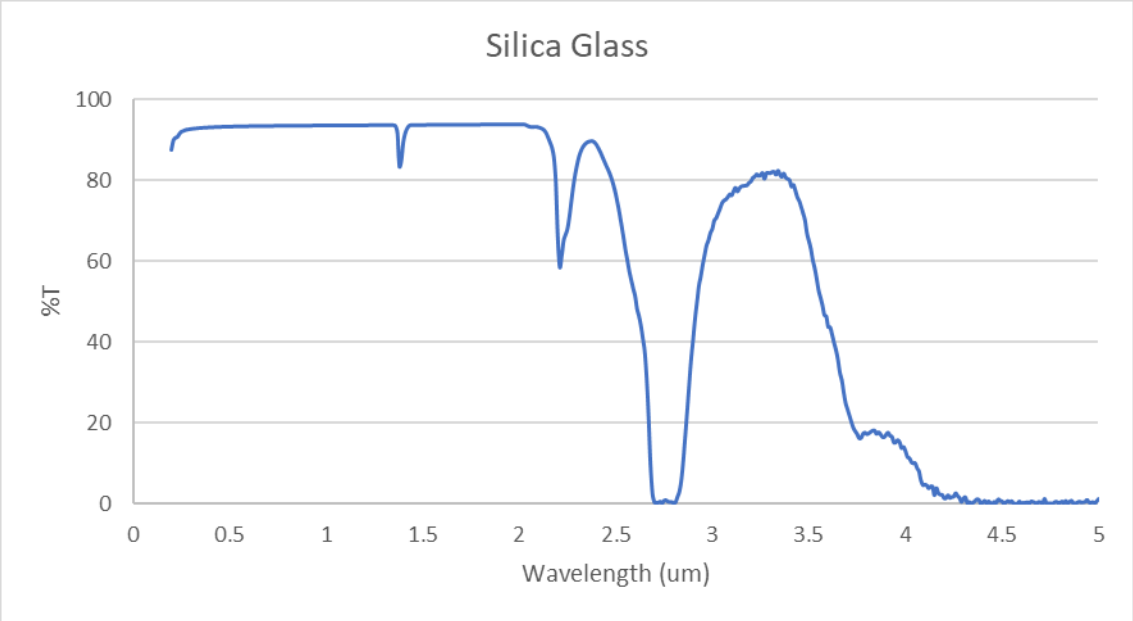

Figure C-4. Fused silica transmissibility data.

Solar Simulator Source

The solar simulator light source is a COTS xenon lamp light source by Newport, model #LCS-100. The spectral irradiance and typical output power is provided in Figure C-5. The light output is commensurate with most commercial xenon-based light sources. As noted in the Overview, the solar simulator light source is mounted underneath the vacuum chamber and the light output is directed into the vacuum chamber viewport, which is aligned with the cold cube assembly viewport.

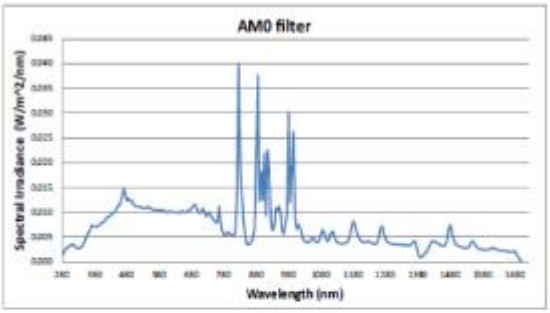

Table 1 Typical Output Power from LCS-100 Solar Simulators

Distance from the Illuminator (inches (mm))	Readings with Optional AM0 Filter (mW/cm²)	Readings with Standard AM 1.5G Filter (mW/cm²)	Readings with Standard AMDir Filter (mW/cm²)
5 (127)	247	161	221
6 (152)	184	119	179
7 (178)	151	100	142
8 (203)	126	82	117
9 (229)	105	69	99

Figure C-5. Newport solar simulator.

Measurements and Instrumentation

Measurements for the DS^3 include cold cube assembly temperatures, sample temperature, and light energy. During testing, temperature measurements were recorded continuously through the cool down phase, during the solar illumination phase, and during the post-test warm up phase. Light energy was measured before and after testing using a handheld light intensity meter and was recorded manually.

The cold cube and sample instrumentation is show in Figures C-6 and Table C-2 below. The cold cube assembly and sample holder are instrumented on all surfaces, to confirm the cold thermal background temperatures. The sample assemblies are shown in Figures C-7 & C-8. To measure sample temperature, a SI-415 barrel-type diode was installed in both the tile sample assembly and the spray-on sample assembly.

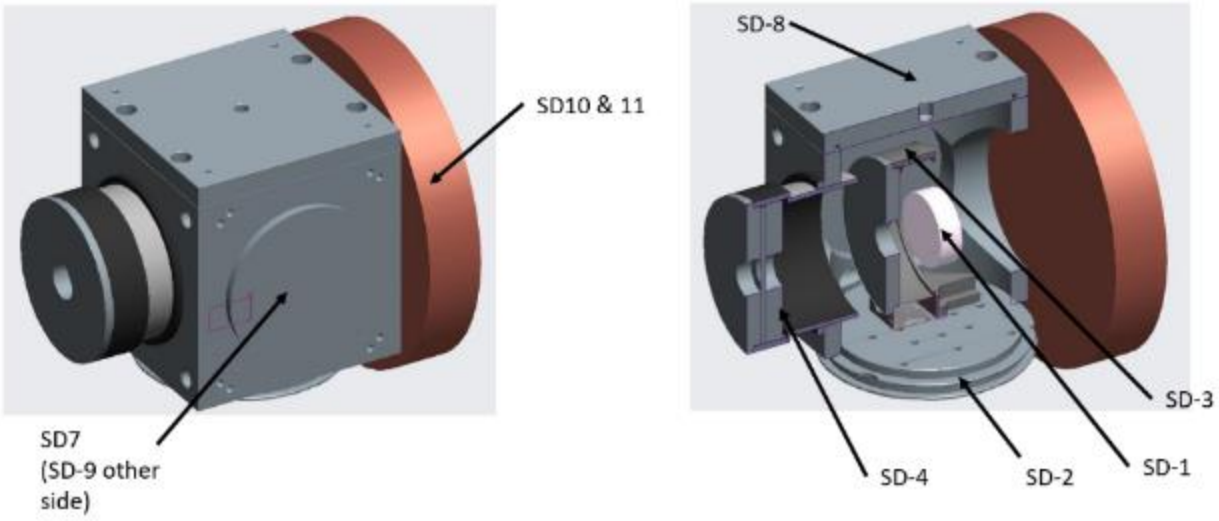

Figure C-6. Cold cube assembly instrumentation.

Table C-2. Cube assembly instrumentation detail.

Channel number	SD #	224 Channel	Location	Diode type
11	1	A	Sample	SI-410 Barrel-type
12	2	B	Front of cube	DT-670 Cu
13	3	C1	Sample holder	DT-670 SD
14	4	C2	Aperture	DT-670 Cu
15	5	C3	Lens 1	Unused
16	6	C4	Lens 2	Unused
21	7	C5	Right side of cube	DT-670 Cu
22	8	D1	Back of cube	DT-670 Cu
23	9	D2	Left side of cube	DT-670 Cu
24	10	D3	Front of adapter	SI-410 Barrel-type
25	11	D4	Back of adapter	SI-410 Barrel-type
26	12	D5	Unused	Unused

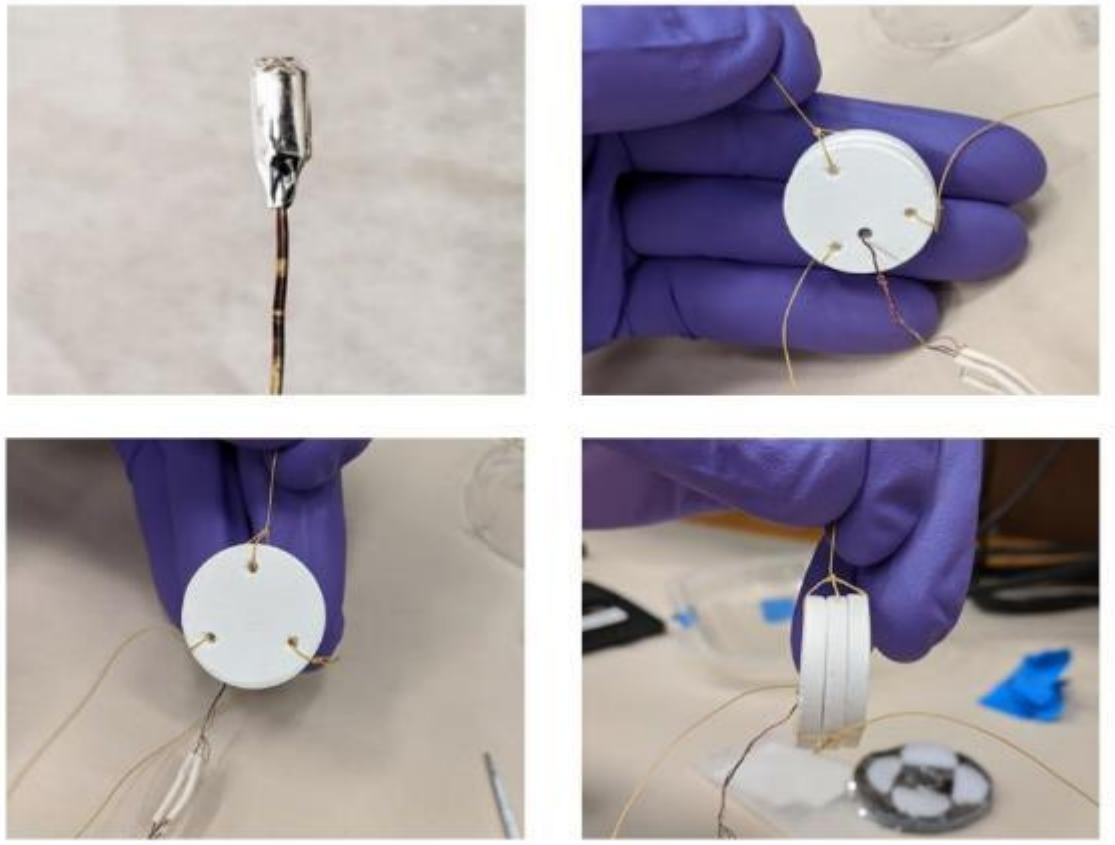

Figure C-7. Solar white tile sample assembly.

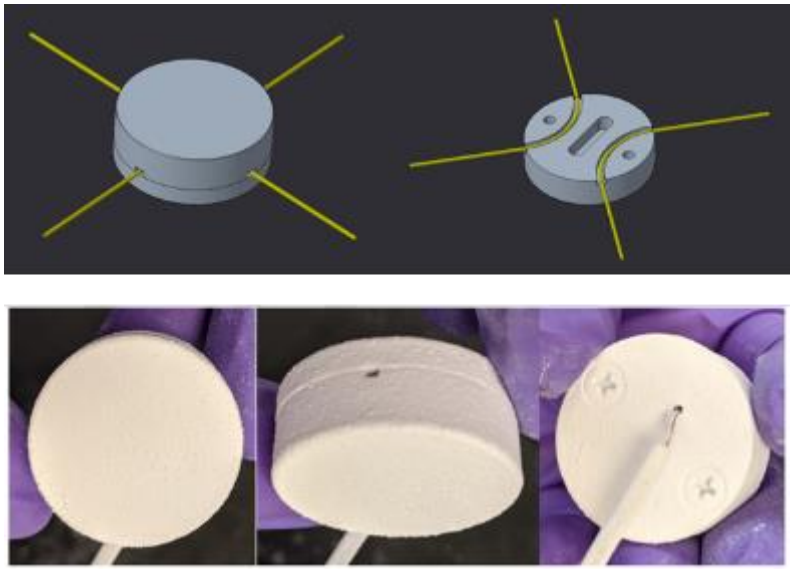

Figure C-8. Solar white spray-on sample assembly.

Light intensity was measured using a COTS thermal power by Thorlabs, model # S405C (See Figure C-9). The S405C sensor is capable of measuring wavelength intensity over a broad

spectrum of wavelengths and is calibrated with NIST-traceable certification of calibration. Performance specifications are listed in the table below. For measuring the light intensity at the sample mount location, a similar optical ring holder was used to mount the light sensor. The light sensor was inserted into the cold cube assembly identical to the Solar White sample holder.

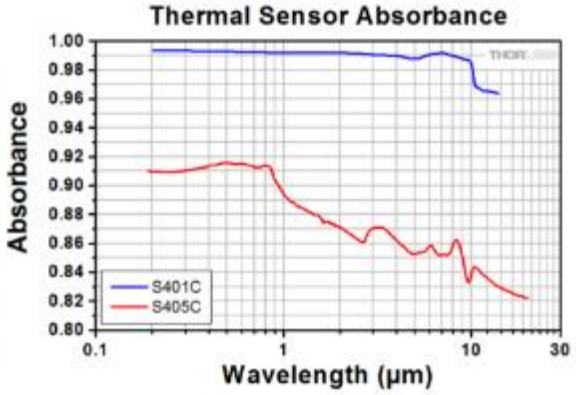

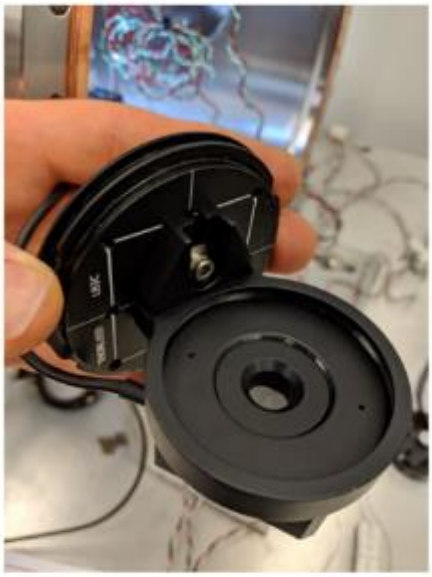

Wavelength Range	190 nm - 20 µm
Optical Power Range	100 µW - 5 W
Input Aperture Size	Ø10 mm
Active Detector Area	10 mm x 10 mm
Max Optical Power Density	1.5 kW/cm² (Avg.)
Detector Type	Thermal Surface Absorber (Thermopile)
Linearity	±0.5%
Resolution[c]	5 µW
Measurement Uncertainty[d]	±3% @ 1064 nm ±5% @ 250 nm - 17 µm
Response Time[e]	1.1 s

Figure C-9. Light intensity meter by Thorlabs.

Testing

DS^3 Testing

A total of 8 Solar White tests were performed in the DS^3, shown in Table C-3 below. Both spray-on and tile Solar White samples were tested. Tiles were tested in both virgin configuration and exposed to atomic oxygen simulated environment. Repeat tests were performed to evaluate alterations of the DS^3 hardware or to evaluate anomalies in previous test results.

Table C-3. DS^3 testing summary.

Test Date	Test ID	Sample ID	Test Description	Comments
12/1/2021	FY21-1	C2AAP2	Spray-on Sample Test #1	DS^3 config: Single lens configuration. **Did not achieve SS conditions.
12/8/2021	FY21-2	21Y-135	Tile sample #1 – Test #1	
12/16/2021	FY21-3	21Y-135	Tile sample #1 – Test #2	DS^3 change: Triple lens configuration.
1/6/2022	FY21-4	C2AAP2	Spray-on Sample Test #2	**Only true flat temp output
1/21/2022	FY21-5	21Y-134	Tile sample #2 – Test #1	
3/4/2022	FY21-6	21Y-134	Tile sample #2 – Test #2	DS^3 change: Added sample holder shield & diode wire thermal anchor
4/1/2022	FY21-7	21Y-122	AO exposed - Test #1	**Abnormal vacuum condition (10^-5 vs 10-7 torr)
4/14/2022	FY21-8	21Y-122	AO-Exposed - Test #2	Vacuum normal: 10^-7 torr

For each test run, DS^3 thermal vacuum testing was performed in 2 phases, light-off steady-state thermal conditions and solar simulation thermal conditions. Key test parameters included: (1) sample radiant background environment temperature, (2) sample temperature, and (03) simulated solar light intensity. The light-off state-state was performed to assess the base IR-thermal baseline conditions prior to initiating the simulated solar condition. The light-off test data provided a key datapoint to validate the thermal model results. During testing, cold cube and sample temperatures are measured continuously. Solar light intensity is measured and recorded manually before and after testing. A breakdown of the standard DS^3 test procedure was as follows:

1. Install sample into holder.
2. Measure and record the light intensity in the cold cube assembly using the light sensor.
3. Install sample into the cold cube assembly.
4. Close chamber and start vacuum pump system.
5. Once high vacuum conditions (10^-5 – 10^-6 torr) were achieved, the cryocooler was turned on.
6. Final light-off thermal steady-state conditions are confirmed (Typical vacuum levels were 10^-7 torr at cold test conditions).
7. Turn solar simulator light source.
8. Final light-on thermal steady-state conditions are confirmed.
9. Turn off light source and cryocooler and warm up DS^3 to ambient conditions.
10. Break vacuum.
11. Perform post-test light intensity light measurement.

Analysis Model Description

Two models were developed to assess the thermal performance of Solar White, a nodal model built in MS Excel and a detailed Thermal Desktop model.

Excel Model

The base thermal analysis to characterize the solar white thermal performance was as follows:

$$E_{IR} + E_{Trans} + E_{diode} + E_{unknown} - (E_{sample} + E_{strings}) = 0$$

A simplified thermal schematic is shown in Figure C-10:

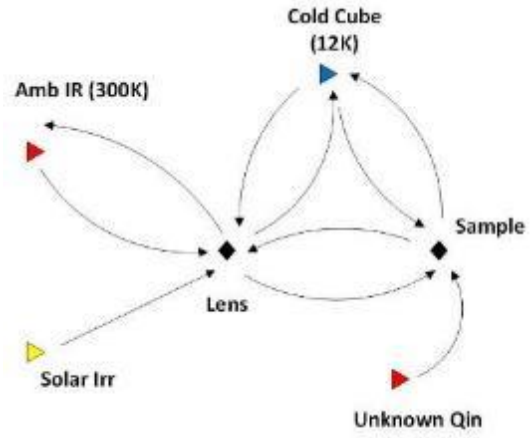

Figure C-10. DS^3 Excel model nodal network description.

E_{IR} includes all thermal background radiation visible to the sample. E_{ir} from the viewport was determined by conducting a test to measure the lens temperature under IR-only cold conditions. Results showed the lens temperature typically cooled to 28K, with a cold boundary temperature of 12K and the external ambient environment at 300K. This result was used to determine the conductance between the aluminum cube assembly and its viewport, which was used to estimate the lens temperature under light-on conditions. E_{Trans} includes all external energy (solar & IR) expected to pass through the cold cube assembly viewport. The manufacturer data and published data for fused silica, were used to estimate the degree of transmission. $E_{strings}$ include the energy conducted through the Kevlar strings used to suspend the sample in the holder. E_{diode} includes energy conducted via the instrument wire and internal diode heating. However, E_{diode} was ultimately excluded from the analysis (due to insufficient data). As such, E_{diode} was effectively rolled up into the $E_{unknown}$ term. E_{sample} includes energy radiated from the sample to the cold thermal background. Finally, $E_{unknown}$ was used in the model to account for heat unaccounted for in the model. The $E_{unknown}$ was determined, in the model, using the final sample temperature under IR-only (light off) conditions.

Thermal Desktop Model

A diagram of the Thermal Desktop model is shown here:

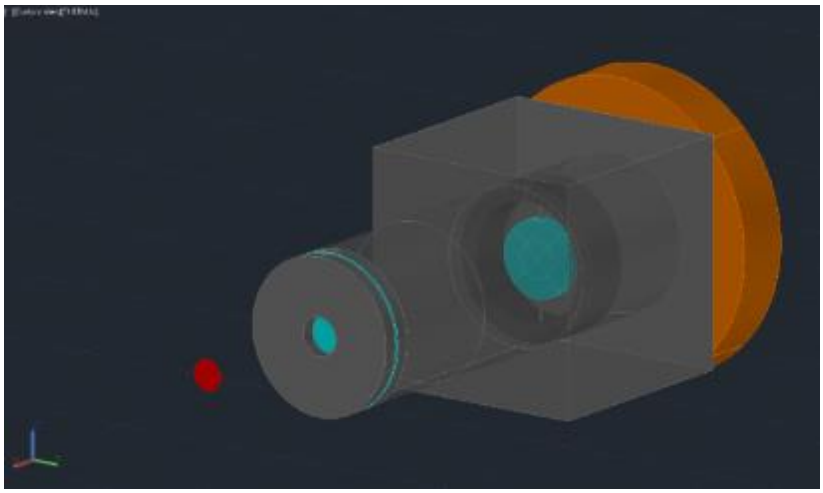

Figure C-11. DS^3 thermal desktop model.

A summary of the model setup is described as follows:

- Solar lamp
  - Single node, thin surface
  - NORMAL optical property on active side
  - Surface not generated (disabled Cond/Cap tab)
- Model runs two cases
  - Light On – 1 Radiation Analysis Group
  - Light Off – 2 Radiation Analysis Groups
- Radiation analysis setup
  - 300,000 rays/node
  - Radk calculation spectrum used for modeling solar lamps
    - Solar vs. infrared
  - Lamp node outputs radks as heating rates (150-170 mW/cm2)
  - Wavelength-dependent properties (0-25 μm)
    - Silica lens & sample

Analysis was conducted to determine estimated sample temperature vs % power absorbed & solar intensity. For all runs, Solar White emissivity was assumed to be 0.85. Solar intensity was varied from 150 – 170 mW/cm^2. Note, solar simulator light intensity average around 155 mW/cm^2 for all test conditions (vs 135 mW/cm^2 1-sun standard[1]). This graph below provides a quick reference for determining material solar absorptivity, given test sample temperature and light intensity measurement.

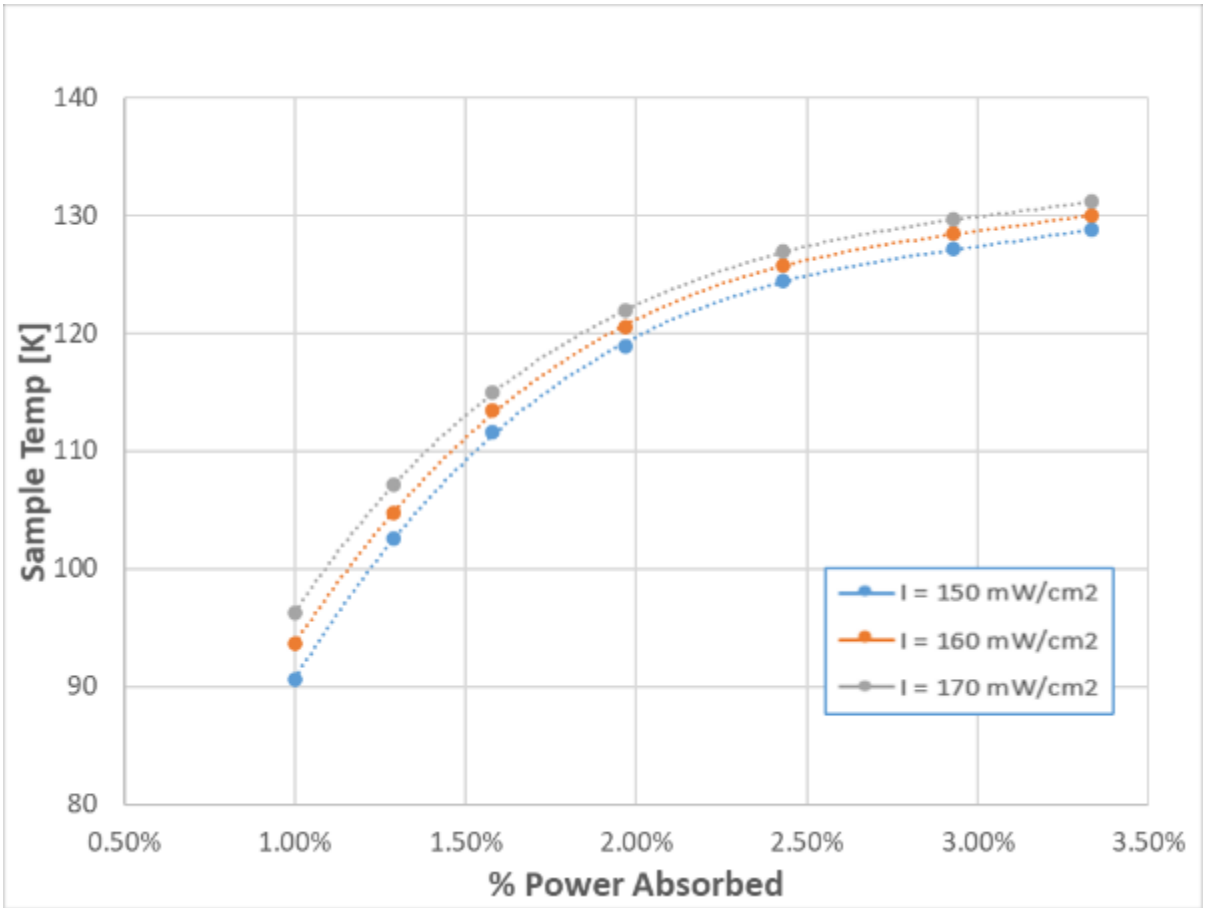

Figure C-12. Thermal desktop model results.

Test Results

A summary of test results is presented in Table C-4 below. The test results were produced using the excel model. Data graphs for each test run are shown in later in this report. Note, runs FY21-1 and FY-7 were not assessed due to testing anomalies. Overall, the solar white solar absorptivity performance was measured at 2.0 – 1.2% for tile and 3.5% for spray-on coating. Post AO-Exposed samples showed negligible performance degradation. Post UV-exposed samples were not tested due to visible UV degradation.

Table C-4. Solar white thermal performance test results.

Test Date	Test ID	Sample ID	Test Description	Final Temp - Light Off	Final Temp - Light On	Qunknown	Qstrings	Heat Abs/ Emitt	Solar Light Input	Solar Abs
				K	K	mW	mW	mW	mW/cm^2	%
12/1/2021	FY21-1	C2AAP2	Spray-on Sample Test #1	68*	174	*	*	*	155	*
12/8/2021	FY21-2	21Y-135	Tile sample #1 – Test #1	64	132 -124	2.35	2.8 - 2.7	23.5 - 18.7	155	2.7-2.1%
12/16/2021	FY21-3	21Y-135	Tile sample #1 – Test #2	56	122 -106	1.69	2.6 - 2.2	17.7 - 10.8	155	2.03 - 1.2%
1/6/2022	FY21-4	C2AAP2	Spray-on Sample Test #2	32	137	0.50	3.90	27.9	155	3.50%
1/21/2022	FY21-5	21Y-134	Tile sample #2 – Test #1	48	119-114	1.20	2.5 - 2.4	16.2 - 13.9	155	1.9 - 1.6%
3/4/2022	FY21-6	21Y-134	Tile sample #2 – Test #2	30	111-105	0.47	2.3 - 2.2	12.7 - 10.5	155	1.55 - 1.3%
4/1/2022	FY21-7	21Y-122	AO exposed - Test #1	18	80-79	*	*	*	155	*
4/14/2022	FY21-8	21Y-122	AO-Exposed - Test #2	17	124-107	0.12	2.6 - 2.2	18.7	155	2.4 - 1.4%

Results Discussion

Throughout the test campaign, the DS^3 design was iterated upon to eliminate hardware heat leaks, which were observed by measuring sample temperature during IR-only (light off) conditions. Several improvements were implemented going into the FY21 campaign, including lens design changes and additional insulation to shield light from entering the cold cube assembly. The initial configuration included a single lens with a 1" diameter viewport (Runs FY21-1 & 2). Observed heat leaks (or $Q_{unknown}$) were as high as 2.35 mW, which amounted to 10% of the estimated heat absorbed by the sample. Starting with run FY21-3, the lens was updated to include three cooled fused silica lenses, to improve viewport IR filtering. An observed drop in sample temperature, both at light-off and light-on conditions was noted. However, $Q_{unknown}$ was still approximately 10% of total sample heat. The final design change was implemented on FY21-6, where a sample shield and instrument wire thermal anchor were added. A comparison of the sample holder configuration is shown in Figure C-13. The test results suggest a significant component of the $Q_{unknown}$ is due to heat leak along the instrument wire and/or ineffective diode conductance with the sample material. One outlier test data point that supports this conclusion is FY21-4, which is the full test of the solar white spray-on sample. The spray-on sample is unique compared to the tile samples because the base sample is made of aluminum and the diode is embedded and epoxied, which provides excellent thermal conductance between the sample and diode. In this test, the sample achieves 30K without the aid of anchoring the instrument wire or additional sample shielding.

Figure C-13. Sample holder configuration comparison: no shield or wire anchor (top) vs. sample shield and wire anchor (bottom).

As noted, the final reported solar absorptivity was calculated using the MS Excel nodal model, which models the DS^3 hardware thermal input sources and factors in design choices, such as the fused silica viewport and the sample support strings. Thermal radiation, in the model, is input as a wavelength-dependent input (mW/cm^2/nm). Background thermal radiation was calculated using the monochromatic emissive power equation for a black body [2]. The solar simulator energy input was based on the manufacturer light output data, and the total light source input energy was also scaled to match the total simulated solar energy level, which was measured using the light intensity meter.

Analysis was performed in two steps. First, the light-off or IR-only test results were input into the model. 300k external thermal environment was assumed. The results for the cold cube lens temperature were input as the boundary temperature for the lens thermal node. This temperature was used to estimate the thermal conductance between the lens and aluminum assembly. Next, the final no-light sample temperature was input into the model. The sample thermal node was converged to zero using $Q_{unknown}$ as the input variable. The next step in modeling was to turn on the light source in the model. With the light turned in the model, the lens temperature was recalculated, converging its node to zero energy balance again by calculating the lens temperature with the light on. Lastly, the sample temperature was input into the model and the sample thermal node was converged to zero energy balance by driving the sample solar absorptivity. Note, sample emissivity was assumed to be 0.85. The final sample solar absorptivity was calculated and is reported in Table C-4.

Sample solar absorptivity is reported as a range for all but one of the test runs (FY21-4). Most test results exhibited a non-steady final solar simulated test condition (see data graphs in DS^3 Test Data section). This peaking in temperature and gradual decay is currently unexplained. The range of solar absorptivity is based on the maximum and minimum recorded sample temperatures.

The non-steady final sample temperature was a new phenomenon with the FY21 testing, as previous years did not exhibit this behavior. It is believed one of the FY21 DS^3 design changes is driving this conduct. Possible causes are believed to be localized heating of the DS^3 insulation, which then gradually cools over time, or perhaps insufficient vacuum levels inside the cube assembly, since significant effort was spent "tightening" up the cube assembly from intrusive light.

Lessons Learned

The Spacecraft Thermal Control Coatings Reference, NASA/TP-2005-212792 [3], describes a Calorimetric Technique for Determining Hemispherical Emittance (section 3.2.3 of the referenced report). Several key design factors were noted that could equally apply to improving the DS^3.

It's noted that parasitic heat losses can affect the accuracy of the measurement at cryogenic temperatures and therefore must be minimized or eliminated from the test and taken into account during the calculation. The parasitic heat losses/inputs primarily arise from the heat lost due to the (1) residual gas in the vacuum chamber, (2) heat conducted through and emitted from the temperature sensor leads, (3) heat from the sample being reflected back to the sample from the chamber walls, (4) radiant heat from the outside striking the sample, or (5) heat dissipated by the temperature sensor into the sample substrate.

- Regarding heat from the sample being reflected back to the sample, it is noted that, if the total area of the sample is small with respect to the total area of the chamber, the heat emitted from the sample and subsequently reflected from the chamber wall back to the sample can be neglected. This could be an area of improvement for the DS^3.

- Sensor heat amounts to a few microwatts and represents only a minor correction factor.

- It is recommended that the vacuum chamber pressure must also be kept as low as possible to minimize the conduction of heat from the sample to the shroud wall by residual gasses in the chamber. For a lower temperature range of -150°C a pressure of 1x10^-6 torr is considered adequate, for lower temperature range an even lower pressure should be maintained to less than 4x10^-8 torr. Note, DS^3 typically operated at 10^-7 torr.

- The loss due to heat flowing down the temperature sensor leads and the heat wires and heater sensors can for the most part be eliminated by the use of a guard heater. All sample instrument wires must be thermally tied to the guard heater, which is operated at the same temperature as the sample. This effectively eliminates heat flow from the sample to the shroud wall via the heater and thermocouple wires. This should be considered for future iterations of DS^3.

- Lastly, a low emittance coating should be applied to the wire insulation between the sample and the guard heater to minimize the heat radiated to the shroud wall by the wire insulation.

Conclusion

A total of 8 test runs were completed in the FY21 timeframe. During the test sequences, several DS^3 design iterations were evaluated to improve test results. Several issues remain that impede the overall DS^3 system performance, including diode contact with sample, insufficient isolation of sample instrument wire, and an uncharacterized thermal transient during solar illumination conditions.

The solar white tile and spray-on material thermal performance were characterized with results showing a 1-2% solar absorptivity for tile and 3.5% for spray-on coating. The final temperature of the tiles ranged from 105-120K and the spray-on sample achieved 137K. Samples exposed to Atomic Oxygen showed minimal thermal performance impact, when compared to unexposed samples.

To characterize the performance of Solar White, two thermal models were developed. The models were used to both improve the design of the DS^3 and characterize the Solar White material thermal performance from test data.

References

1. Donabedian, Martin. (2003). *Spacecraft Thermal Control Handbook Volume II: Cryogenics.* The Aerospace Corporation.
2. Barron, Randall. & Nellis, Gregory. (2016). *Cryogenic Heat Transfer 2nd Edition.* CRC Press.
3. Kauder, Lonny. (2005). "Spacecraft Thermal Control Coatings References", NASA/TP-2005-21279

DS^3 Test Data

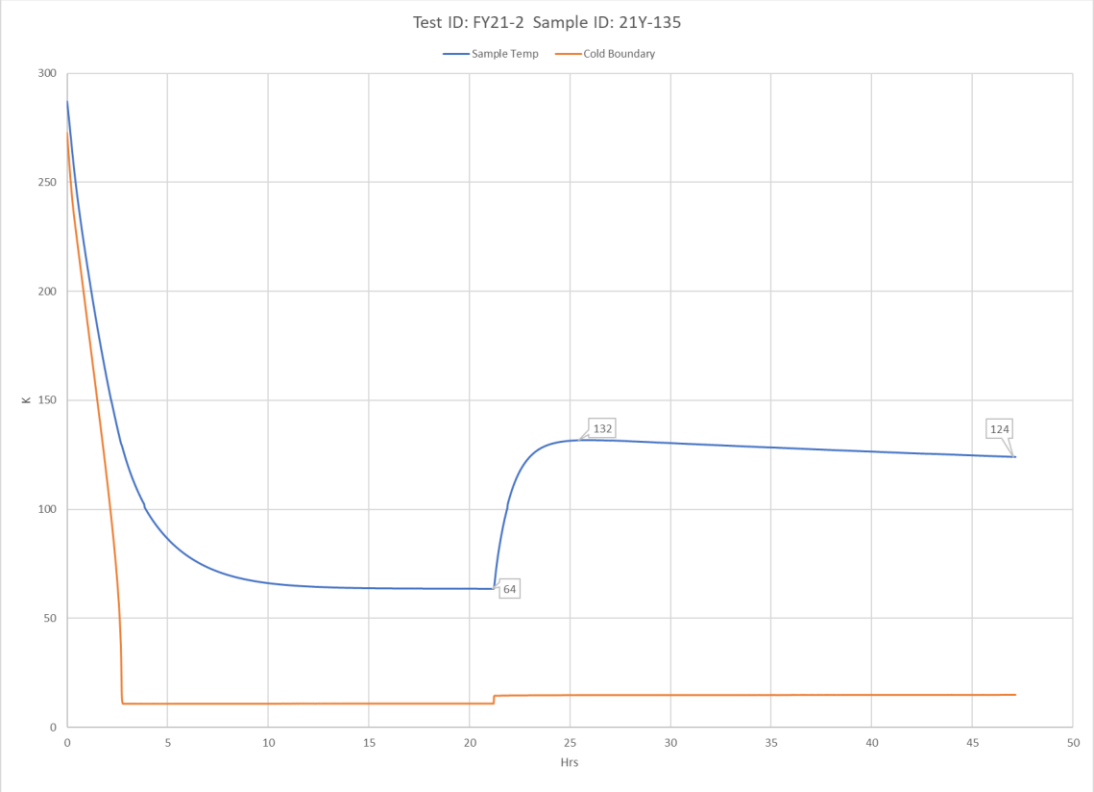

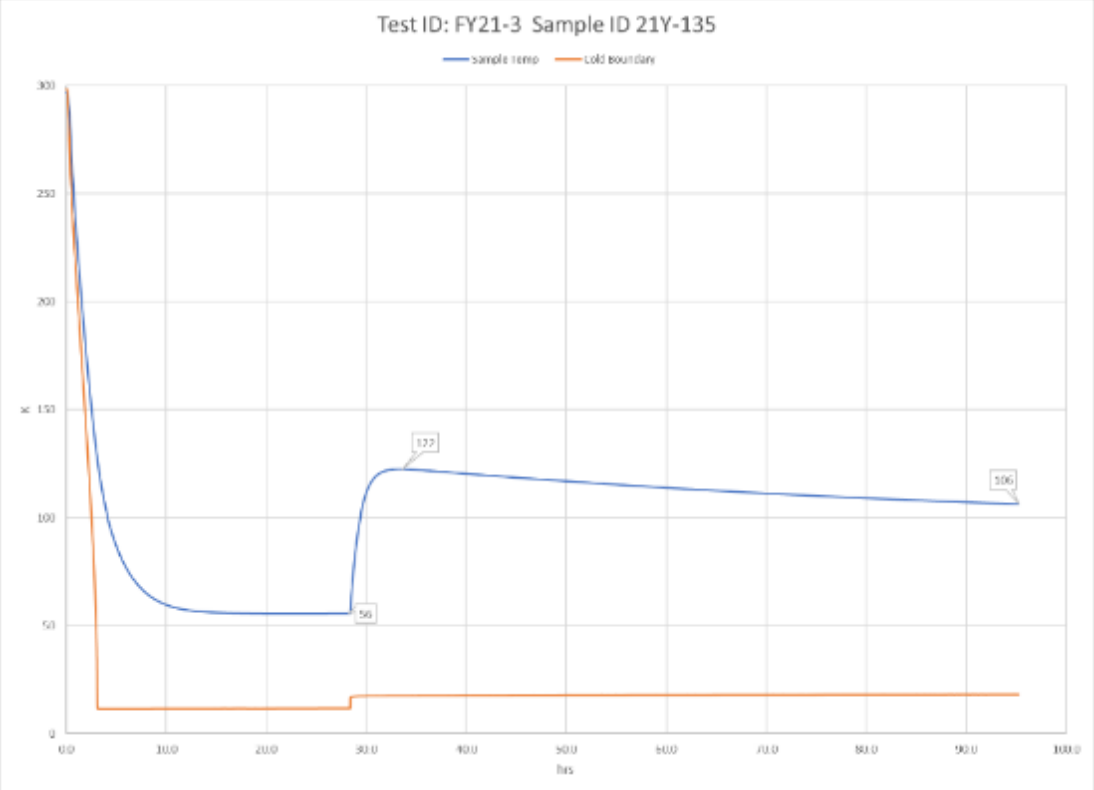

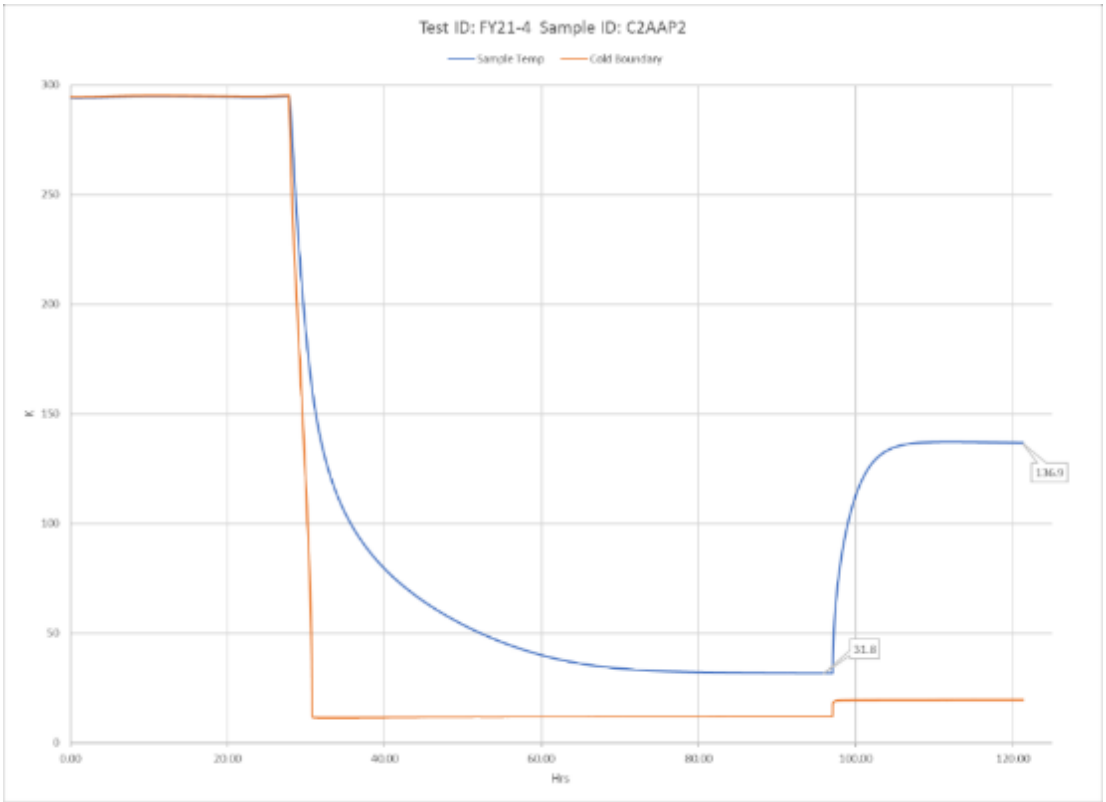
Test ID: FY21-4 Sample ID: C2AAP2
Sample Temp
Cold Boundary
K
Hrs
136.9
31.8

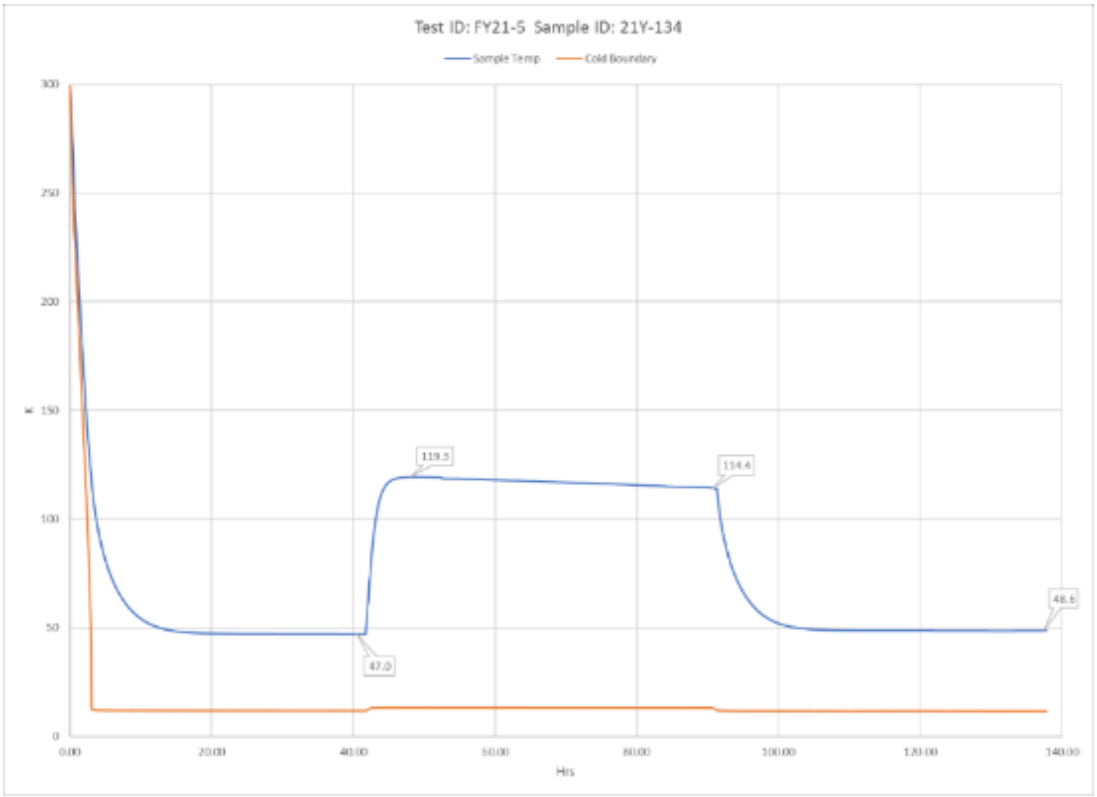
Test ID: FY21-5 Sample ID: 21Y-134
Sample Temp
Cold Boundary
K
Hrs
119.5
114.4
47.0
48.6

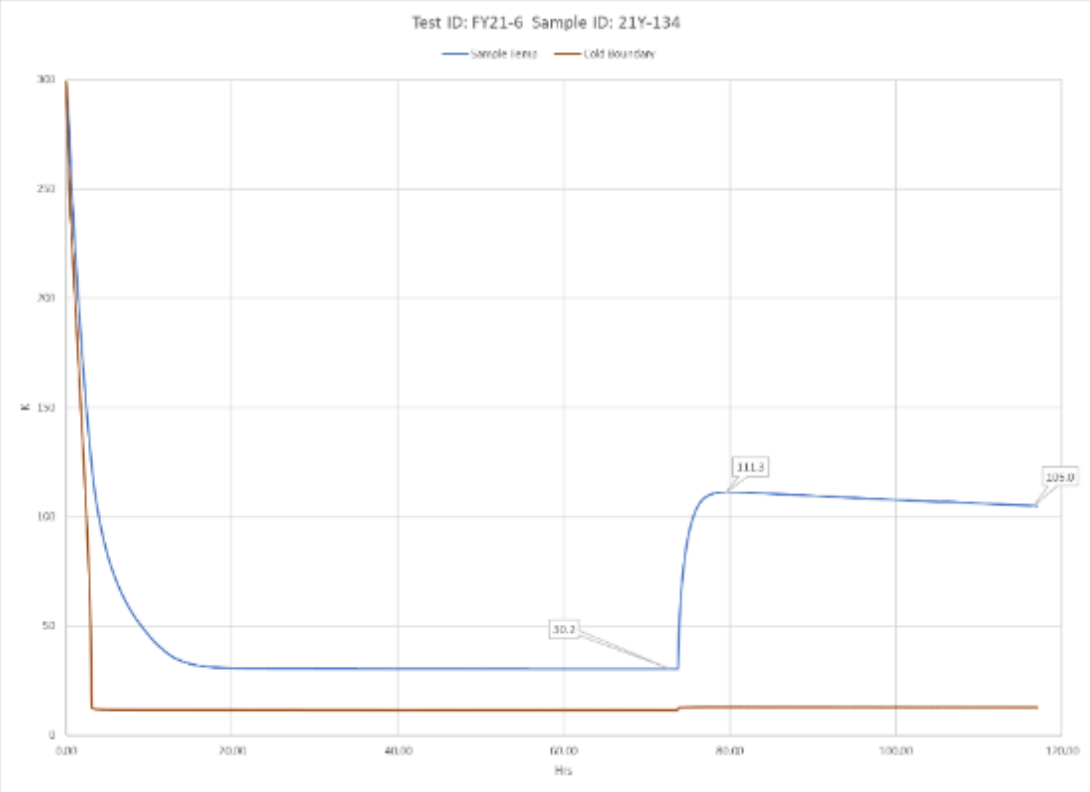
Test ID: FY21-6 Sample ID: 21Y-134
Sample Temp
Cold Boundary
K
Hrs
111.3
105.0
30.2

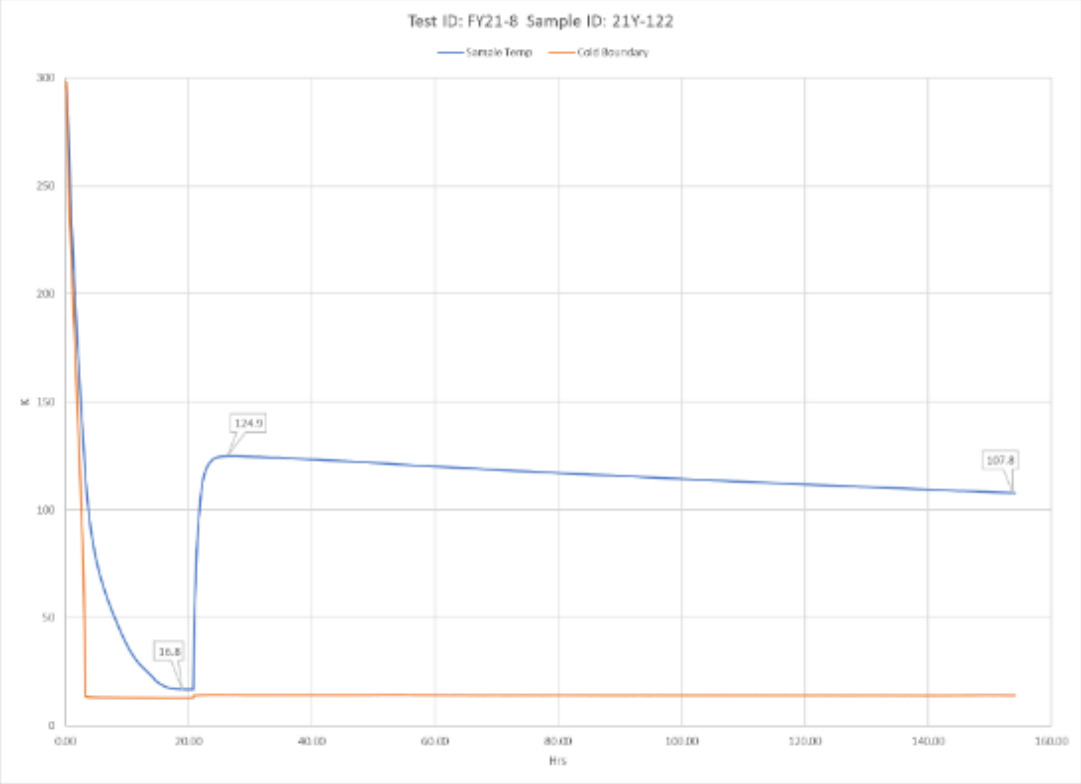
Test ID: FY21-8 Sample ID: 21Y-122
Sample Temp
Cold Boundary
K
Hrs
124.9
107.8
16.8

APPENDIX D: ATOMIC OXYGEN EXPOSURE OF SOLAR WHITE COUPONS

Sharon Miller
NASA Glenn Research Center, Cleveland OH

Emily Naim
HX5 at NASA Glenn Research Center, Cleveland OH

Introduction

This report summarizes the results of testing completed under the STMD GCD Cryogenic Fluid Transfer project to measure the effect of atomic oxygen on the solar absorptance and thermal emittance of tiles composed of Solar White and Solar White sprayed onto aluminum substrates. The atomic oxygen dose levels were provided by the project to represent levels that the solar white thermal control surface may be exposed to on a cryogenic refueling platform. There is concern that exposure to atomic oxygen may affect the ability of the thermal control surface to absorb and reject heat thereby reducing the effectiveness of the thermal control surface. The Solar White coupons were exposed to three atomic oxygen dose or fluence levels and the solar absorptance and thermal emittance were measured on each coupon as received and after each exposure increment.

Test Description

Atomic oxygen exposure testing was conducted in a small quartz vacuum chamber evacuated using a roughing pump with a filtered inlet to prevent pump fluid back-streaming. The chamber was backfilled with a constant flow of filtered air at a flow rate of 3.3 standard cubic centimeters per minute during testing to reach a rough vacuum of approximately 270-300 mTorr. Capacitor plates on the outside of the chamber were powered to 50 W of forward radio frequency (RF) power to create a plasma discharge in the chamber to produce atomic oxygen. Similar results have been shown to be obtained whether an air or oxygen plasma is used.1 An aluminum sample mounting plate shown in Figure D-1 was machined to fit the 2.54 cm diameter Solar White coupons that were provided. The holder was machined to various depths to accommodate the difference in thickness between the sample coupons that were Solar White tiles and those that were Solar White spray coated onto aluminum substrates so that the surfaces were all level with the top of the sample plate. The Solar White tiles had three small holes spaced around the perimeter of the samples. Therefore, a 2.54 cm diameter, 0.00079 thick sample of polyimide Kapton H was placed under each sample to reduce atomic oxygen flux through the tile sample from the back side. A 2.54 cm diameter, 0.0127 cm thick sample of polyimide Kapton H, used to measure the atomic oxygen fluence, was also placed on top of an aluminum spacer in the sample holder. The Kapton H sample was dehydrated under vacuum for 48 hours prior to weighing on a Sartorius ME-5 microbalance both before and after atomic oxygen exposure.

The change in mass of the polyimide Kapton H was used to calculate the atomic oxygen fluence for each increment as described in ASTM E-20892. Three Solar White tile samples and three spray coated Solar White on aluminum samples (one with thermocouple wires embedded in the back), were exposed to atomic oxygen. The wires were wrapped with aluminum foil to protect the wires and insulation from erosion by atomic oxygen during exposure. Figure D-2 shows the Solar White samples in the holder in the chamber after RF power was applied to initiate the plasma.

Figure D-1. Solar White samples in aluminum sample holder with Kapton fluence witness.

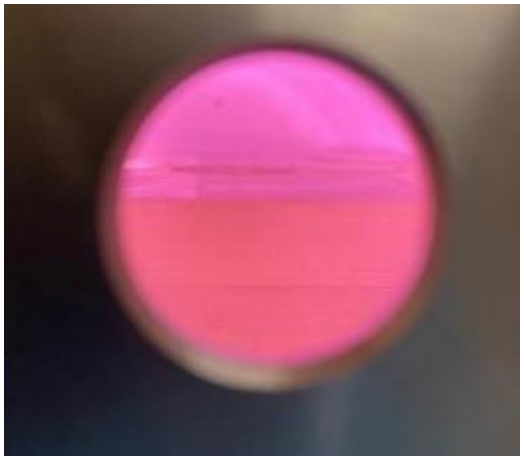

Figure D-2. Solar White samples in atomic oxygen chamber.

Before and after each atomic oxygen exposure increment, the reflectance of the surface in the ultraviolet-visible-near infra-red was measured as a function of wavelength from 250 to 2500 nm using a Cary 5000 spectrophotometer with a DRA-2500 integrating sphere. This was used to calculate the absorptivity (absorptivity =1-reflectivity). The reflectance in the IR wavelength ranges as a function of wavelength was measured in the same manner using a Nicolet FTIR with Pike integrating sphere attachment. This was used to calculate the emissivity (emissivity=1-IR reflectivity). The total thermal emittance was calculated by integrating the emissivity as a function of wavelength with respect to the black body curve at each temperature of interest[3], and the solar absorptance was calculated by integrating the solar absorptivity with respect to the Air Mass Zero (AM0) solar spectrum[4].

Results and Discussion

Solar White tile samples 21Y-122, 21Y-123, 21Y-127, and Solar White spray coating on aluminum samples C1AAP2, C4AAP2 and wired sample #1 were exposed to three increments of atomic oxygen exposure up to a total fluence of 1.31e21 atoms/cm^2. Figure D-3 contains a photo of the Solar White samples in the holder after atomic oxygen exposure. After exposure, the initially bright white samples appeared to be more of an ivory color, hence indicating a slight discoloration.

Figure D-3. Solar White coupons in sample holder after atomic oxygen exposure to a fluence of 1.31e21 atoms/cm^2.

The reflectance as a function of wavelength data showed that the Solar White was becoming less reflecting in the blue portion of the spectrum, confirming the visual observation of a slight discoloration of the samples. Figures D-4 through D-6 contain the reflectivity as a function of atomic oxygen fluence for each of the Solar White samples (the original report contains plots of absorptivity (1-reflectivity), but these have been removed to try and keep the final report manageable).

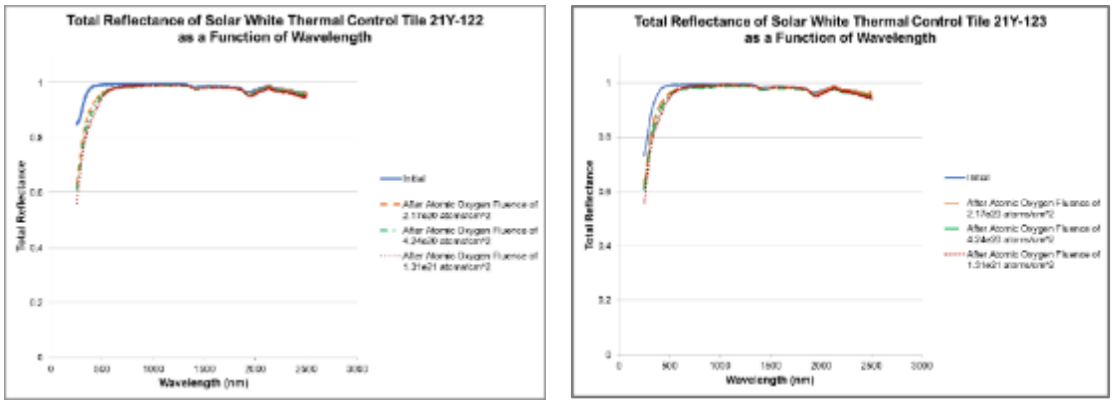

Figure D-4. Reflectivity of Solar White thermal control tiles 21Y-122 and 21Y-123 with atomic oxygen fluence.

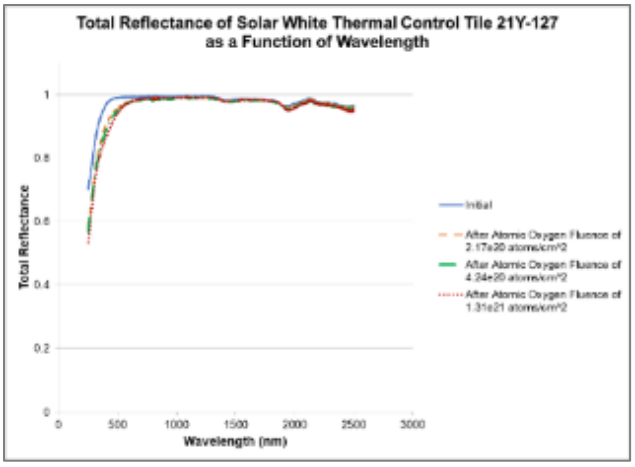

Figure D-5. Reflectivity of Solar White thermal control tile 21Y-127 with atomic oxygen fluence.

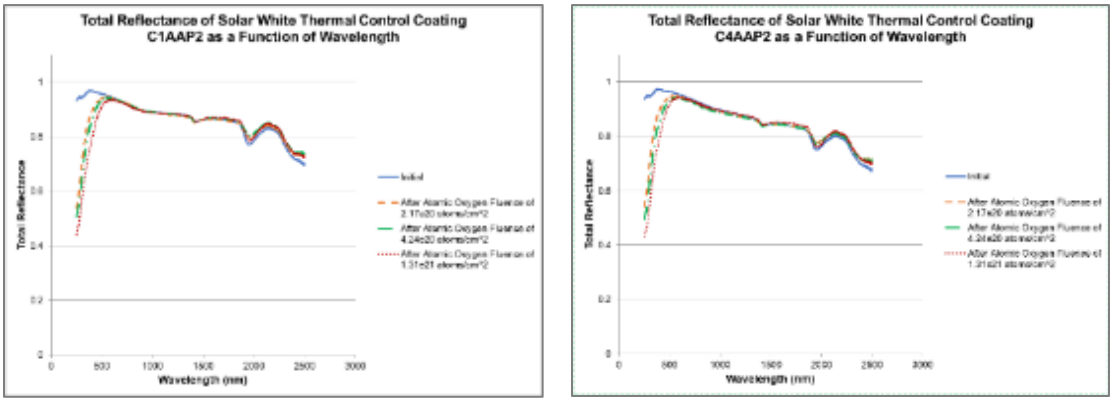

Figure D-6. Reflectivity of Solar White spray coating on aluminum with atomic oxygen fluence.

For both the Solar White tiles and Solar White spray coating on aluminum samples, the greatest change occurred early in the exposure with less noticeable changes after the first exposure increment. Table D-1 contains the air mass zero (AM0) solar absorptance values as a function of atomic oxygen fluence for each of the Solar White samples. The greatest percentage change in AM0 solar absorptance with atomic oxygen exposure occurred for the Solar White tile samples. Overall, the tile samples exhibited a 161-276% increase in AM0 solar absorptance while the spray coating on aluminum samples increased 51-54%. The tile samples however still had an AM0 solar absorptance lower than the spray coating on aluminum samples.

Table D-1. Air Mass Zero (AM0) solar absorptance as a function of atomic oxygen fluence for Solar White tile and Solar White spray coating on aluminum samples.

Sample	Initial AM0 Solar Absorptance	AMO Solar Absorptance after Atomic Oxygen Fluence of 2.17e20 atoms/cm^2	Change in Solar Absorptance	Percent Change
21Y-122	0.012	0.033	0.021	178.97
21Y-123	0.016	0.034	0.018	108.99
21Y-127	0.018	0.039	0.021	116.23
C1AAP2	0.084	0.104	0.021	24.54
C4AAP2	0.081	0.104	0.023	28.87
Sample	AMO Solar Absorptance after Atomic Oxygen Fluence of 2.17e20 atoms/cm^2	AMO Solar Absorptance after Atomic Oxygen Fluence of 4.24e20 atoms/cm^2	Change in Solar Absorptance	Percent Change
21Y-122	0.033	0.039	0.006	17.97
21Y-123	0.034	0.042	0.008	22.81
21Y-127	0.039	0.043	0.005	12.45
C1AAP2	0.104	0.110	0.006	6.01
C4AAP2	0.104	0.116	0.012	11.45
Sample	AMO Solar Absorptance after Atomic Oxygen Fluence of 4.24e20 atoms/cm^2	AMO Solar Absorptance after Atomic Oxygen Fluence of 1.31e21 atoms/cm^2	Change in Solar Absorptance	Percent Change
21Y-122	0.039	0.045	0.006	14.18
21Y-123	0.042	0.044	0.002	5.54
21Y-127	0.043	0.047	0.003	7.40
C1AAP2	0.110	0.126	0.016	14.56
C4AAP2	0.116	0.124	0.008	7.15
Sample	Initial AM0 Solar Absorptance	AMO Solar Absorptance after Atomic Oxygen Fluence of 1.31e21 atoms/cm^2	Change in Solar Absorptance	Percent Change
21Y-122	0.012	0.045	0.033	275.77
21Y-123	0.016	0.044	0.028	170.88
21Y-127	0.018	0.047	0.029	161.16
C1AAP2	0.084	0.126	0.043	51.25
C4AAP2	0.081	0.124	0.044	53.89

Figure D-7 contains a graph of the AM0 solar absorptance of the Solar White samples as a function of atomic oxygen fluence. As can be seen from the graph, the AM0 solar absorptance for both the tile and spray coating on aluminum samples increased and leveled off as a function of fluence at about the same rate.

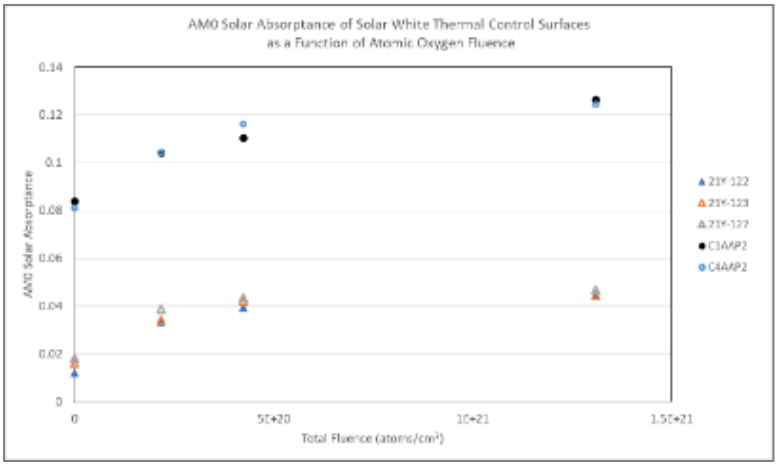

Figure D-7. AM0 Solar Absorptance of Solar White tile and Solar White spray coating on aluminum samples as a function of atomic oxygen fluence.

Figures D-8 through D-17 contain graphs of emissivity and total thermal emittance vs temperature for each of the Solar White samples with atomic oxygen exposure. Figure D-18 contains a graph of the emittance at 90K as a function of atomic oxygen fluence.

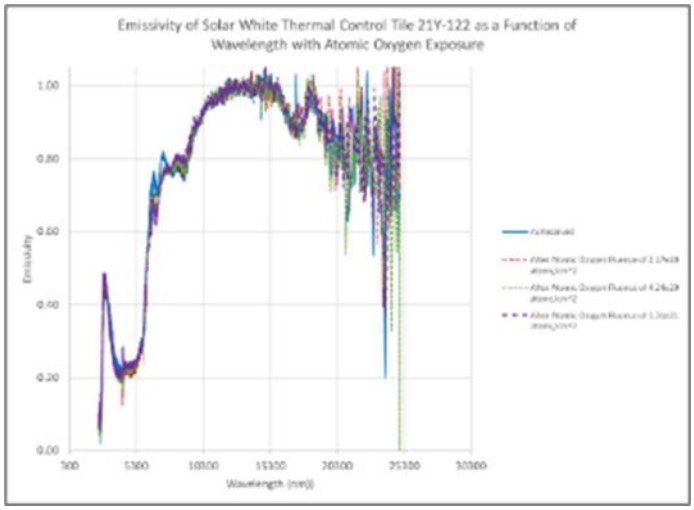

Figure D-8. Emissivity of Solar White tile sample 21Y-122 as a function of atomic oxygen fluence.

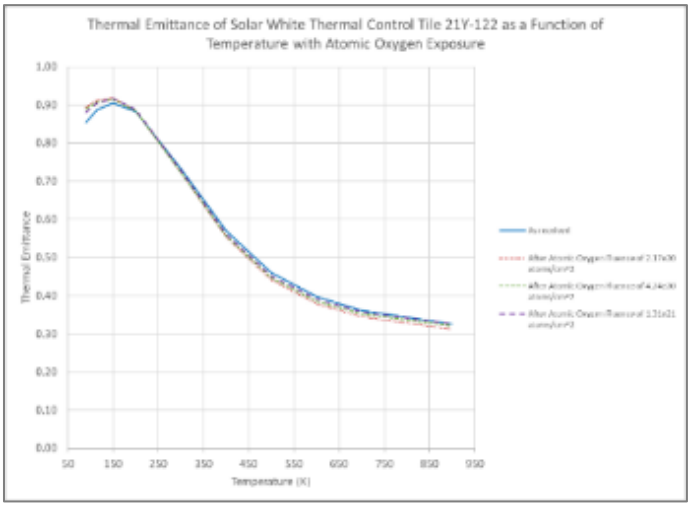

Figure D-9. Thermal emittance as a function of temperature and atomic oxygen fluence for Solar White tile sample 21Y-122.

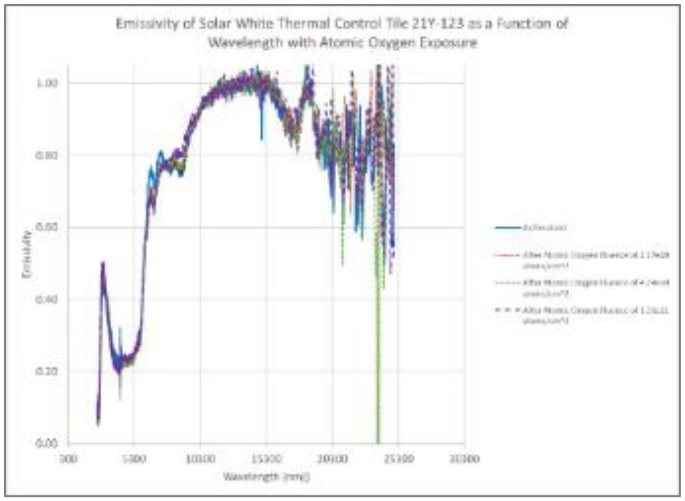

Figure D-10. Emissivity of Solar White tile sample 21Y-123 as a function of atomic oxygen fluence.

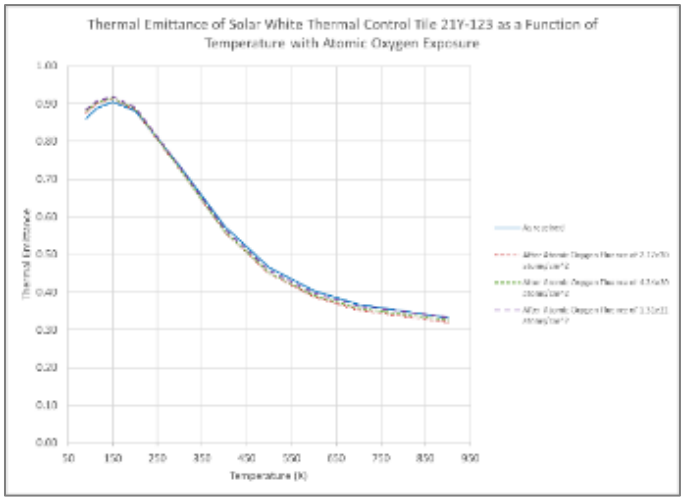

Figure D-11. Thermal emittance as a function of temperature and atomic oxygen fluence for Solar White tile sample 21Y-123.

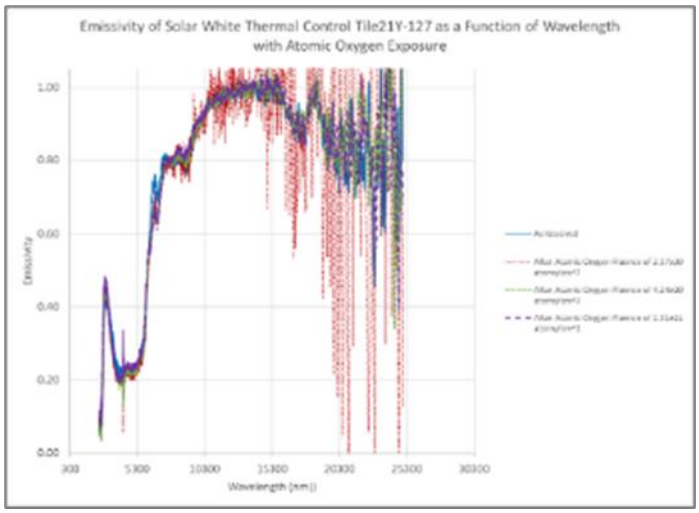

Figure D-12. Emissivity as a function of atomic oxygen fluence for Solar White tile sample 21Y-127.

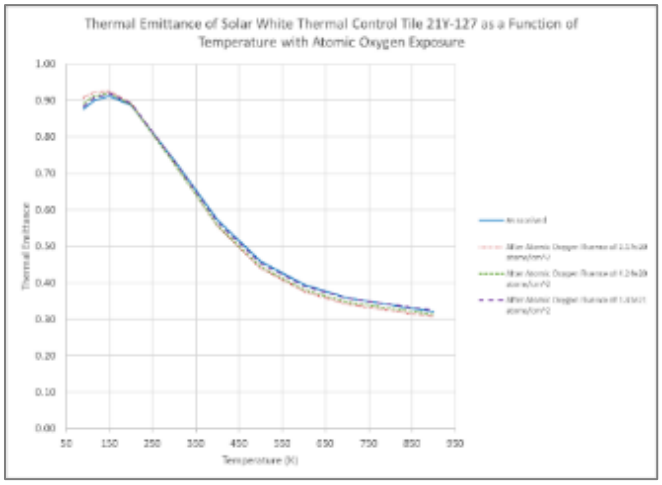

Figure D-13. Thermal emittance as a function of temperature and atomic oxygen fluence for Solar White tile sample 21Y-127.

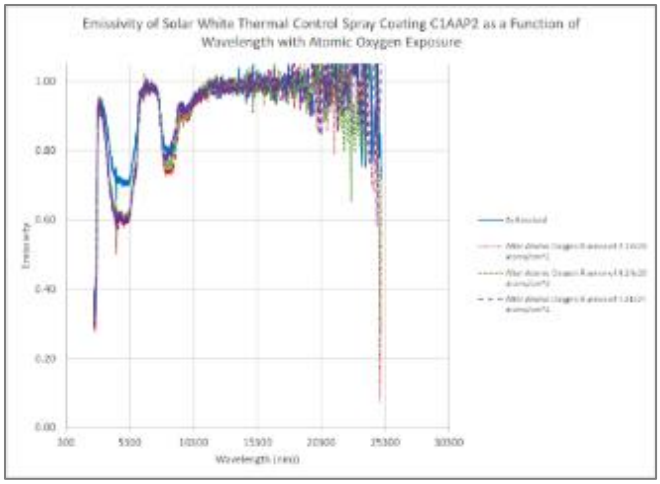

Figure D-14. Emissivity as a function of atomic oxygen fluence for Solar White spray coating on aluminum sample C1AAP2.

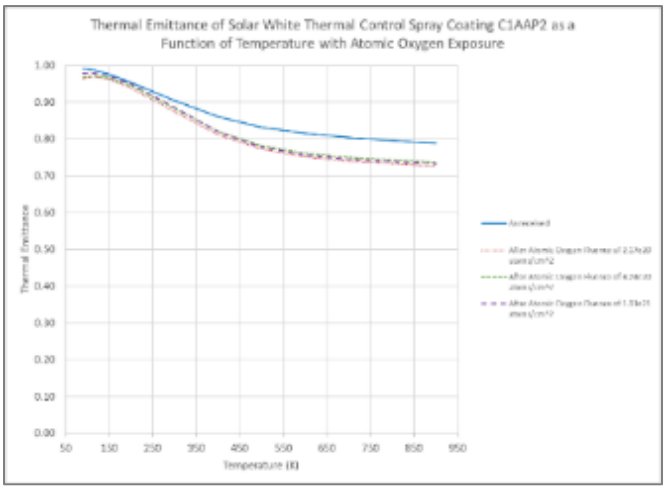

Figure D-15. Thermal emittance as a function of temperature and atomic oxygen fluence for Solar White spray coating on aluminum sample C1AAP2.

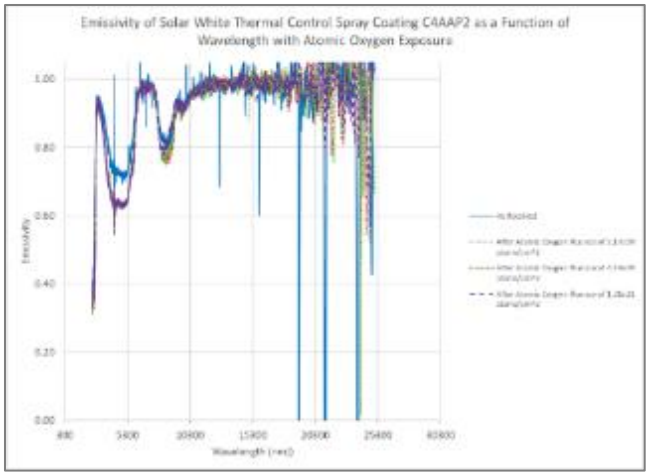

Figure D-16. Emissivity as a function of atomic oxygen fluence for Solar White spray coating on aluminum sample C4AAP2.

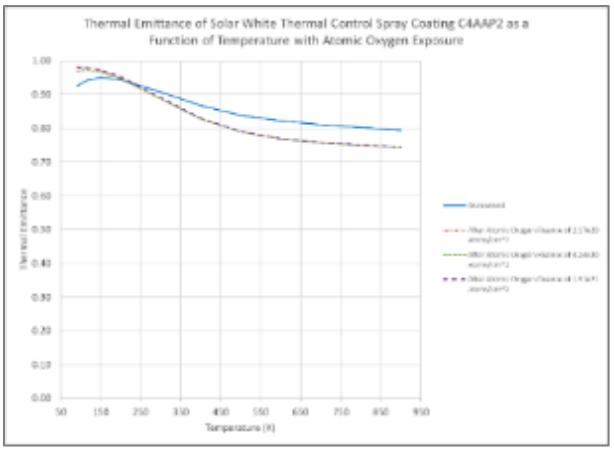

Figure D-17. Thermal emittance as a function of temperature and atomic oxygen fluence for Solar White spray coating on aluminum sample C4AAP2.

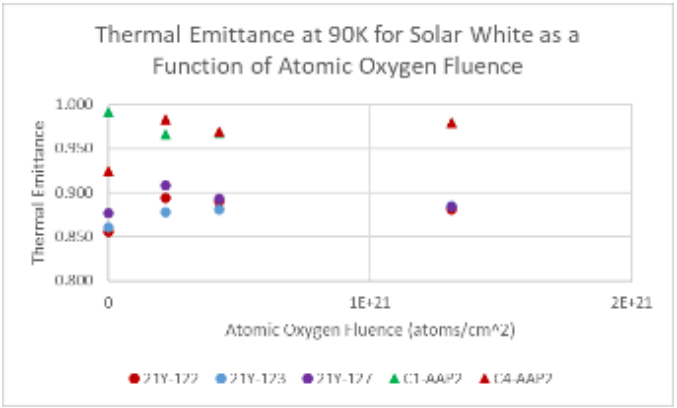

Figure D-18. Thermal emittance at 90K for Solar White tiles and Solar White spray coating on aluminum samples as a function of atomic oxygen fluence.

The emissivity of the Solar White tile samples changed slightly as a result of exposure to atomic oxygen, with a reduced emissivity in two places between 5300 and 10300 nm. The thermal emittance as a function of temperature for the tile samples had the greatest change in emittance with atomic oxygen exposure for temperatures below 150K. At 90K, the thermal emittance increases then levels off as a function of atomic oxygen exposure fluence. The overall increase in thermal emittance after the third atomic oxygen exposure increment for the Solar White tile samples was less than approximately 3% as shown in Table D-2. The Solar White spray coating on aluminum samples also experienced an emissivity change with a reduced emissivity in two places between 2500 and 10300. The thermal emittance as a function of temperature for temperatures above 150K decreased with atomic oxygen exposure but the change below 150K was more random. At 90K the thermal emittance for C1AAP2 decreased roughly 2.5% then slightly increased as a function of atomic oxygen fluence for an overall decrease in thermal emittance of roughly 1% after the third exposure increment. The thermal emittance for C4AAP2 increased 6.27% initially followed by a decrease and small increases in thermal emittance as a function of atomic oxygen fluence for an overall net gain in emittance of roughly 5.8%. The change in thermal emittance for all of the Solar White samples was very low in comparison to the change in solar absorptance.

Table D-2. Thermal emittance at 90K as a function of atomic oxygen fluence for Solar White tile and spray coating on aluminum samples.

Sample	Initial Thermal Emittance at 90K	Thermal Emittance at 90K after Atomic Oxygen Fluence of 2.17e20 atoms/cm^2	Change in Thermal Emittance at 90K	Percent Change
21Y-122	0.855	0.894	0.039	4.56
21Y-123	0.861	0.878	0.017	1.97
21Y-127	0.877	0.908	0.031	3.53
C1AAP2	0.991	0.966	-0.025	-2.52
C4AAP2	0.925	0.983	0.058	6.27
Sample	Thermal Emittance at 90K after Atomic Oxygen Fluence of 2.17e20 atoms/cm^2	Thermal Emittance at 90K after Atomic Oxygen Fluence of 4.24e20 atoms/cm^2	Change in Thermal Emittance at 90K	Percent Change
21Y-122	0.894	0.890	-0.004	-0.45
21Y-123	0.878	0.881	0.003	0.34
21Y-127	0.908	0.893	-0.015	-1.65
C1AAP2	0.966	0.968	0.002	0.21
C4AAP2	0.983	0.969	-0.014	-1.42
Sample	Thermal Emittance at 90K after Atomic Oxygen Fluence of 4.24e20 atoms/cm^2	Thermal Emittance at 90K after Atomic Oxygen Fluence of 1.31e21 atoms/cm^2	Change in Thermal Emittance at 90K	Percent Change
21Y-122	0.890	0.881	-0.009	-1.01
21Y-123	0.881	0.885	0.004	0.45
21Y-127	0.893	0.884	-0.009	-1.01
C1AAP2	0.968	0.980	0.012	1.24
C4AAP2	0.969	0.979	0.010	1.03
Sample	Initial Thermal Emittance at 90K	Thermal Emittance at 90K Atomic Oxygen Fluence of 1.31e21 atoms/cm^2	Change in Thermal Emittance at 90K	Percent Change
21Y-122	0.855	0.881	0.026	3.04
21Y-123	0.861	0.885	0.024	2.79
21Y-127	0.877	0.884	0.007	0.80
C1AAP2	0.991	0.980	-0.011	-1.11
C4AAP2	0.925	0.979	0.054	5.84

Conclusions

All of the Solar White samples exhibited a change in AM0 solar absorptance as a function of exposure to atomic oxygen. The greatest change occurred early on in the exposure then leveled off. The net change for the AM0 solar absorptance of the tile samples was slightly less than for the spray coating on aluminum samples although the initial values for the tile samples (0.012-0.018) were lower than those of the spray coated samples (~0.08). This difference drove the % change to be 160-275% for the tile samples and 51-54% for the spray coated samples. The thermal emittance percentage change at 90K was much lower but followed a similar trend in that the thermal emittance mostly increased with atomic oxygen fluence with the greatest change early on in the exposure then leveling off. The change was more random in nature but stayed overall less than about 6%. The ability to reject heat for a space thermal system is usually determined by looking at the ratio of AM0 solar absorptance to thermal emittance at the temperature of interest. It is desired to keep the ratio as low as possible. For the Solar White tile samples, the solar absorptance to thermal emittance ratio for 90K was about 0.017 initially and increased to 0.051 after an atomic oxygen effective fluence of 1.31e21 atoms/cm^2, while the ratio for the Solar White spray coating on aluminum samples changed from approximately 0.084 to 0.128 for the same exposure. This indicates that although both the solar absorptance and thermal emittance increased with atomic oxygen exposure, the change in solar absorptance was dominant causing an increase in the solar absorptance to thermal emittance ratio.

References

1) Banks, B.A.; Rutledge, S.K.; de Groh, K. K.; Stidham, C.R.; Gebauer, L.; LaMoreaux, C.M.; *Atomic Oxygen Durability Evaluation of Protected Polymers Using Thermal Energy Plasma Systems,* International Conference on Plasma Synthesis and Processing of Materials, Denver, CO, February 21-25, 1993.
2) Standard Practices For Ground Laboratory Atomic Oxygen Interaction Evaluation Of Materials For Space Applications, ASTM E-2089-15(2020).
3) Siegal, R. and Howell, J.R.; Thermal Radiation Heat Transfer, Second Edition, Mc Graw Hill, 1981.
4) 2000 ASTM Standard Extraterrestrial Spectrum Reference E-490-00, http://rredc.nrel.gov/solar/spectra/AM0.

APPENDIX E: ULTRAVIOLET RADIATION EXPOSURE OF SOLAR WHITE COUPONS

Sharon Miller
NASA Glenn Research Center, Cleveland OH

Emily Naim
HX5 at NASA Glenn Research Center, Cleveland OH

Introduction

This report summarizes the results of testing completed under the STMD GCD Cryogenic Fluid Transfer project to measure the effect of ultraviolet radiation on the solar absorptance and thermal emittance of tiles composed of Solar White and Solar White sprayed onto aluminum substrates. The ultraviolet radiation dose levels were provided by the project to represent levels that the Solar White thermal control surface may be exposed to on a cryogenic refueling platform. There is concern that exposure to ultraviolet radiation may affect the ability of the thermal control surface to absorb and reject heat thereby reducing the effectiveness of the thermal control surface. The Solar White coupons were exposed to three dose levels of ultraviolet radiation and the solar absorptance and thermal emittance were measured on each coupon as received and after each exposure increment.

Test Description

Ultraviolet (UV) radiation exposure testing was conducted in the UV Belljar. The vacuum belljar which is shown in Figure E-1 was evacuated using a CTI Cryogenics cryopump after achieving a rough vacuum using an Agilent dry scroll pump. Vacuum in the chamber during testing was approximately 2.6e-6 Torr. UV radiation was provided by a deuterium lamp (Hammamatsu L7293) to cover the vacuum UV (VUV) (115-200 nm) and a Mercury-Xenon arc lamp (Newport 66142) to cover the near UV (NUV) (200-400 nm). An aluminum sample mounting plate shown in Figure E-1 was machined to fit the 2.54 cm diameter Solar White coupons that were provided. The holder was machined to various depths to accommodate the difference in thickness between the sample coupons that were Solar White tiles and those that were Solar White spray coated onto aluminum substrates so that the surfaces were all level with the top of the sample plate. The holder was fabricated so that there was a 60-degree angle between the arrival of the VUV lamp radiation and normal to the sample holder surface. The NUV lamp radiation arrived at a 30- degree angle with respect to surface normal. The holder was mounted to a motor driven movable plate that positioned the sample holder so that it was in the center of the arrival from both the VUV and NUV lamps. The sample holder and drive motor were housed inside a water-cooled copper box to reduce overheating. The intensity of the VUV arrival was measured in vacuum at the midplane of the sample holder using a cesium iodide (CsI) detector. The detector was mounted at the midplane of a second water cooled chamber inside the belljar, and the lamp was moved from the feedthrough for the sample chamber to the feedthrough for the detector chamber at the beginning and end of each test increment to determine the average intensity during that exposure increment. The NUV intensity was measured by mounting a BlackRay detector on the sample holder and measuring the NUV intensity through the chamber window while in air at the start and end of testing. The sun intensity of the VUV lamp was calculated by dividing the measured lamp intensity by the integrated ASTM E-4901 sun intensity in W/cm2 from 115-200 nm. Likewise, the sun intensity of the NUV lamp was calculated by dividing the measured lamp intensity by the integrated ASTM

E-4901 sun intensity in W/cm2 from 200-400 nm. Sun intensity during testing ranged from 0.75 to 1.27 suns for VUV and 1.75 to 2.04 suns for NUV. The average sun intensity for each exposure increment was multiplied by the time duration of the increment to achieve the equivalent sun hours (ESH) for that exposure increment.

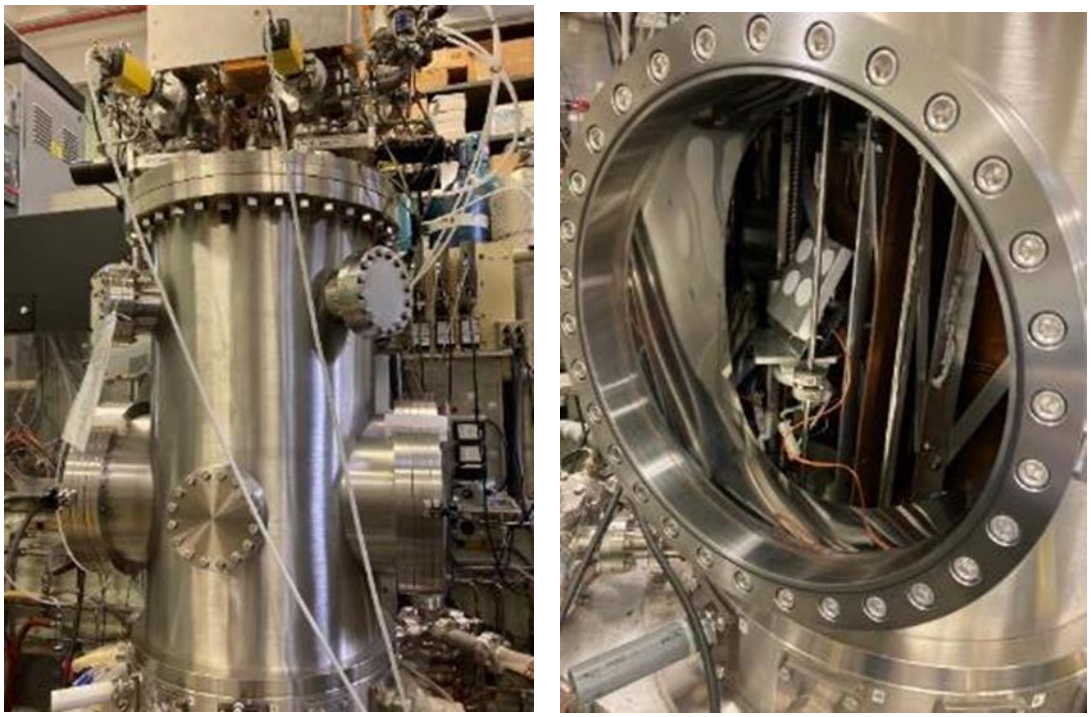

Figure E-1. Vacuum UV bell jar with Solar White samples mounted inside.

Before and after each UV exposure increment, the reflectance of the surface in the ultraviolet-visible-near infra-red was measured as a function of wavelength from 250 to 2500 nm using a Cary 5000 spectrophotometer with a DRA-2500 integrating sphere. This was used to calculate the absorptivity (absorptivity =1-reflectivity). The reflectance in the IR wavelength ranges as a function of wavelength was measured in the same manner using a Nicolet FTIR with Pike integrating sphere attachment. This was used to calculate the emissivity (emissivity=1-IR reflectivity). The total thermal emittance was calculated by integrating the emissivity as a function of wavelength with respect to the black body curve at each temperature of interest[2], and the solar absorptance was calculated by integrating the solar absorptivity with respect to the Air Mass Zero (AM0) solar spectrum[3].

Results and Discussion

Solar White tile samples: 21Y-130, 21Y-131, and Solar White spray coating on aluminum samples: C3AAP2, and wired sample #2 were exposed to three increments of UV exposure up to a total exposure of approximately 844 ESH NUV and 458 ESH VUV total. Figure E-2 contains a photo of the Solar White samples in the holder after UV exposure. After exposure, the initially bright white samples were visibly discolored. Solar White tile sample 21Y-131 was not able to be measured or tested further after the second exposure increment because it slipped from the holder on the UV-VIS-NIR integrating sphere while being measured and broke into multiple small segments.

The reflectance as a function of wavelength data showed that the Solar White was becoming significantly less reflecting in the blue to green portion of the spectrum with exposure, which confirmed the visual observation that the samples had discolored to a light tan color. Figures E-3 through E-5 contain the reflectivity as a function of VUV and NUV exposure of the Solar White samples. After the final UV exposure, the samples were left sitting in their containers exposed to room air for 118 hrs. in order to investigate whether the Solar White is forming color centers that bleach out when exposed to air. The solar absorptivity and emissivity were then measured again to look for evidence of recovery of the spectra due to air bleaching. As can be seen from the spectra, the time in air did not result in any significant recovery of the absorptivity or reflectivity.

Figure E-2. Solar White coupons in sample holder after UV exposure to approximately 844 ESH NUV and 458 ESH VUV. Tile sample 21Y-131 was not present in the holder at the end of the test as it slipped out of the holder during UV-VIS-NIR measurement after the second increment and broke.

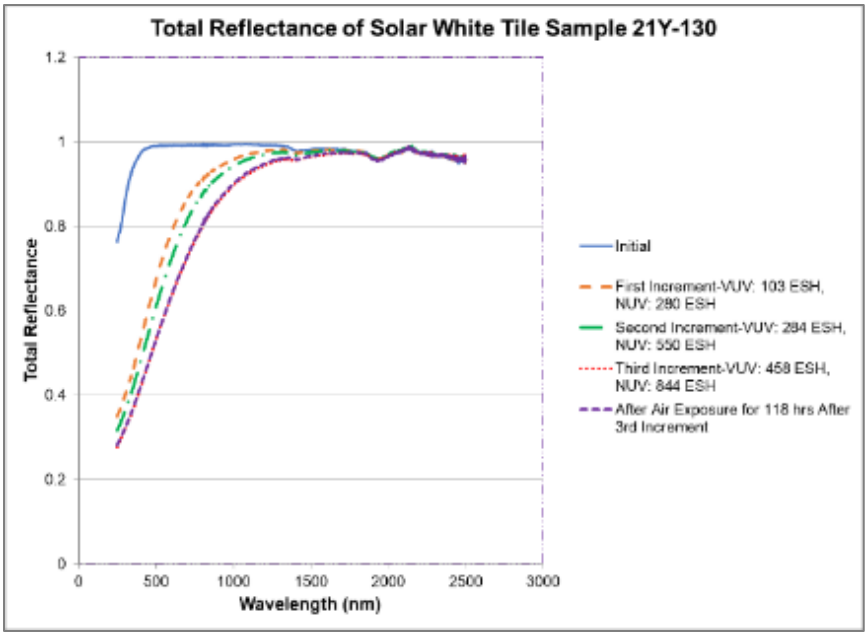

Figure E-3. Reflectivity of Solar White thermal control tile 21Y-130 with UV exposure

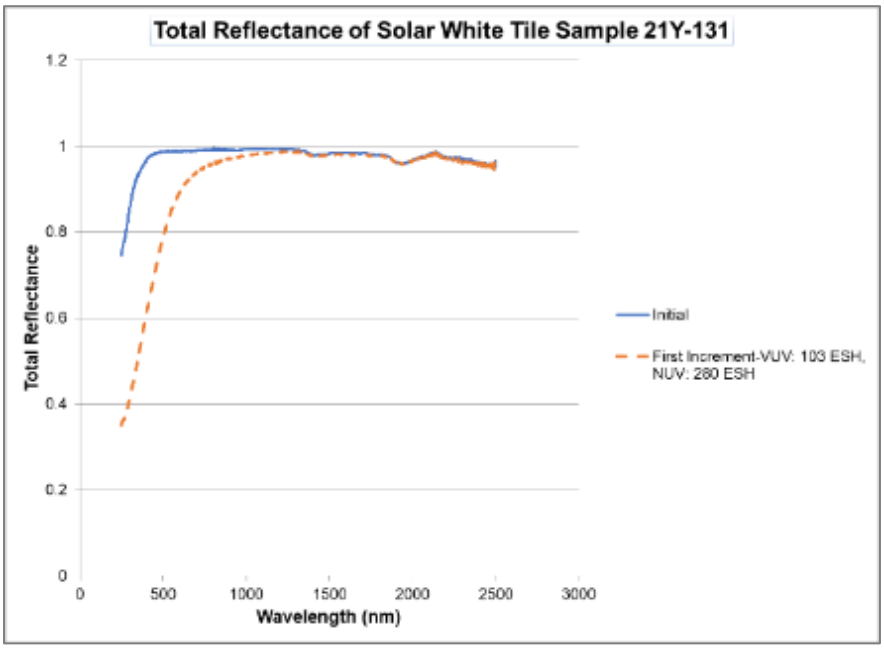

Figure E-4. Reflectivity of Solar White thermal control tile 21Y-131 with UV exposure.

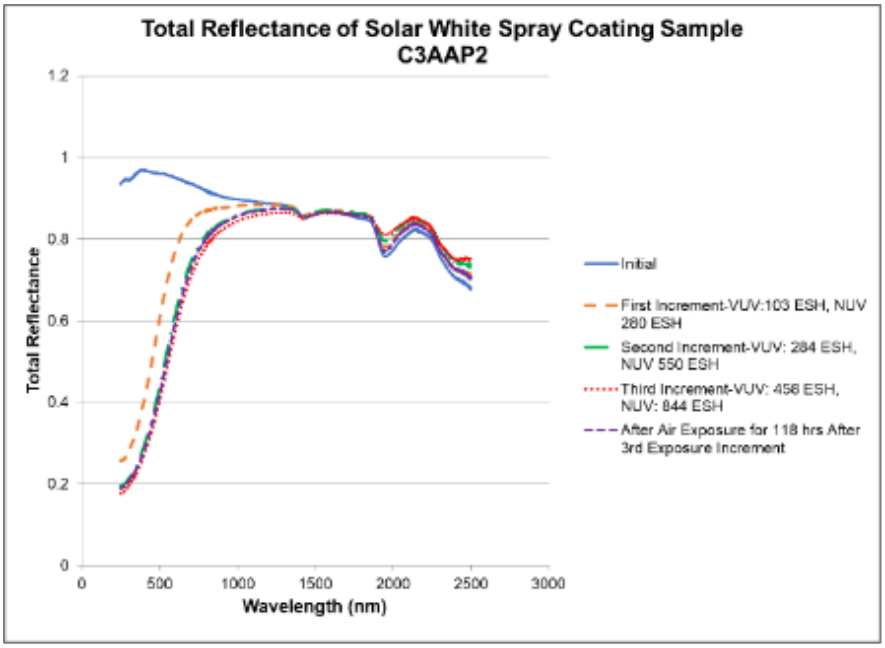

Figure E-5. Reflectivity of Solar White thermal control spray coating C3AAP2 on aluminum with UV exposure.

For both the Solar White tiles and Solar White spray coating on aluminum samples, the greatest change occurred early in the exposure with less noticeable changes after the first exposure increment. Table E-1 contains the air mass zero (AM0) solar absorptance values as a function of UV exposure for each of the Solar White samples. The greatest percentage change in AM0 solar absorptance with UV exposure overall, occurred for the Solar White tile sample. Overall, the tile samples exhibited an approximately 1550% increase in AM0 solar absorptance while the spray coating on aluminum sample increased approximately 361%. The tile samples however still had an AM0 solar absorptance lower than the spray coating on aluminum sample.

Table E-1. Air Mass Zero (AM0) Solar Absorptance as a Function of UV Exposure for Solar White Tile and Solar White Spray Coating on Aluminum Samples.

Sample	Initial Solar Absorptance	Solar Absorptance after 103 ESH VUV and 280 ESH NUV	Change in Solar Absorptance	Percent Change
21Y-130	1.72E-02	1.89E-01	1.72E-01	996.12
21Y-131	1.93E-02	1.32E-01	1.13E-01	583.40
C3AAP2	7.97E-02	2.63E-01	1.83E-01	229.96

Sample	Solar Absorptance after 103 ESH VUV and 280 ESH NUV	Solar Absorptance after 284 ESH VUV and 550 ESH NUV	Change in Solar Absorptance	Percent Change
21Y-130	1.89E-01	2.26E-01	3.66E-02	19.34
C3AAP2	2.63E-01	3.43E-01	8.00E-02	30.42

Sample	Solar Absorptance after 284 ESH VUV and 550 ESH NUV	Solar Absorptance after 458 ESH VUV and 844 ESH NUV	Change in Solar Absorptance	Percent Change
21Y-130	2.26E-01	2.84E-01	5.89E-02	26.12
C3AAP2	3.43E-01	3.67E-01	2.43E-02	7.08

Sample	Solar Absorptance after 458 ESH VUV and 844 ESH NUV	Solar Absorptance after 118 hrs in Air Following the Last UV Exposure	Change in Solar Absorptance	Percent Change
21Y-130	2.84E-01	2.82E-01	-2.92E-03	1.03
C3AAP2	3.67E-01	3.54E-01	-1.32E-02	3.60

Sample	Initial Solar Absorptance	Solar Absorptance after 458 ESH VUV and 844 ESH NUV	Overall Change in Solar Absorptance	Percent Change
21Y-130	1.72E-02	2.84E-01	2.67E-01	1549.79
C3AAP2	7.97E-02	3.67E-01	2.88E-01	360.77

Figure E-6 contains a graph of the AM0 solar absorptance of the Solar White samples as a function of NUV ESH. As can be seen from the graph, the AM0 solar absorptance for both the tile and spray coating on aluminum samples increased and started to level off as a function of fluence at about the same rate. As can be seen from the open symbols on the graph, the 118-hour air exposure did not cause any significant bleaching of the samples after the end of the third UV exposure increment in terms of AM0 solar absorptance. The most recovery was in the near IR portion of the spectrum.

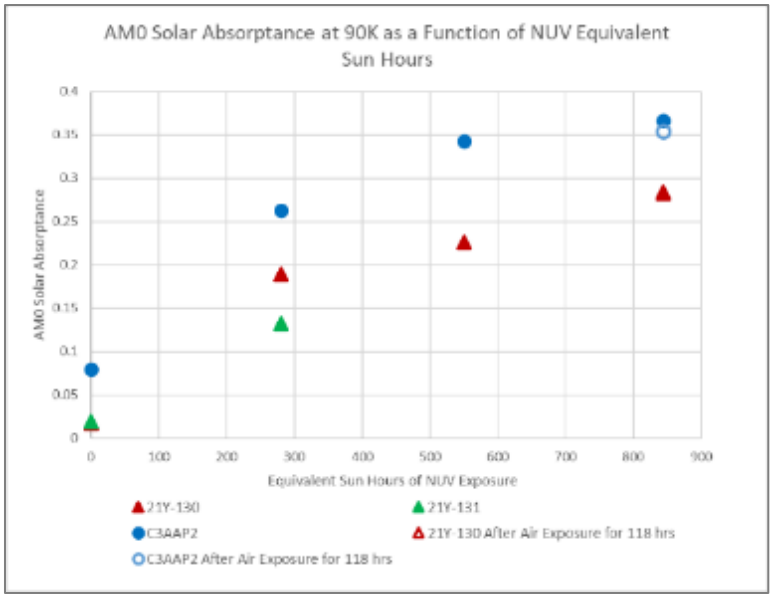

Figure E-6. AM0 Solar Absorptance of Solar White tile and Solar White spray coating on aluminum samples as a function of UV exposure.

Figures E-7 through E-12 contain graphs of emissivity and total thermal emittance vs temperature for each of the Solar White samples with UV exposure. Figure E-13 contains a graph of the emittance at 90K as a function of UV exposure.

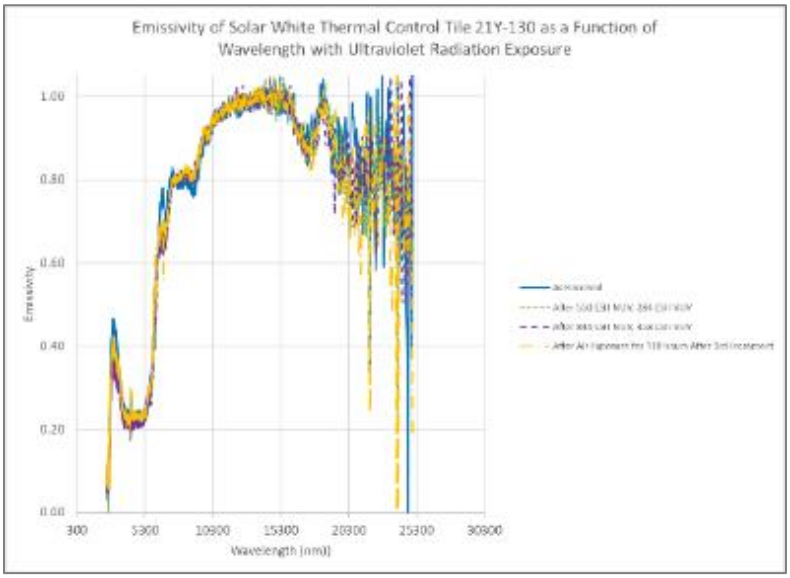

Figure E-7. Emissivity of Solar White tile sample 21Y-130 as a function of UV exposure.

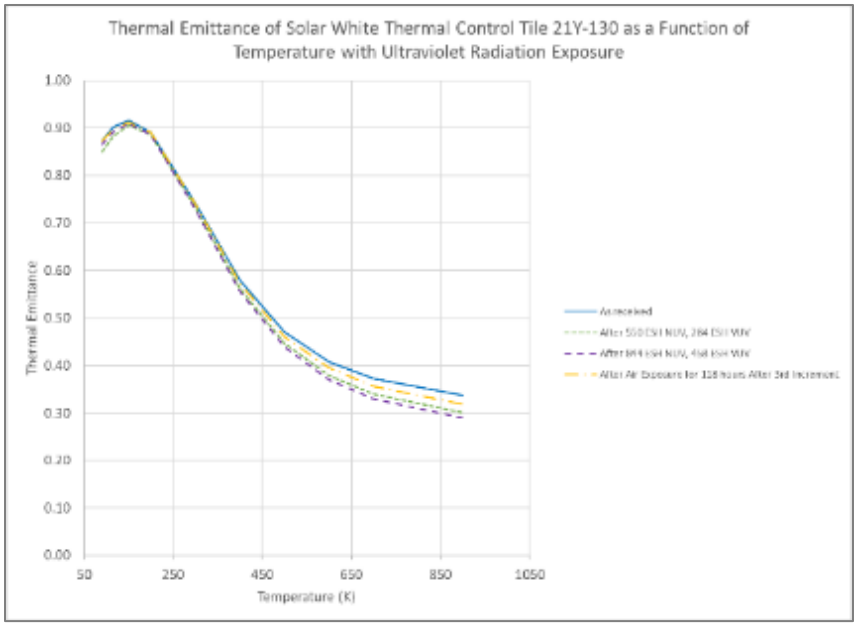

Figure E-8. Thermal emittance as a function of temperature and UV exposure for Solar White tile sample 21Y-130.

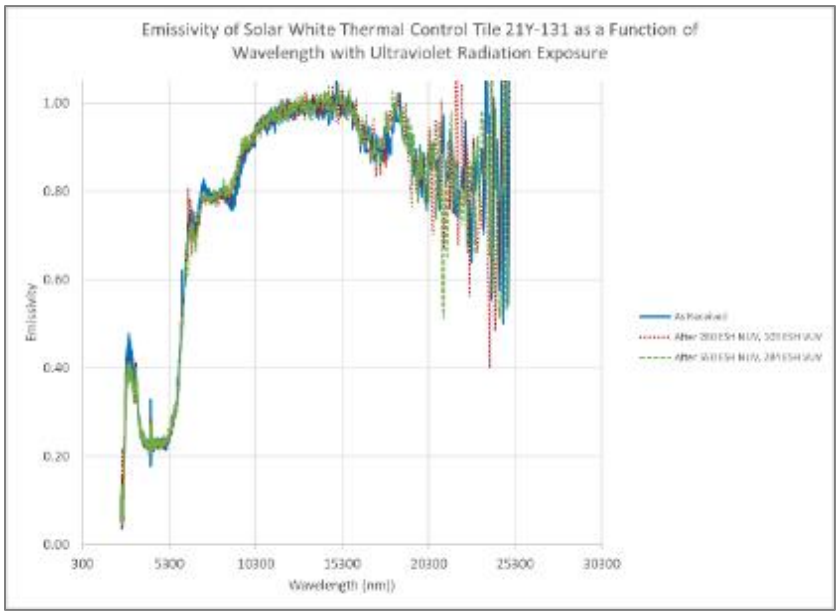

Figure E-9. Emissivity of Solar White tile sample 21Y-131 as a function of UV exposure.

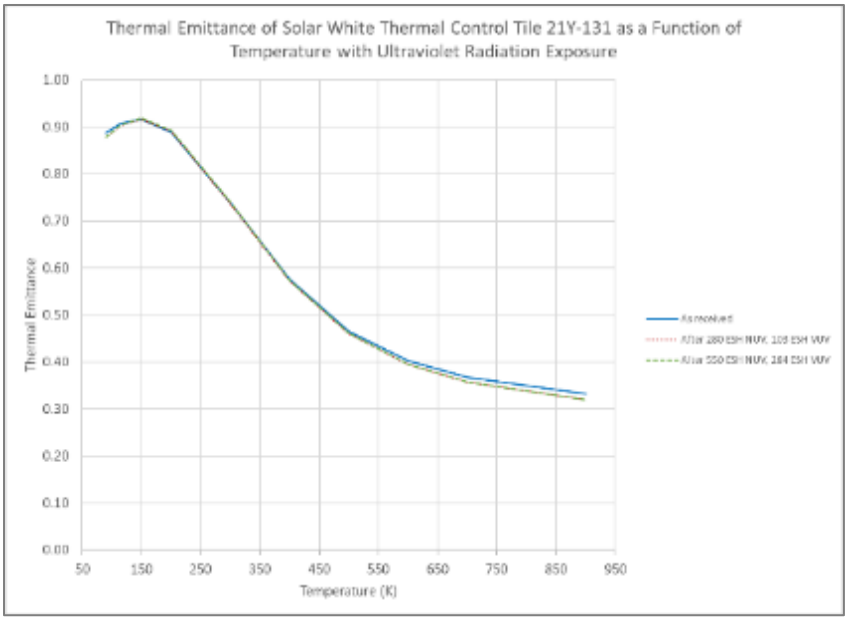

Figure E-10. Thermal emittance as a function of temperature and UV exposure for Solar White tile sample 21Y-131.

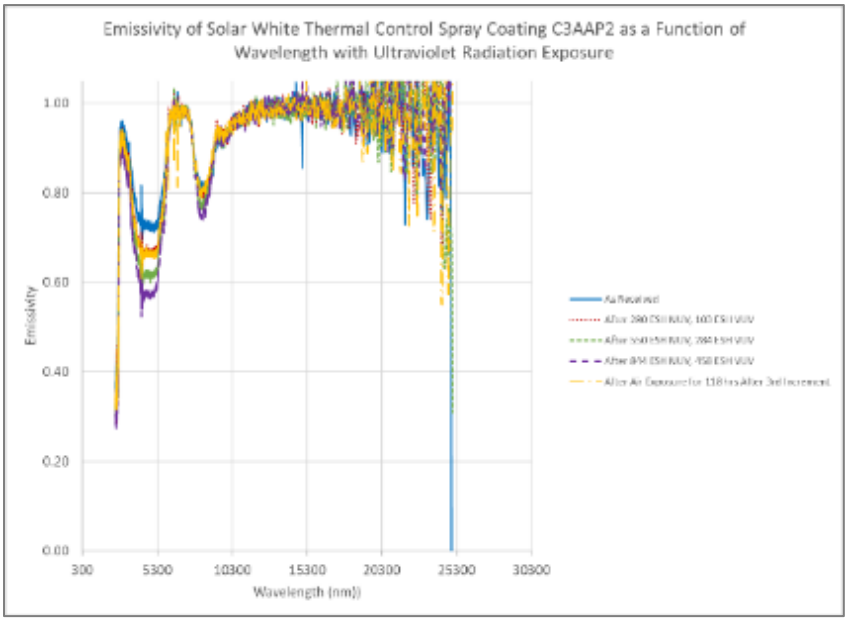

Figure E-11. Emissivity as a function of UV exposure for Solar White spray coating on aluminum sample C3AAP2.

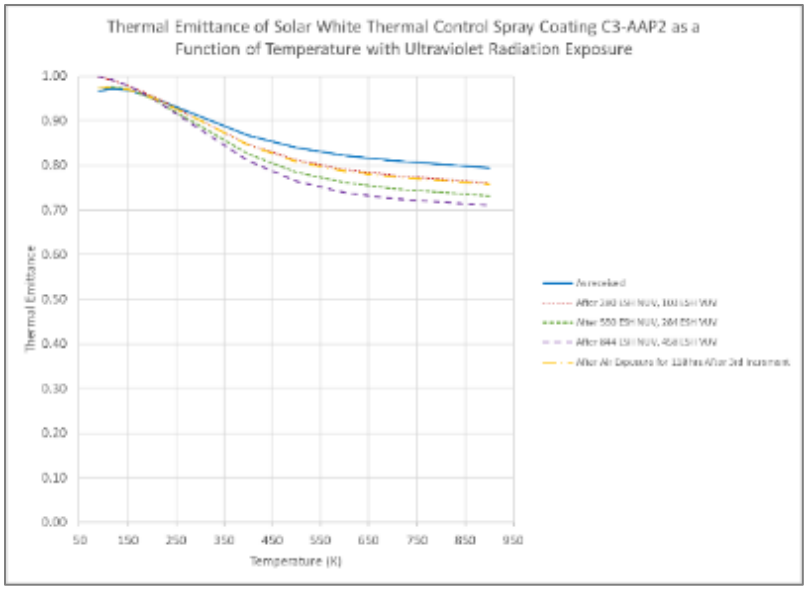

Figure E-12. Thermal emittance as a function of temperature and UV exposure for Solar White spray coating on aluminum sample C3AAP2.

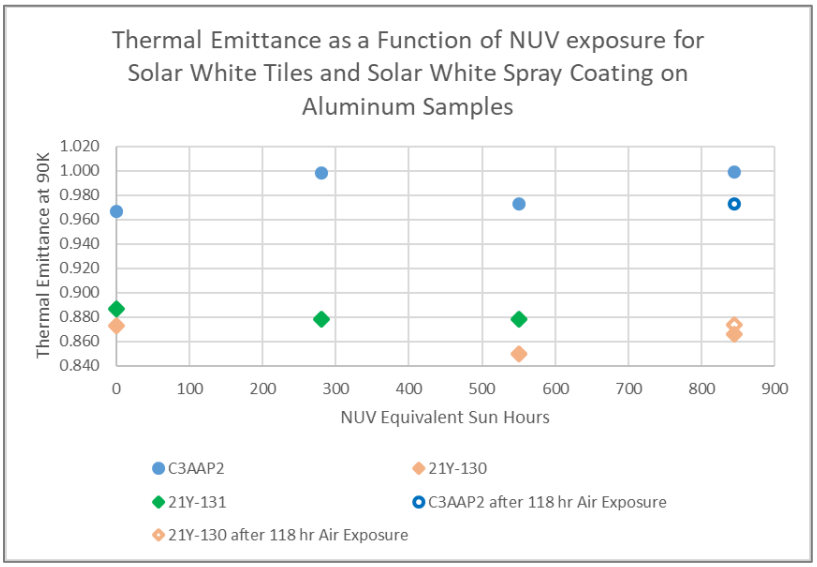

Figure E-13. Thermal emittance at 90K for Solar White tiles and Solar White spray coating on aluminum samples as a function of UV exposure.

Table E-2. Thermal Emittance at 90K as a Function of UV Exposure for Solar White Tile and Solar White Spray Coating on Aluminum Samples.

Sample	Initial Thermal Emittance at 90K	Thermal Emittance at 90K after UV Exposure to 103 ESH VUV and 280 ESH NUV	Change in Thermal Emittance at 90K	Percent Change
21Y-130	0.873			
21Y-131	0.887	0.878	-0.009	-1.01
C3AAP2	0.967	0.998	0.031	3.21
Sample	Thermal Emittance at 90K after UV Exposure to 103 ESH VUV and 280 ESH NUV	Thermal Emittance at 90K after UV Exposure to 284 ESH VUV and 550 ESH NUV	Change in Thermal Emittance at 90K	Percent Change
21Y-130		0.850		
21Y-131	0.878			
C3AAP2	0.998	0.973	-0.025	-2.51
Sample	Thermal Emittance at 90K after UV Exposure to 284 ESH VUV and 550 ESH NUV	Thermal Emittance at 90K after UV Exposure to 458 ESH VUV and 844 ESH NUV	Change in Thermal Emittance at 90K	Percent Change
21Y-130	0.850	0.866	0.016	1.88
21Y-131				
C3AAP2	0.973	0.999	0.026	2.67
Sample	Thermal Emittance at 90K after UV Exposure to 458 ESH VUV and 844 ESH NUV	Thermal Emittance at 90K after 118 hr exposure in air following the last UV exposure	Change in Thermal Emittance at 90K	Percent Change
21Y-130	0.866	0.874	0.008	0.92
21Y-131				
C3AAP2	0.999	0.973	-0.026	-2.60
Sample	Initial Thermal Emittance at 90K	Thermal Emittance at 90K after UV Exposure to 458 ESH VUV and 844 ESH NUV	Change in Thermal Emittance at 90K	Percent Change
21Y-130	0.873	0.866	-0.007	-0.80
21Y-131	0.887			
C3AAP2	0.967	0.999	0.032	3.31

The emissivity of the Solar White tile samples changed slightly as a result of exposure to UV radiation, with a reduced emissivity in several places between 2500 and 10300 nm. The thermal emittance as a function of temperature for the tile samples had the greatest change in emittance with UV exposure for temperatures above approximately 400K. At 90K, the thermal emittance appeared to be mostly level with a slight fluctuation as a function of UV exposure. Overall, the change in thermal emittance at 90K after the third UV exposure increment for the Solar White tile samples was less than 1% as shown in Table E-2. The Solar White spray coating on aluminum samples also experienced an emissivity change with a reduced emissivity in two places between 2500 and 10300. The thermal emittance as a function of temperature for temperatures above 200 K decreased with UV exposure but the change below 150 K was somewhat random. At 90 K the thermal emittance for C1AAP2 fluctuated with UV exposure by about +/- 3%. The change in thermal emittance at 90K for all of the Solar White samples was very low in comparison to the change in solar absorptance. The change at higher temperatures was more significant.

Conclusions

All of the Solar White samples exhibited a change in AM0 solar absorptance as a function of UV exposure. The greatest change occurred early on in the exposure then leveled off. The net change for the AM0 solar absorptance of the tile samples was slightly less than for the spray coating on aluminum samples although the initial values for the tile samples (0.017-0.019) were lower than those of the spray coated sample (~0.08). This difference drove the % change to be 1550% for the tile sample and approximately 361% for the spray coated samples. The thermal emittance percentage change at 90K was much lower and more random in nature but stayed overall less than about 3.5%. The ability to reject heat for a space thermal system is usually determined by looking at the ratio of AM0 solar absorptance to thermal emittance at the temperature of interest. It is desired to keep the ratio as low as possible. For the Solar White tile samples, the solar absorptance to thermal emittance ratio for 90K was about 0.02 initially and increased to 0.33 after UV exposure to 458 ESH VUV and 844 ESH NUV, while the ratio for the Solar White spray coating on aluminum samples changed from approximately 0.08 to 0.37 for the same exposure. This is a significant change for a thermal control system.

References

1) Standard Solar Constant and Zero Air Mass Solar Spectral Irradiance Tables, ASTM E-490-00a (2019).
2) Siegal, R. and Howell, J.R.; Thermal Radiation Heat Transfer, Second Edition, Mc Graw Hill, 1981.
3) 2000 ASTM Standard Extraterrestrial Spectrum Reference E-490-00, http://rredc.nrel.gov/solar/spectra/AM0.

APPENDIX F: ELECTROSTATIC CHARGING AND RESISTIVITY TESTING

Introduction

Solar White tile and spray-on test samples were evaluated in simulated low earth orbit (LEO) and GEO environments, to understand the material's charging characteristics in potential end-use orbital environments.

Test Setup

The Solar White test sample configurations are shown in Figure F-1, two spray-on samples and a tile sample consisting of 4 co-mounted tile samples. The following test sequences were performed:

Table F-1. Test samples and protocols for Solar White tests.

Test ID	*Test Sample*	*Test Protocol*
1	Spray-On Sample 20220418-1	GEO
2a	Spray-On Sample 20220418-2	LEO
2b	Spray-On Sample 20220418-2	GEO
2c	Tile sample	GEO

The spray-on samples were 8" x 6" x ¼" thick aluminum panels with a ~ 6" x 6" area spray painted with the Solar White spray-on coating. The thickness of the spray on coating was 3.9-mil and 4.4-mil (average) for Sample 1 and 2 respectively. All uninsulated portions of the aluminum plates were covered in Kapton tape, to insulate bare metal from arcing. The Solar White tile sample consists of four 1" dia x 3mm thick tiles affixed to a 4" x 2.25" x ¼" thick aluminum plate. The tiles were secured to the aluminum plate using Scotchweld-2216 epoxy. All uninsulated portions of the aluminum plate were covered in Kapton tape.

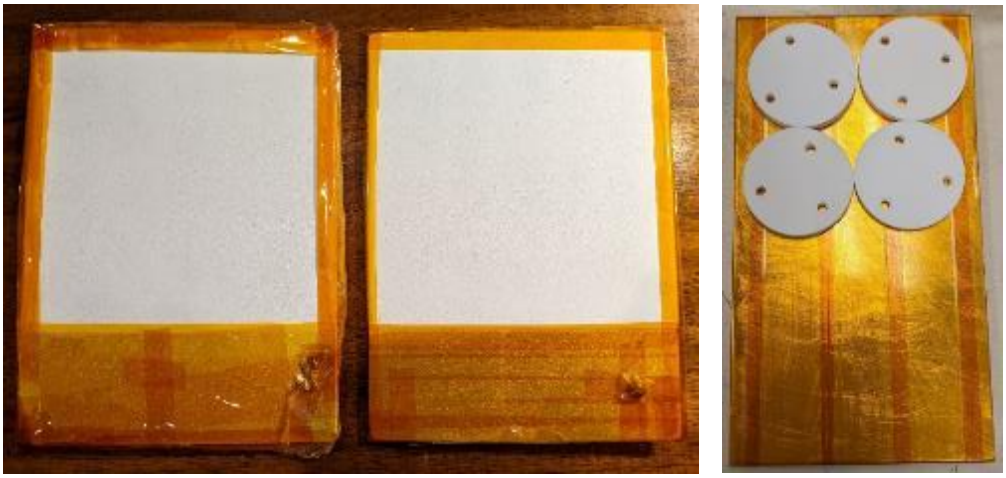

Figure F-1. Solar White test samples: (left) Spray-on samples #1 and #2 and (right) Tile sample.

Tests were performed in a 1.8m diameter by 2m length horizontal vacuum chamber. Testing was performed in two separate test runs. Test 1 included only Spray-On Sample 1 and GEO simulated testing. Test 2 included Spray-on Sample #2 and the Tile Sample.

Samples were mounted in the vertical position at the distance of 120 cm from the electron gun (EG) barrel (Figure F-2). All bare metal surfaces of the coupons were covered with Kapton tape to prevent arcing. The samples were bolted to chamber frames and insulated from the chamber ground. The samples' aluminum plates were connected to a high-voltage feedthrough, which was biased negatively with a power supply through an RC circuit.

Both GEO and LEO environmental testing was performed for Test 2. The difference in the environment was achieved by changing the source of the charging particles: low-temperature Xenon plasma for LEO simulations, and electron beam for GEO simulations.

Figure F-2. Test setup is shown, with all instruments mounted and connected to the recording/measuring equipment.

Test 1

Test 1 consisted of testing Spray-On Sample #1 in a GEO simulated environment using an electron gun as the charging source. The sample was mounted in the chamber in a vertical position at the distance of 120cm from the electron gun barrel (Figure F-2). The electron beam current density was measured and monitored by a Faraday cup biased 50 V using a Keithley 237 source meter. The spray-on material surface potential was measured using a TREK probe (341B with AGILENT voltmeter 34401A), which scanned the painted surface in the horizontal direction-from right to left and back. The parking area for the TREK probe was located on the grounded aluminum plate (shown to the right of the spray-on sample in Figure F-2). The grounded aluminum plate served to adjust "zero" voltage before each individual scan. The sample coupon was biased with a high-voltage power supply through a RC circuit (R=2 MΩ, C=50 nF). All discharge pulse wave forms were recorded with a TEKTRONIX (DPO 7254) oscilloscope (Ch.1-voltage, Ch.2-current). The image of the coupon surface was continuously recorded via video camera and VCR to detect arc

discharges. Vacuum chamber partial pressures were measured and recorded by a residual gas analyzer (RGA) to detect different species in the vacuum chamber and assess the material for decomposition under arcing. Background pressure in the chamber did not exceed 0.2 µTorr during testing.

To evaluate the spray-on material surface charge potential, both inverted and normal gradient testing was performed. In performing an inverted gradient test (dielectric positive with respect to aluminum plate), the sample aluminum plate was biased -5kV. Then, the surface potential of the spray-on coating was measured with the TREK probe before irradiation with electron beam. Next, the coupon was irradiated with electron beam of 5.8 keV energy and 0.6 nA/cm2 current density. Surface potential was measured after about 5 minutes irradiation. Tests were repeated with beam densities of 0.3 and 0.2 nA/cm2. The sample surface was monitored for arcs while discharge pulse wave forms were recorded. To perform normal gradient testing, the sample was biased to -200V and irradiated with beam of 0.5 nA/cm2 current density and 5.6 keV energy. TREK scan was performed immediately after EG was turned OFF. This test was repeated with 8 keV beam energy.

Test 2a

Spray-On Sample 2 and the Tile Sample were both mounted in the vertical plane at the distance of 120 cm from EG barrel. Initially, Sample 2 was tested in simulated LEO plasma environment. Plasma was generated by Kaufman source with a stable flow of Xe. Neutral gas pressure in VF20 was kept steady and equal to 100 µTorr. Filament current and voltage with respect to canister were steady and equal to 4.6 A and 22 V respectively. The stability of plasma parameters was monitored by measuring collection current on one Langmuir probe (LP), and it demonstrated steady state current of 0.16 mA under bias voltage of 20 V (K237). Plasma parameters were determined by sweeping LP (Figure F-3). Floating potential was approximately 1 V and plasma potential was equal to 2 V.

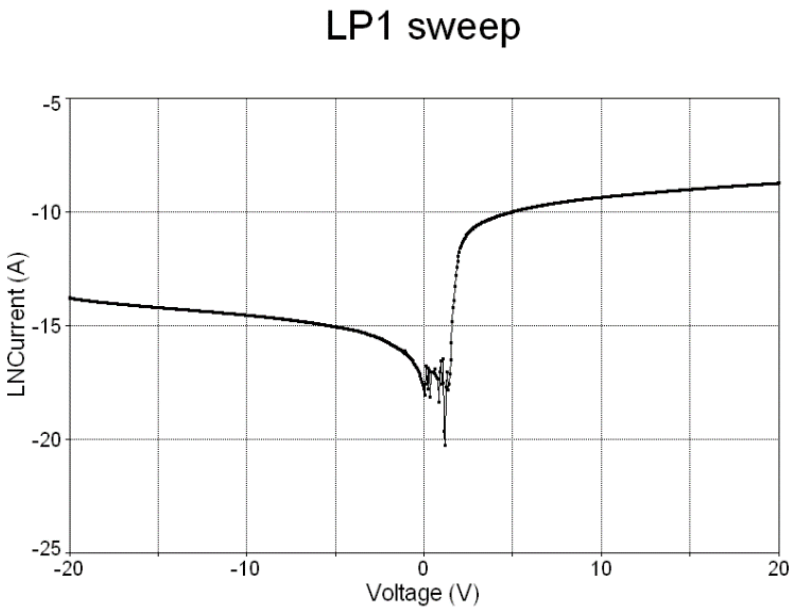

Figure F-3. LP sweep: electron temperature Te=0.25 eV, ne=106 cm^3

To find the paint resistivity of Spray-On Sample 2, the sample was biased straight using the Keithley 237 source meter and voltage was increased stepwise manually to measure current. Each step took about 10 seconds to allow current to get stabilized. The current vs voltage under test is shown in Figure F-4 below.

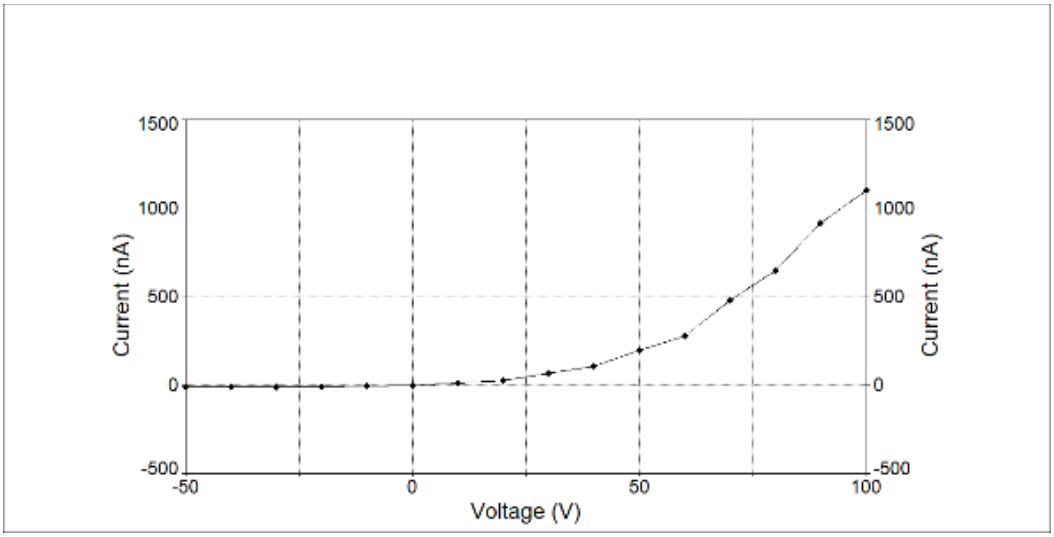

Figure F-4. Current collection vs. bias voltage

The next stage of the test was performed by biasing the sample through RC circuit (R=10 kΩ, C=0.22 µF), and keeping coupon under voltages -200, -250, -300 V for 25 minutes consecutively. These conditions exceed worst case differential charge of LEO conditions.

Test 2b

Testing of Spray-On Sample 2 in GEO simulated environment was conducted with the sample biased -5 kV through RC circuit (R=2.2 MΩ, C=50 nF) and irradiated with electron beam of 5.6 keV energy and 0.5 nA/cm2 current density. The surface of coupon was scanned by TREK probe before irradiation and after 5 minutes of continuous irradiation. Partial pressures of different gases in chamber were monitored during tests in GEO simulated environment

Test 2c

Before testing the Tile Sample, the beam current density distribution was measured by moving the Faraday cup from right to left up to the position of coupon, and back. Beam current density varied from 0.6 nA in the right position to 0.3 nA in the left one. Sample#3 was biased -5 kV through the same RC circuit, irradiated with the beam of 5.6 keV, and kept for 35 minutes under such environment. Due to sample design and the TREK probe's sensitivity to gaps in the measurement surface, charge voltage was not measured for the tile samples. Instead, the tile surface was simply monitored for arcing under GEO conditions. Partial pressures of different gases in chamber were also monitored during testing.

Test Results

Test 1

The inverted gradient testing produced consistent arcing under simulated GEO conditions. The surface potential of Spray-On Sample 1 before electron beam irradiation (Figure F-5) confirmed the -5 kV bias voltage. With the coupon irradiated by the electron beam of 5.8 keV energy and 0.6 nA/cm2 current density, the surface potential of the sample was measured after about 5 minutes irradiation (Figure F-6).

The results show the differential potential reached 5-3.6=1.4 kV. This magnitude was high enough to cause dielectric layer breakdown (Figure F-7) of the Solar White spray-on coating. Examples of discharge pulse wave forms are shown in Figure F-8. Tests were repeated with beam densities of 0.3 and 0.2 nA/cm2, discharges were initiated after 4-5 minutes of irradiation, surface potential profiles and pulse wave forms were similar to ones shown in Figure F-8, but locations of discharges were varied over the painted surface. Results of the normal gradient test are shown below for 5.6 keV (Figure F-9) and 8 keV (Figure F-10) beam energy respectively. These measurements demonstrated high conductivity of white paint: while KAPTON tape charges over 5 kV negative the painted surface potential did not exceed 1 kV. The RGA did not show any signs of paint sputtering/erosion with lower limit of partial pressure of 10-8Torr.

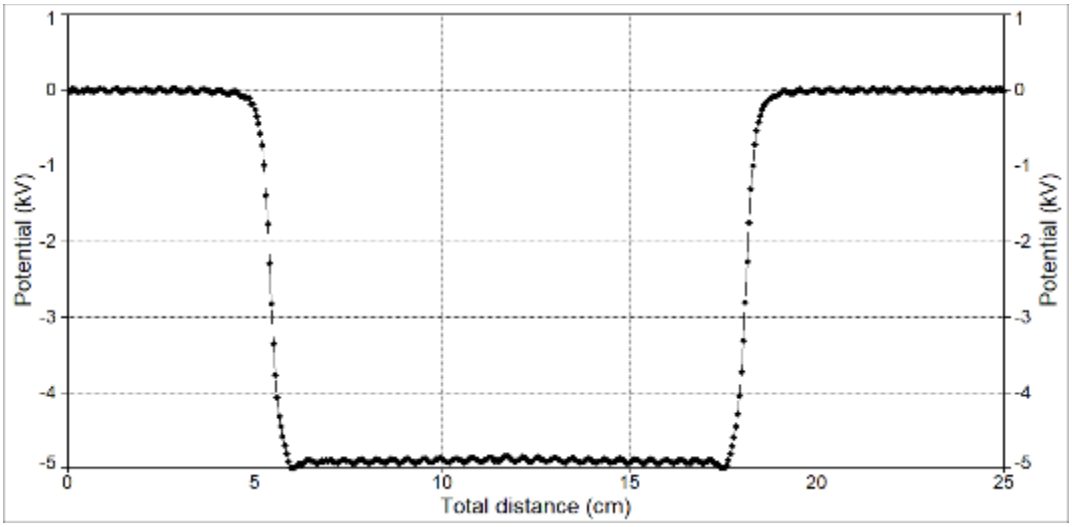

Figure F-5. Surface voltage before electron gun irradiation.

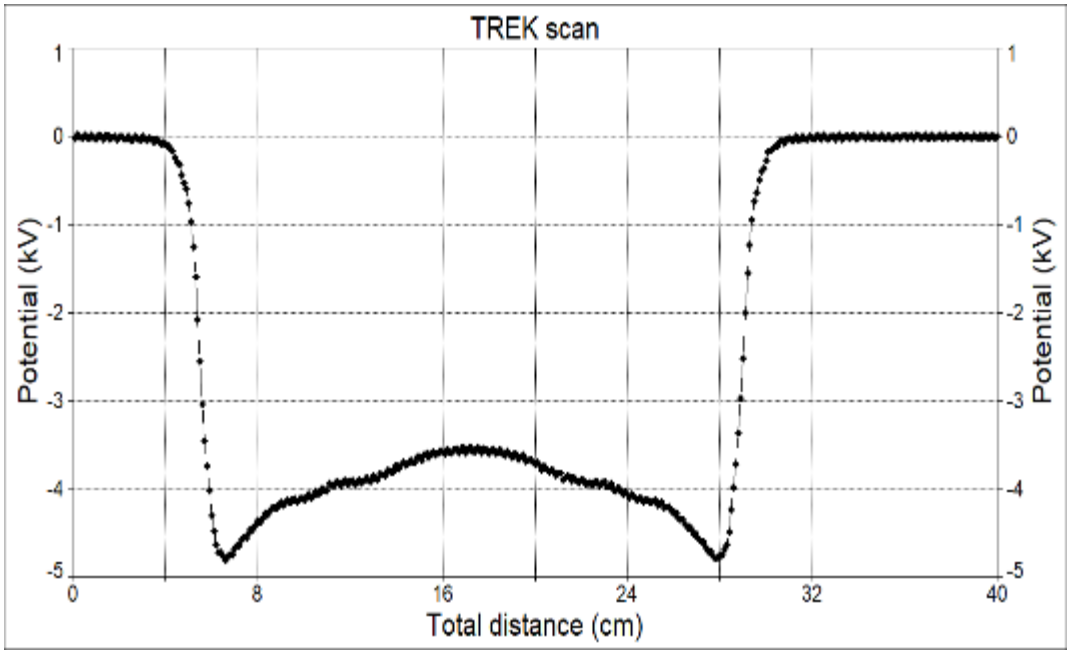

Figure F-6. Surface voltage after irradiation.

Figure F-7. Surface arcing due to dielectric layer breakdown of solar white coating.

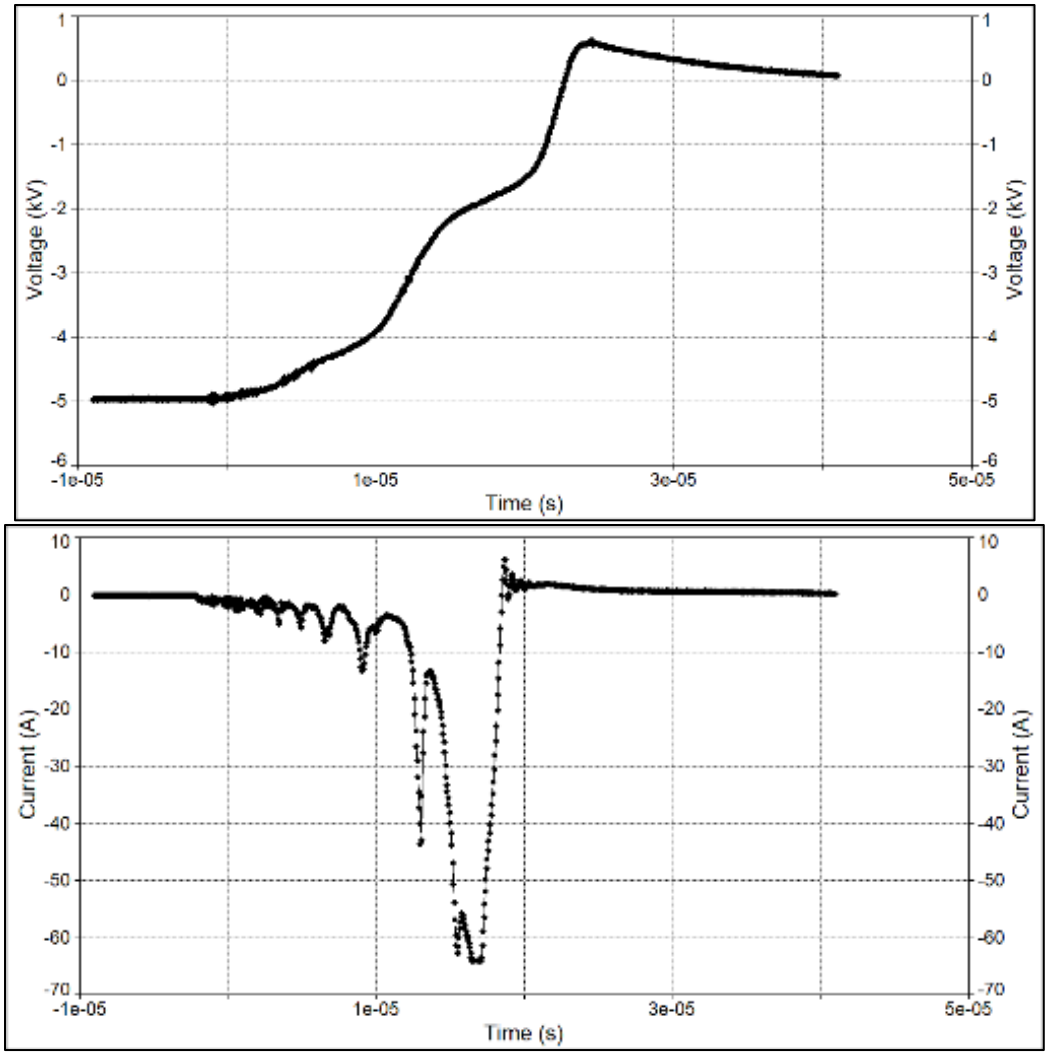

Figure F-8. Examples of discharge pulse wave forms.

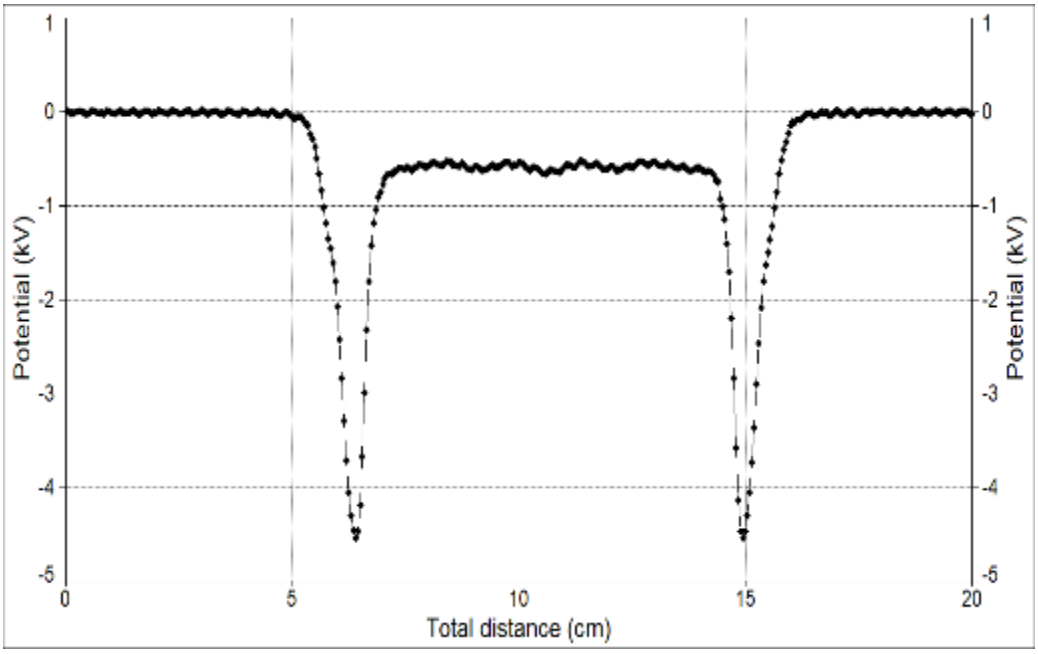

Figure F-9. Surface potential after irradiation with 5.6 keV beam.

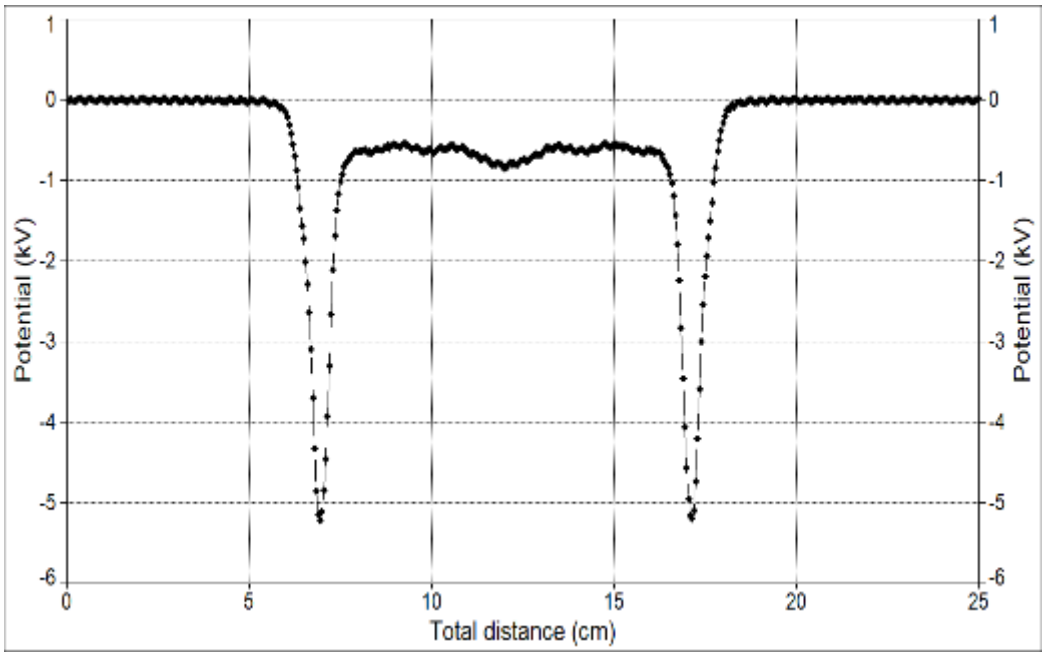

Figure F-10. Surface potential after irradiation with 8 keV beam.

Test 2a

For LEO test simulation (Test 2a), no arcing was initiated throughout the test sweep of voltages and currents, which enveloped worst case LEO conditions. However, it was observed that collected currents had been rising during each step. For example, at -300 V bias, collected current increased from 5.2 µA to 7 µA. It was postulated that the cause was an erosion of the Solar White paint dielectric. To confirm the hypothesis, the sample was re-run at 50 V. The current was

measured to be 1.1 µA vs the original measurement of 200 nA, which was a 5-fold increase in current.

Test 2b

GEO testing for Spray-On Sample 2 (Test 2b) was performed similarly to Test 1. The charge voltage of the spray-on surface was measure before (Figure F-11) and after 5 minutes irradiation with the electron gun (Figure F-12). It is seen that differential voltage reached about 2 kV, and this potential difference was high enough to cause arc/breakdown (Figure F-13).

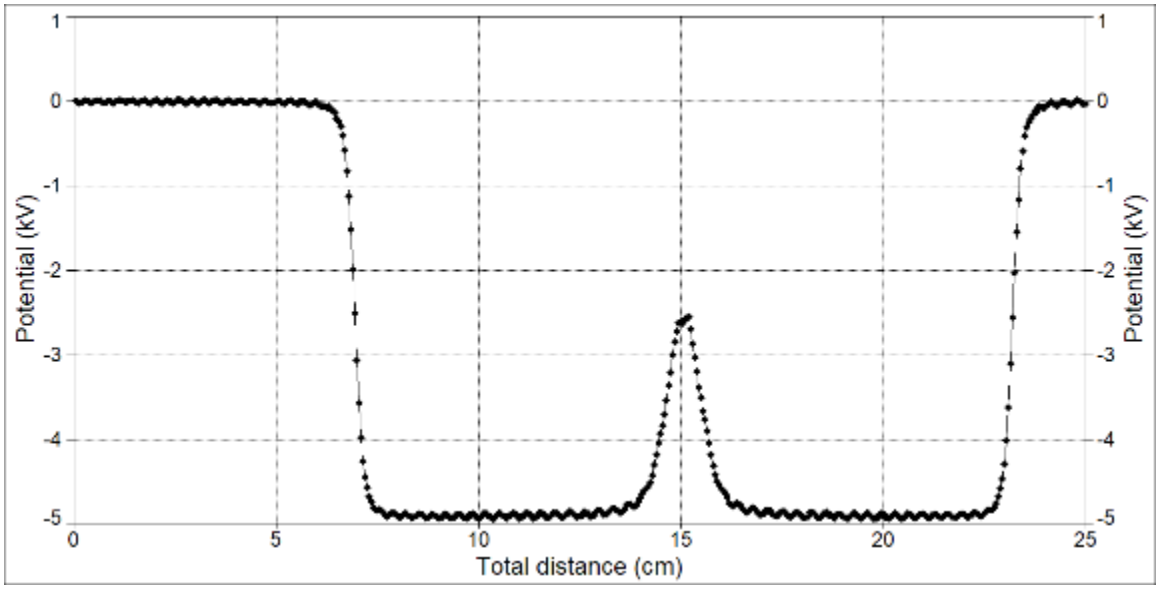

Figure F-11. Spray on sample 2 potential before electron gun irradiation.

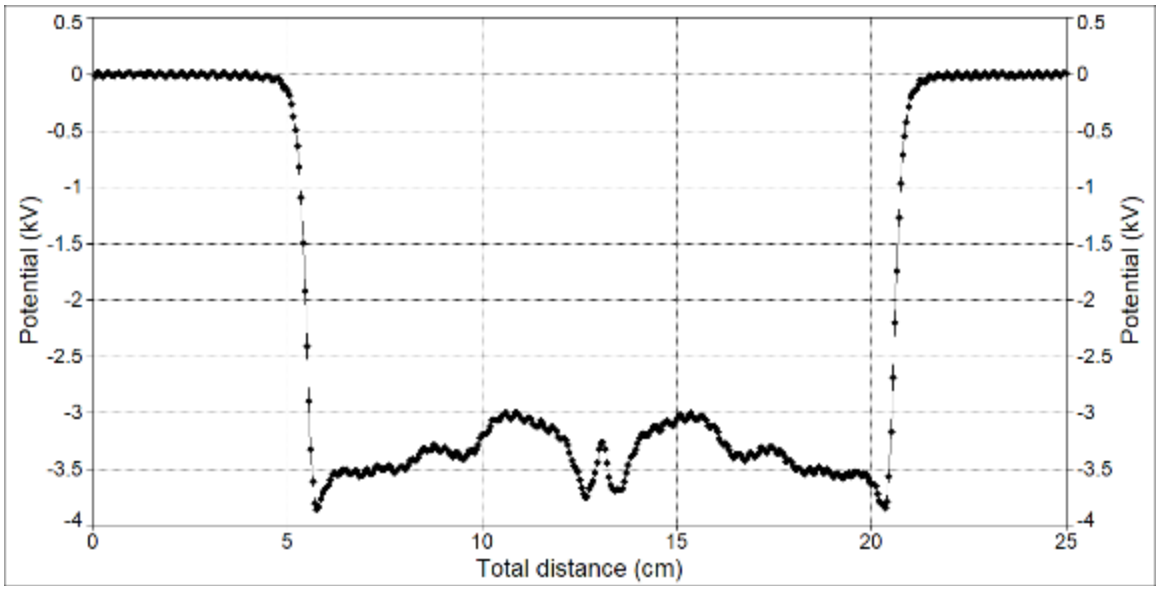

Figure F-12. Spray-on Sample 2 surface potential after 5 minutes of 5.6 keV irradiation.

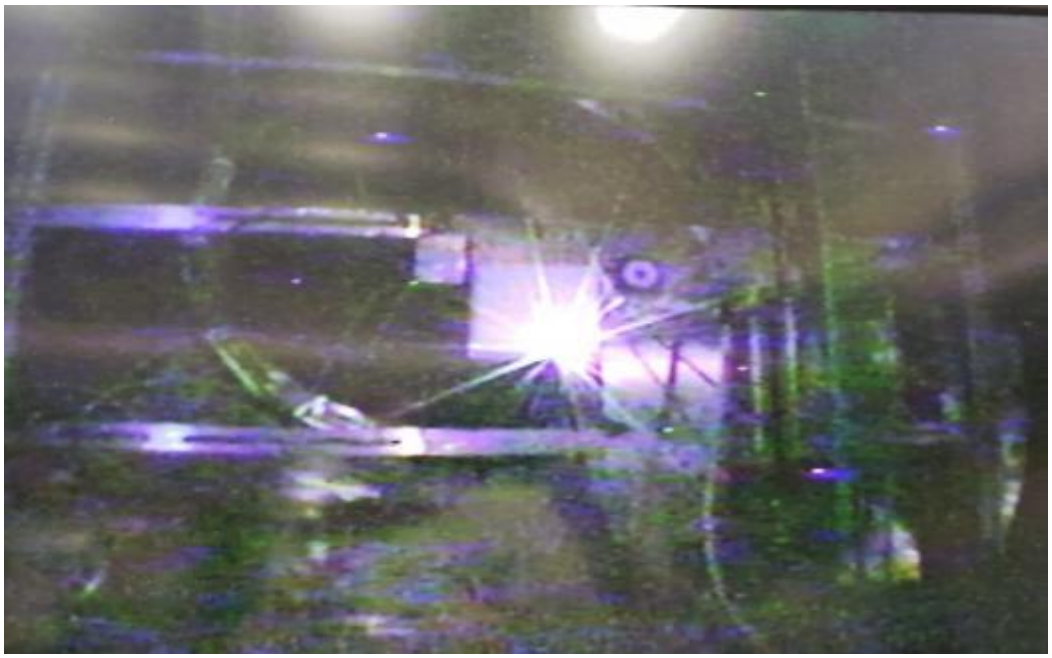

Figure F-13. Arcing due to dielectric breakdown of Spray-on Sample 2.

Test 2c

The Tile Sample was biased -5 kV, irradiated with the beam of 5.6 keV, and kept for 35 minutes under such environment. No arc was observed. Partial pressures of different gases in chamber were monitored during tests in GEO simulated environment. No extra species were observed.

Discussion & Conclusion

This initial work was exploratory in nature. The purpose of this testing was to understand the material's charging characteristics in potential end-use orbital environments, including LEO and GEO. Under LEO conditions, the spray-on sample did not display arcing under the entire test sweep of voltage potentials, indicating the coating has suitably high conductivity for LEO conditions. It should be noted, however, that the LEO test results also indicated that erosion was occurring, which should be investigated in future testing. The simulated GEO environment testing showed that the Solar White spray-on samples were poor performers. In each sample test, the GEO test protocol produced arcing conditions within 5 minutes of charging, under relatively low initial electron gun irradiation levels of 5.8 keV and 0.6 nA/cm^2 current density. This arcing was a result of material dielectric break down. Sample 1 was further evaluated at reduced current densities (0.3 and 0.2 nA/cm2) and still produced similar dielectric breakdown. Note, typical GEO testing starts at a lower current density and works up to 1 nA/cm^2. Conversely, the solar white tile was evaluated for arc and showed no arcing, suggesting material thickness likely plays a factor. Unfortunately, due to tile sample configuration, surface potential of the tile was not evaluated.

Again, this testing was an initial evaluation of the material under LEO and GEO conditions. Potential future work could include evaluating various spray-on thickness or material formulations under GEO conditions, to understand if a threshold or approach exists to prevent dielectric breakdown. Further investigation is also warranted in LEO conditions, where results suggested erosion is occurring. For better evaluation of tile compound, purpose-built samples for EC&R

testing are recommended, which would include larger samples and a sample holder than ensures no gap between the tile and the parking plane of the TREK probe, used to measure surface potential.